Optical and vibrational properties of new ”Nano-Designed” materials produced by pulsed laser deposition

Jeremie Margueritat

To cite this version:

Jeremie Margueritat. Optical and vibrational properties of new ”Nano-Designed” materials produced by pulsed laser deposition. Physics [physics]. Université Paul Sabatier - Toulouse III, 2008. English. NNT : . tel-00288338

HAL Id: tel-00288338
https://theses.hal.science/tel-00288338

Submitted on 16 Jun 2008

Optical and vibrational properties of new *"Nano-Designed"* materials produced by pulsed laser deposition

by Jérémie Margueritat

under the supervision of

Jose Gonzalo de los Reyes & Adnen Mlayah

A Thesis submitted to the

Universidad Autonoma de Madrid & Université Paul Sabatier, Toulouse III

for the obtention of the
Degree of Doctor in Philosophy
speciality :
"Física de Materiales" and "Nanophysique, Nanomesures et Nanocomposants"

before a Jury composed by :

José García Solé (President)
Fco. Javier Solís Céspedes (Referee)
Bruno Palpant (Referee)
Fco. José García Vidal
Adnen Mlayah

LPG
Instituto de Óptica
CSIC

CEMES
Université Paul Sabatier
CNRS

Madrid, April 2008

The physical properties of a metal object change when its charcteristic size is reduced down to few nanometers. This is related to the quantum confinement of electronic states and to the importance of surface excitations in small objects. The combination of these effects with those derived from its inclusion in a host matrix allows the design of new materials with special macroscopic properties. Thus, the control of the size and shape of embedded structures within a few nanometers is one of the most challenging issues faced by nanoscience. In particular, noble metal nanoparticles (NPs) embedded in a dielectric matrix have widely been studied in recent years, since their unique optical properties make them promising materials for optical applications if a good control over the spectral response is achieved. This work focuses on the particular case of thin amorphous Al_2O_3 (a-Al_2O_3) films containing nano-designed Ag nanostructures. The optical properties of Ag nanostructures are characterized by the absorption at the surface plasmon resonance (SPR) wavelength that depends on the nanoparticles morphology. Further tuning of the SPR can be achieved through the synthesis of ordered nanoparticles with complex shapes and controlled morphology. This possibility is particularly challenging, since new optical properties should arise from this "*nano-design*".

Among the possible ways to control the morphology, we have developed a new route to produce thin films containing such shaped nanoparticles, based on the alternate pulsed laser deposition (a-PLD) technique, which allows the deposition of multilayered thin films, offers an excellent control of deposition sequence, and in the case of nanoparticles, allows partial control of the nanoparticles morphology. Using this route we have produced nanostructured thin films containing spherical Ag nanoparticles, nanolentils or nanocolumns, to study the relationship between morphology and optical properties, as well as mixed structures containing alternate layers of Co and Ag nanoparticles to study the plasmon-vibration interaction regime.

The morphology of the nanostructured thin films has been studied using transmission electron microscopy (TEM). The analysis of plan-view and cross section images has shown that we were able to produce spherical Ag nanoparticles with diameters in the range from 2 to 5 nm, nanolentils with an average in-plane diameter of 10 nm and an average height of 6 nm and finally, nanocolumns with average diameters in the range from 2 to 3 nm and a height that as been varied from 6.5 to 65 nm, which corresponds to aspect ratios from 0.6 to 25. Nevertheless, some discontinuities have been observed in the case of nanocolumns, that are most likely related to the production procedure. In the case of samples containing Co and Ag nanoparticles, TEM images show the formation of layers containing spherical Co nanoparticles with an average diameter of 2.7 nm and

Ag nanolentils with an average diameter of 10 nm and an average height of 6 nm. The in-depth sparation between the layers of Co and Ag NPs has been varied from 4 to 8 nm.

The optical properties of these nanostructures have been studied using optical absorption spectra and low frequency Raman spectroscopy. The presence of non-spherical Ag nanoparticles is evidenced in the optical absorption spectrum through the presence of two surface plasmon resonances, the longitudinal and transverse SPR. When the aspect ratio is larger than 1 (nanocolumns) these SPR are located respectively at higher and lower wavelength than that of spherical nanoparticles, while for aspect ratios smaller than 1 (nanolentils) the opposite occurs. Moreover, the well defined longitudinal and transverse SPR modes confirm the self-orientation perpendicular to the substrate surface in the case of the nanocolumns. These results are confirmed by the confined acoustic vibration bands observed in the Raman spectra. In the case of spherical nanoparticles the band observed is due to the degenerated quadrupolar vibration mode ($l = 2$; $m = \pm 0{,}1{,}2$; $n = 0$). When the aspect ratio differs from 1 the five fold of the quadrupolar vibration mode are not longer degenerated and the frequency of the band observed is shifted with respect to the case of spherical nanoparticles. The vibrations modes observed for samples containing nanolentils or nanocolumns have been identified as spheroidal-like modes ($l = 2$; $m = \pm 0{,}1$; $n = 0$) and ($l = 2$; $m = \pm 2$; $n = 0$), respectively.

The final part of the work is devoted to the study of the Raman response of samples containing Co nanoparticles and Ag nanolentils. Raman scattering, of samples containing only Ag nanolentils, excited at a wavelength close to the SPR reveals confined acoustic phonons of the silver nanolentils, while no vibration bands were observed in samples containing only Co nanoparticles. In mixed systems the vibration band corresponding to Ag nanolentils remains constant, while a new band related to acoustic vibrations of Co nanoparticles appears when the distance between Co nanoparticles and Ag nanolentils layers decreases below a certain threshold. The analysis of the Raman scattering suggests the existence of coupling between Co and Ag nanoparticles for separations shorter than 6 nm that is most likely related to the interaction of the Co quadrupolar acoustic vibrations with the electric field generated by the SPR of the Ag nanolentils.

The experimental results presented have also been compared to theory, which has allowed relating the morphology of the nanostructures with their optical properties, and at the same time, studying different couplings: plasmon-plasmon (between nanocolumns) and plasmon-vibration in the samples containing either Ag nanocolumns or Co and Ag layers of nanoparticles and nanolentils, respectively.

Spanish abstract

Se han desarrollado nuevos conceptos de fabricación de materiales nanoestructurados en lámina delgada basados en el depósito por láser pulsado alterno de un metal (Ag) y un dieléctrico (Al_2O_3), que han permitido alcanzar un control óptimo sobre los parámetros morfológicos de las nanoestructuras que determinan su respuesta óptica. Se han producido nanoesferas, "nanolentils" y nanocolumnas auto-ensambladas orientadas. Se ha correlacionado su respuesta óptica lineal con su morfología y se ha simulado la respuesta óptica utilizando diferentes modelos teóricos. En paralelo al estudio óptico, se ha analizado la respuesta vibracional de las nanoestructuras mediante dispersión Raman de baja frecuencia. Por último, se han fabricado nanoestructuras que contienen capas alternas de nanopartículas de Co y de Ag separadas por una distancia de unos pocos nanometros, en las que se ha observado que la interacción entre el plasmon superficial y los modos vibracionales esferoidales de las nanopartículas activa la señal Raman.

French abstract

Nous avons développé de nouveaux concepts de fabrication de matériaux nanostructurés en couche mince basés sur le dépôt par ablation laser alterné d'un métal (Ag) et d'un diélectrique (Al_2O_3). Cette technique permet d'atteindre un contrôle optimal sur les paramètres morphologiques des nanostructures qui déterminent la réponse optique des couches minces. Nous avons produit des nanosphères, des "nanolentils" et des nanocolonnes, auto-organisées et orientées, encapsulées dans une matrice d'alumine amorphe. Leur réponse optique a été étudiée en fonction de leur morphologie et comparée á des simulations théoriques. En parallèle á cette étude, la réponse vibrationnelle des nanostructures a été analysée par spectrométrie Raman basse fréquence. Finalement, des nanostructures contenant des couches alternées de nanoparticules de Co et d'Ag séparées par une distance de quelques nanomètres ont aussi été fabriquées. Il a été montré que l'interaction entre le plasmon de surface et les modes sphéroïdaux de vibration des nanoparticules active le signal Raman.

Acknowledgements

I express my deepest and sincere gratitude to my supervisors Prof. Adnen Mlayah and Dr. Jose Gonzalo (Pepe). Adnen helped me to find this opportunity in Madrid which has been a very good experience. That would have probably not been the case without Pepe, he welcomed me, and helped me to accommodate to the new life that was waiting me in Madrid. By telephone, e-mail or in live they constantly support, guide, and encourage me, giving me freedom and confidence necessary for doing innovative research. The numerous discussion about physics or life have made me a better and confident person. I am grateful to them for giving me the impetus for completing the research experiments and writing this thesis.

It is a privilege to thank Prof. Carmen N. Afonso for her collaboration to my work, discussing my results and their interpretations, and for her criticisms and compliments that helped me to improving my skills of researcher. I have benefited from her expertise of researcher and learn a lot from her great capacity to communicate scientific results.

I wish to express my gratitude and regards to Dr. Lucien Saviot and Dr. Dan Murray, for their theoretical investigations of the nanoparticles vibrations; Prof. Peter Lievens, and Dr. Alexey Dobrynin, for the magnetic measurements; Prof. Gustaf Van Tendeloo, Dr Marta-Dacil Rossell Abrodos, Dr. Ute Hörmann, Prof. Carmen Ballesteros, and Isabel Ortiz, for the TEM and STEM measurements; Prof. Boris Luk'Yanchuk, Dr. Hong Ming Hui, and Zhou Yi; for their theoretical investigations of the SPR. I want to have a special thought for Prof. Boris Luk'Yanchuk, who teach me a lot during my stay in Singapore: “step by step”.

I am grateful to Drs. Guillaume Bachelier and Arnaud Arbouet for letting me benefit of their experience as young researchers, and for encourage me when I was doubting.

I express my sincere gratitude to Prof. Javier Solis, Dr. Jan Siegel, and Dr. Ángel Perea, for fruitful discussions and for answering my questions patiently. I can never forget the time they spend with me in the laboratory or discussing about science and life. A special thought to Dr Miguel Jimenez, and Dr Paco Gordillo for the pleasent coffee breaks shared during my years of PhD.

My sincere thanks to all the persons working in the LPST, now moved to the CEMES, specially my university professors Prof. Jesse Groenen, Prof. Robert Carles and Prof. Vincent Paillard that give me the taste of physical science. Thank you.

I wish to thank Dr. Vincenzo Resta to help me starting with the experiments at the beginning of my stay at the Instituto de Óptica, and all the other students that I met in Madrid and in Toulouse during my PhD.

I acknowledge an I3P fellowship from the CSIC and the European Fund for providing financial support during my PhD and giving me the opportunity to stay during one month in Singapore.

I thank all my friends who supported me although they were far from here. I would like to thank my family for their moral support and encouragement, without which this work would not have been a success. Last but not the least, I would like to thank Sandrine that encouraged me when I need it.

Jérémie Margueritat

To my father, Guy, my mother, Ghislaine and my brothers and sister, Jean-Francois, Charles and Janouk. And to Sandrine who give me the courage to achieve this work.

Contents

Part I

Introduction

In his talk: "*There's plenty of room at the bottom*", given at an American Society meeting at Caltech in 1959, the physicist and chemist Richard Feynman[?] put the first stone of the future "*Nano-Technology*" building. Feynman anticipated the possibilities of organizing the matter at the nanometric scale. He underlined that from this nano-scale should arise new physical properties. For example, the physical properties of a metal object change when its characteristic size is reduced down to a few nanometers,[?,?] making this new material more competitive. This basic idea made its way during the sixties generating interest among the scientists and in 1974 Professor Norio Taniguchi from Tokyo Science University finally named this new field of investigation: "Nano-technology" and re-defined it as follows:"Nano-technology mainly consists of the processing of, separation, consolidation, and deformation of materials by one atom or by one molecule".[?] Finally, during the 1980s the definition of nano-technology was extended as a field of applied science and technology whose final goal is the control of matter at the atomic and molecular scale, typically 1 to 100 nanometers, and the fabrication of devices with critical dimensions that lie within that size range.

In addition to their indispensable roles in nanoscience, nanostructures are at the centre of the development of a broad range of emerging and exciting technological applications, while the potential applications of fundamental research in nanotechnology include goals such as improved electronics, sensors, biomedical devices, catalysts and futuristic ones such as nanorobots, molecular machines, molecular electronics, etc...[?,?] Thus, to satisfy the technological demand for ever-decreasing device feature sizes and ever-increasing device performances, it is imperative to explore size and shape-dependent optical,[?,?,?] magnetic,[?] catalytic,[?] thermodynamic,[?] electric transport[?] and electrochemical[?] properties of materials at the nanoscale.

Size, shape and nano-organization in the volume (or surface) of nanostructures are responsible for the modification of the physical properties, and thus, the synthesis method is critical to tune the physical properties at the nanometric scale. There are several methods to nano-design materials, each one being more or less efficient to control size, shape or organization. However, none of them are able to control all parameters at the same time. In particular, this work is focused to the study of metal nanoparticles (NPs) in which small variations of these parameters induce changes in the optical response.

Although NPs are often considered as an invention of modern technology, the use of noble metal NPs for "artistic" applications is not new at all. The first known uses date back from the Roman Empire. Artisans discovered that small quantities of gold powder diluted in the blend used to produce glass changed its color,[?] and what it was

(a) View of the glass at the day ligth (reflexion).

(b) View of the glass when held up to the ligth (transmission).

Figure 1: Lycurgus cup.[?]

more amazing: when looking at the light transmitted through the glass, this looked completely different. This must have been a tremendous innovation at the time, and unfortunately just one example of this technology has been preserved. Figure 1 shows the "*Lycurgus cup*" (4th century AD).[?] This extraordinary cup is the only complete example of a very special type of glass, known as dichroic, which changes color when held up to the light. The opaque green cup (Fig. 1(a)) turns to a glowing translucent red (Fig. 1(b)) when light is shone through it. This is due to the tiny amounts of colloidal gold and silver embedded inside the glass.**?**

During the Middle Age, as the height of the buildings increased, so did the size of the windows and the first stained glass windows were then produced for decorative purposes. Figure 2 shows a picture of a stained glass window dated from the XIII century, taken from the Chartres Cathedral (France). The technique was improved since the Roman empire and the variety of color was increased using new metal powders, such as silver or copper.

Indeed, the pottery from the Middle Ages and Renaissance often retain a distinct gold, silver or copper colored metallic glitter. This so called lustre is caused by a metallic film that was applied to the transparent surface of a glazing. The lustre originates within

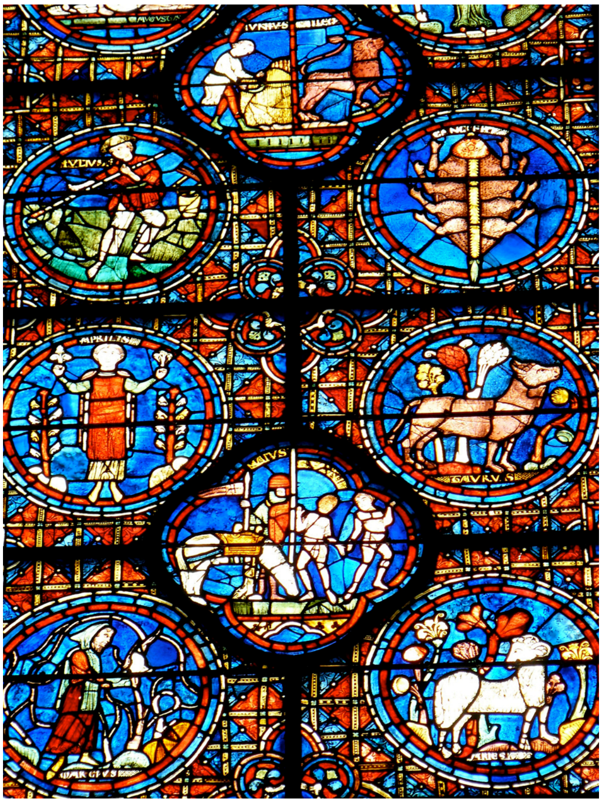

Figure 2: Stained glass window of Chartres Cathedral.

the film itself, which contains silver and copper nanoparticles, dispersed homogeneously in the glassy matrix of the ceramic glaze. They can be somewhat considered as the first nanocomposites.

However, the fabrication and use of nanoparticles remained essentially empirical for many centuries and it was only in 1857, when Faraday reported a systematic study of the synthesis and colors of colloidal gold.[?] He prepared the first pure sample of colloidal gold, which he called "activated gold". He used phosphorus to reduce a solution of gold chloride and demonstrated that the color of the solution was due to the size of the gold particles. In 1905 Maxwell Garnett formulated the first theoretical description of these results which relate the color with the size and volume fraction of NPs inside the glass. Finally, the pioneering work by Gustav Mie in 1908[?] proposed that the interaction of light with Ag NPs can give rise to collective oscillations of the free electrons commonly known as *surface plasmons*. Peaks appear in the extinction spectra whenever surface plasmons are excited by the electric field of incident light under resonant conditions.

All metal NPs have a surface plasmon resonance (SPR), however in most cases, the

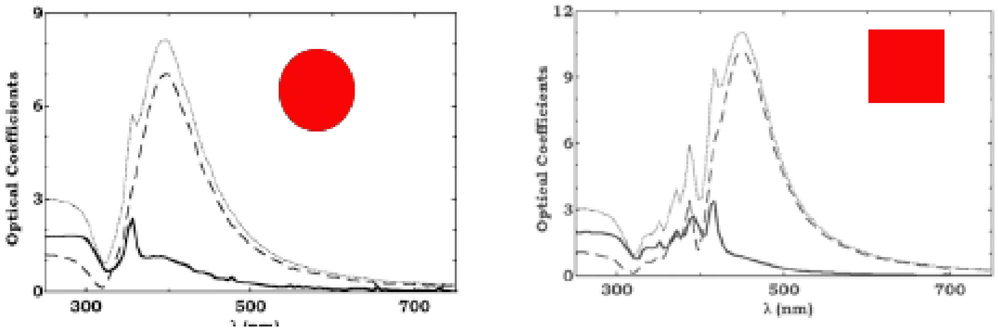

(a) Sphere.

(b) Cube

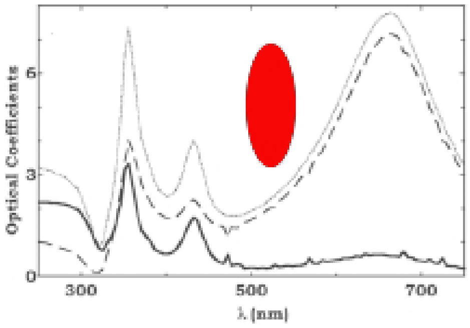

(c) Prolate ellipsoid.

Figure 3: Calculated spectra of the optical coefficients of silver nanostructures having different shapes.[?]

SPR is located in the ultra-violet range of the spectrum. In this respect, noble metals (Ag, Au and Cu) are unique since their densities of free electrons are in the proper range to give their NPs SPR in the visible region of the spectrum. Figure 3[?] shows calculated optical coefficient spectra for Ag NPs of different shapes. For a spherical Ag particle, the SPR is located around 400 nm (Fig. 3(a)). When the shape of the NP changes, the physical properties are modified, which induces changes in the optical response such as the appearance of multipolar SPRs (Fig. 3(b)) or the splitting of the SPR into different modes (Fig. 3(c)). Thus, the shape of the NPs is an important parameter for tuning the wavelength of the SPR. However, it is much easier to manufacture spherical NPs than to produce well controlled non-spherical shapes. Moreover, size and shape of the NPs are not the only parameters inducing change in the SPR. The environment is also an essential factor. The sensitive response of SPR peaks to environmental changes is interesting for many applications. It can be exploited to optically detect and monitor binding events on the metal NP surface, which lead to the realization of probes[?] or all integrated gas sensors.[?] Alternatively, they can be used for probing the interactions between small proteins,[?] SPR imaging detection of DNA hybridization[?] or SPR transmissions.[?]

A direct application of the NPs is surface enhanced Raman scattering[?,?] (SERS). This phenomenon has first been observed in the seventies for molecules deposited on rough metallic surfaces, through an enhancement of their Raman signal. This is related to the enhancement of the electromagnetic field in the vicinity of the metal roughness when excited close to the SPR. The efficiency of SERS increases when the rough surface is replaced by a high density of NPs deposited on a dielectric substrate. Moreover, the spatial organization as well as the control of the morphology of the NPs on large surface is actually a challenge since the enhancement of the Raman signal is related to the appearance of multipolar interactions between NPs.[?,?]

Guiding the light at nanometer scale is also important to develop all integrated optical systems. Linear chains of spherical Au or Ag nanoparticles can channel the light over distances of hundreds of nanometers without significant loss, using the interactions among the SPRs of the NPs.[?] The major requirement is the spatial organization of the NPs, since they must be separated by gaps narrow enough (<1 nm) to obtain an efficient coupling between the SPR modes. The use of different shapes might also be interesting. For example, the use of prolate ellipsoids in the linear chains would allow guiding different SPR modes by switching the polarization of the light.

The current challenge in producing solid systems containing NPs is the control and tuning of the SPR through nano-design of the NPs features and distributions. Indeed the response of nanocomposites formed by metal nano-objects embedded in dielectrics depends on the metal type, the substrate, the matrix, but over all on the size, shape, and organization of the NPs at the nanometric scale. It is essential to develop a synthesis method allowing to control all this parameters.

There are different approaches to produce such nanocomposites with controlled NPs morphology. They can be produced trough different physical or chemical synthesis techniques, and after their production, they can also be processed (thermally, with a laser, etc...) to enhance the quality of the nanostructures.

The methods based on chemical reactions in solution are widely used and one of the most popular is probably the citrate reduction method.[?] It consists in the preparation of Au or Ag nanospheres dispersed in water reducing $HAuCl_4$ in a boiling sodium citrate solution.[?] Another method is the seeded growth method. It uses preformed Ag or Au

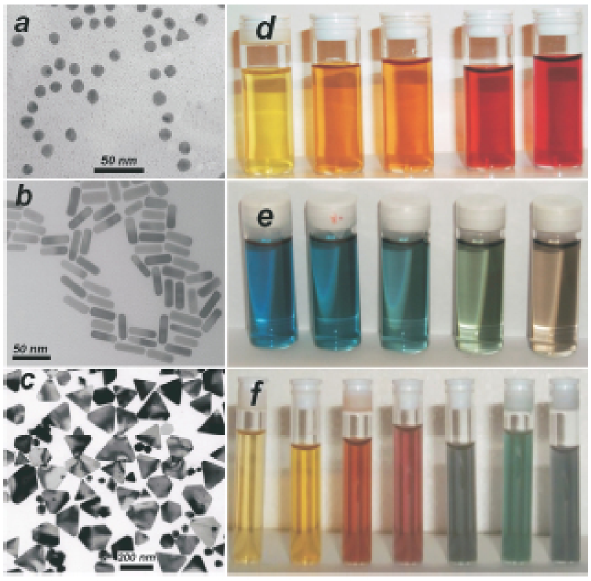

Figure 4: Left: Transmission electron micrographs of (a) Au nanospheres and nanorods (b) and Ag nanoprisms (c) formed using citrate reduction, seeded growth, and DMF reduction, respectively. Right: Photographs of colloidal dispersions of AuAg alloy NPs with increasing Au concentration (d), Au nanorods of increasing aspect ratio (e), and Ag nanoprisms with increasing lateral size (f).[?]

seeds on which additional metal is grown in solution by means of a mild ascorbic agent (ascorbic acid) allowing to produce elongated nanorods with controlled aspect ratio as a function of the paramaters employed.[?,?] Finally the DMF (N,N-dimethylformamide) reduction method reported by Liz-Marzan et al.[?] allowed the formation of anisotropic shapes such as nanoprisms. An overview of the results obtained using these methods is presented in Fig. 4,[?] which clearly evidence the influence of the size and shape on the SPR wavelength.

These methods allow tuning easily the shape of the NPs; but do not allow the spatial organization of NPs, for example on a substrate surface that is necessary in many applications. An alternative is the production of NPs directly on the surface or “inside” a matrix using, for example, the template method. This method allows synthesizing the desired material within the pores of nanoporous alumina[?] or polymer[?] membrane. Metals can be deposited within the pores of the template membranes by electrochemical reduction of the appropriate metal ions. Electrochemical deposition is accomplished by simply coating one face of the membrane with a metal film and using this metal film as a cathode for electroplating. An example of gold nanorods within the pores of alumina template membrane is shown in Fig. 5, where the dark regions are the gold nanorods.[?]

The main disadvantage of this technique is the template itself, since the size of the pores are limited to ≈50 nm. Thus one can only obtain rods with large diameters (≈40 nm).

Figure 5: Transmission electron micrograph of an alumina template membrane showing 70 nm diameter Au nanowires within the pores.[?]

A more versatile method for producing NPs on a surface with controlled dimensions, size, shape and organization is electron beam lithography.[?] In this case the substrate is covered with a conductive resin sensitive to electrons like PMMA. Then an electron beam is projected through a pattern to irradiate the resin. The exposed or non-exposed resin is eliminated through a chemical treatment. The metal is thus removed from the substrate leading to the pattern once the rest of the resin is eliminated. Despite the high degree of control that can be achieved with this method, the high cost, limitations in the minimum size of the NPs (≈20 nm[?]) and the maximum extension of the sample (≈ μm^2) prevents a wide spread use of this technique.

Angle resolved nanosphere lithography[?] is also interesting for spatial organization. In a first step, a nanosphere mask is self-assembled onto a surface followed by metal deposition trough this mask. In general the set mask/substrate is positioned normal to the direction of metal deposition, but an alternative method consists in tilting this set allowing a better control over the size, shape and separation between metal NPs. However, the minimum size of the NPs that can be produced is higher than 70 nm, and the preparation of the mask on a large area is difficult.

As opposed to the methods presented above, physical methods have the great advantage to produce NPs onto or inside a solid matrix on large surfaces (∼ cm^2). Ion implantation is one of them. Metal is implanted inside the matrix but in general, the size dispersion is large and post-implantation thermal treatment are typically required.[?,?] It is very difficult to achieve a good control over the morphology of the NPs, moreover, the depth of implantation is limited, which prevents control of the in-depth organization.

Thin film deposition techniques are more versatile methods since they allow producing not only NPs on a surface, or at a certain depth as ion implantation, but also nanocomposites in which metal NPs and matrix are produced in the same environment. The deposition process is made under controlled atmosphere (vacuum or gas) and materials with high purity and complex stochiometry can be produced. Among these methods, the more relevant ones are sputtering,[?,?] and pulsed laser deposition.[?,?]The sputtering technique is a physical vapor deposition process in which atoms in a solid target are ejected into the gas phase due to the bombardment of the material by energetic ions. However, this method has limitations drawbacks when producing certain type of materials such as good quality dielectric oxides. In Pulsed Laser Deposition (PLD) a high power pulsed laser beam is focused inside a vacuum chamber on a target of the desired composition. Material is then ejected from the target and deposited as a thin film on a substrate facing the target.[?] It is a very simple technique from the experimental point of view, since the target can have almost any geometry, and it does not require polarizing or cooling the target. PLD can occur in ultra high vacuum or in the presence of a background gas and the composition of the thin film reproduces quite well that of the target. In the configuration of alternate PLD , i.e. using a multiple target holder controlled by computer, it is possible to produce multilayers in a single step process. The characteristics of the deposit can be controlled trough several parameters such as the energy density of the laser, the number of laser pulses on the target, the pressure inside the chamber during the deposit, the configuration of the target-substrate holders, the use of static or rotating substrate holder, etc... Unique features of PLD are its pulsed character and the directionality of the expansion of the plasma generated by laser ablation. While the former favours deposition rates ($\sim 10^3$ nm.s^{-1}),[?] the latter induces a non homogenous deposit of the thin film.[?]

Earlier works performed at the "Grupo de Procesado por Laser" (GPL) of the Instituto de Óptica (IO) have demonstrated the high versatility of this technique for the production of nanocomposite thin films containing metal NPs (Au,[?] Fe,[?] Bi,[?] Ag,[?] Cu,[?] Co[?]) embedded in a-Al_2O_3. Moreover, there are many works from other groups reporting the production by PLD of other type of NPs (Au,[?] Si,[?] Co,[?] Pt,[?] Ge,[?] CdTe[?]) embedded in Al_2O_3, TiO_2 or ZnO. Until now, the works done in the LPG mainly studied the relation between the number of laser pulses used to ablate the metal and the morphological characteristics as well as the optical response of the nanocomposite thin films. In some cases, NPs embedded in a-Al_2O_3 have also been produced using different ablation fluences for the metal[?,?] or for the a-Al_2O_3[?] matrix. These earlier works have shown that the size and shape dispersions of NPs produced by PLD is quite reduced for small NPs (< 3 nm), but both increase when the average size increases. Thus, it is imperative to determine the parameters of the PLD or to develop an alternative process which allows reducing the size dispersion and controlling the shape.

Aim of this work

The aim of this work is to determine the experimental conditions that allows "nano-designing" nanocomposite systems containing embedded Ag NPs with small size dispersion and controlled shape and to relate their optical response to the NPs morphology. When the NPs are elongated (spheroids or nanorods) two distinct SPR bands related to transverse and longitudinal electron oscillations are observed in the optical response, and the latter SPR is very sensitive to the aspect ratio[?] of NPs. In this respect, it is challenging to produce elongated NPs with high aspect ratios to tune the longitudinal SPR into the near infra-red. We have chosen Ag as the metal because its SPR is well separated from interband transitions. To reach the objective we have extended the well known alternate deposition conditions for Ag NPs embedded in Al_2O_3.[?] The starting hypothesis is that reducing the in-depth separation between consecutive layers of Ag NPs until they became in contact, the NPs of the consecutive layers might connect and form a stack of NPs, that we will refered to as nanocolumns (NCls).

This work started with the study of the optical properties of Ag NPs as a function of the number of pulses used to ablate the Ag target. This allowed us to relate the morphology of the NPs with their optical properties. At the same time, the conditions to achieve a fine tuning of the a-Al_2O_3 thickness as a function of the pulse number were identified. In both cases the geometry of the target-substrate holders was optimized in order to obtain homogenous samples. Once this calibration process was completed we started to produce multilayers of Ag NPs decreasing the thickness of a-Al_2O_3. These samples were first characterized by electron microscopy to relate the morphology of the NPs with the parameters used to produce them, and thus, to demonstrate that it is possible to nano-design NCls using a-PLD. In order to demonstrate that we were able to tune the SPR, a systematic study of the optical properties of these samples as a function of angle of incidence and polarization of the light was performed. The experimental results were analyzed within Mie theory and its extension to anisotropic isolated NP (Rayleigh-Gans). The discrepancies between experimental and theoretical results required to introduce a new parameter: the density of NPs, and for this reason we also used an effective medium theory (Maxwell-Garnett). More recently one of our collaborators[*] also made more precise calculations using the open source DDSCAT[?] code.

To solve this problem we had used a different type of spectroscopy, i.e. the low frequency Raman spectroscopy (LFRS), which gives access to the vibration modes of the NPs. The study of the metal nanostructures, by LFRS, has been initiated by Gersten in 1980, with the first observation of vibration modes in rough copper and silver electrodes.[?] Since then, several works have been performed in this direction and especially for NPs.[?,?,?,?,?,?,?] It has been demonstrated that the acoustic vibration of a metal NP is directly related to the size of the particles and, in particular, Lamb theory[?] provides excellent results for estimating NP size. It has also been shown that the vibration of the NPs depends on their geometry,[?,?] and as in the case of the SPR, the vibration modes split into different branches when the NPs are anisotropic. Finally, Bachelier et al. demonstrated that the vibrations of the NPs are directly related to the SPR,[?] since the vibration modulates the polarization at the surface of the NPs which affects the oscillating electrons and thus the SPR. These experiments were performed in Toulouse at the LPST and the interpretation of the results were performed in collaboration with several researchers around the world[†]. The results were then compared to the morphology and the SPR features. The results show that combining extinction spectra and LFRS, which are both accesible and non destructive techniques, one can assess the morphology of NPs.

In parallel to this work, small spherical Co and CoO NPs were produced to study their magnetic properties in collaboration with different research groups[‡][§]. The most important results of these fruitful collaborations can be found in references.[?,?,?] We used the knowledge obtained in producing Ag and Co NPs to produce complex nanocomposites formed by pairs of Ag and Co NPs layers with well defined separations. Since Ag and Co NPs have specific optical and magnetic properties, respectively, when they are separated, the first aim was to study the effect of this coupling on the magneto-optical

---

[*] Dr A. Arbouet, CEMES, Toulouse, France

[†] D.B. Murray, University of British Columbia, and L. Saviot, Université Carnot de Bourgogne

[‡] Prof. Peter Lievens, and his team, Katholieke Universiteit Leuven

[§] Prof. G. Armelles and his team, Instituto de Microelectronica de Madrid properties of these samples but, as it happens some times in research, the results obtained were not concluding. However, we decided to study these samples using LFRS to further investigate the relationship between SPR and acoustic vibrations. This allowed us detecting the vibration of Co NPs when their distance to Ag NPs decreases. The size parameters were used to calculate[*] the electric field generated by the SPR in the vicinity of a Ag NPs. This allowed us to demonstrate that the vibrations of Co NPs are excited when the NPs are located in the near field generated by the SPR of the Ag NPs.

Structure of this work

The work is divided in five parts. Part I introduces the work.

Part II focuses on the nano-design. It starts describing the alternate PLD technique: history, principle and experimental setup (Chapter 1). It is followed by the description of the protocol used to nano-design our samples (Chapter 2). Finally, we present the morphology of the samples obtained by this method of production (Chapter 3).

Part III introduces the theoretical optical and vibrational properties of nanocomposite thin films containing NPs. We start with the simple case of a bulk metal (Chapter 4) and then, as dimensions are reduced, we present the special properties of metal NPs (Chapter 5).

Part IV presents the optical properties of the thin films produced. The techniques used to acquire the spectra and the special configuration used to study the splitting of the SPRs and vibrations are first shown (Chapter 6). Then we present the results, and analyze them within the theoretical models (Chapter 7). Finally, the SP-SP and SP-vibration coupling are discussed (Chapter 8).

Finally, Part V concludes this work.

---

[*] Boris Luk'Yanchuk and his team at the Data Storage institute in Singapore.

Part II

"Nano-Design"

1

Alternate-Pulsed Laser Deposition of Thin Films

Pulsed laser deposition (PLD) is one of numerous physical thin film deposition techniques. Other methods include molecular beam epitaxy (MBE) or sputtering deposition (RF, Magnetron, ...) for instance. In comparison PLD offers a higher flexibility including a wider choice of target material, laser parameters, target-substrate geometry, and ambient gas and pressure. The PLD technique is based on laser-matter interaction process: a high power pulsed laser beam is focused inside a vacuum chamber to strike a target of a material from which we want to produce a thin film. If the power density is high enough, material is ejected from the target surface, generating a plasma that expands along the direction normal to the target surface. Finally, if a substrate is placed in an appropriate position, a fraction of the ejected material is deposited leading to the growth of a thin film. The experimental conditions: laser fluence, substrate temperature, type and pressure of ambient gas, and geometry of the target-substrate system, determine the characteristics of the deposited films. For example, film growth can take place either in ultra high vacuum or in the presence of a background gas, such as oxygen, which is commonly required when depositing oxides.

In this chapter the basic concepts of the PLD technique are introduced. However, a detailed description is out of the scope of the present work and can be found elsewhere.[?]

1.1 Pulsed Laser Deposition

1.1.1 Introduction

History

The history of laser-assisted film growth started soon after the technical accomplishment of the first laser in 1960 by Maiman.[?] In 1962, Breech and Cross[?] showed the ablation of material by laser radiation and studied the laser-ejection and excitation of atoms from solids surfaces. Few years later, in 1965, Smith and Turner demonstrated for the first time the deposition of thin films by ablating materials such as stibnite, ZnTe, PbTe or Ge, with a pulsed ruby laser.[?] However, the quality of the deposited films was not as good as that obtained by other techniques which prevented the development of the technique. In the early 1980's, a few research groups achieved remarkable results on manufacturing thin film using lasers; but the real breakthrough came in 1987 when Dijkkamp and coworkers[?] used PLD to produce thin films of the then new high-temperature superconductor $YBa_2Cu_3O_{4-\delta}$ (YBCO) with a control over the crystalline quality and the stoichiometry superior to that achieved with any other physical and chemical deposition technique. Since then, PLD has demonstrated its potential to produce high quality crystalline and amorphous films, including ceramic oxides, nitride films, metallic multilayers and various superlattices among other materials. Today PLD is recognized as the best technique for the deposition of oxide thin films. Finally, the development of alternate PLD, which is based on the sequential ablation of different materials, has allowed during the last decade depositing complex structures in thin film configuration such as thin films composed by metallic nanoparticles embedded inside an oxide matrix and multilayers structures.[?,?] Nowadays, the development of new laser technologies, i.e. more competitive lasers having higher repetition rates, energies and new wavelengths, has made PLD a very competitive tool for the production of thin films with well defined complex stoichiometry and complex structures.

Basic principles

The most important deposition parameters concern the laser (e.g. wavelength, pulse duration, beam profile and pulse energy), the target (e.g. density, absorption coefficient, thermal conductivity, melting temperature, target morphology), the substrate (e.g. material, crystallinity, temperature), the deposition geometry (substrate placed in or out the expanding plasma), and the gas background (e.g. type of gas and its pressure).[?] The appropriate choice of them will determine the final characteristics of the deposited material.

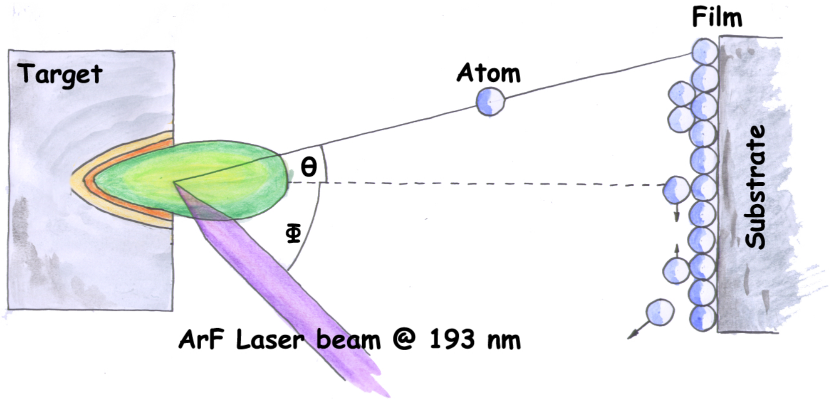

Figure 1.1: Ablation and deposition processes

The processes involved in the film growth by PLD are schematically summarized in Fig. 1.1. A pulsed laser beam is focused on a piece of material we want to grow in thin film configuration: *the target*. Focusing the laser beam results in a high energy density (*fluence*) on the target surface, inducing an increase of the temperature immediately followed by the melting and then the ejection of the material. This ejected material is partially ionized and highly excited, and behaves as a transient plasma, which explains the light emission. Due to its shape this plasma is also known as *"plume"*.

Figure 1.2 shows the light emission of a Ag plasma, the Ag target being ablated using an Excimer UV laser at 193 nm. The kinetic energy of ejected species depends on the angle of incidence of the laser, Φ, and their ejection angle, θ with respect to the target normal (Fig. 1.1). The plasma expands primarily along the normal to the target surface. In this configuration, a fraction of the ablated species reaches the substrate leading to the growth of thin films. Different processes, as diffusion, adsorption, or desorption, may take place at the substrate surface depending on the kinetic energy of the species reaching the substrate. In addition, PLD differs from other physical thin-film deposition

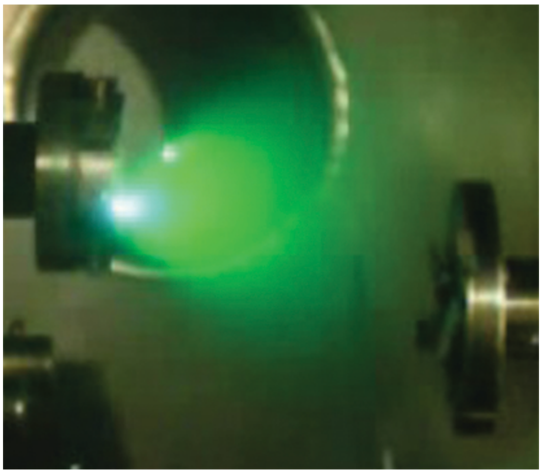

Figure 1.2: Plasma plume produced by laser ablation of a Silver target.

techniques by a relatively high instantaneous deposition rate (10^3 nm s^{-1}) and by a significant fraction of ions reaching the substrate with high kinetic energy.

Plasma generation and expansion

When laser radiation is absorbed in the surface region of a condensed-matter target, the electromagnetic energy is immediately converted into electronic excitation in the form of plasmons, unbound electrons and, in the case of insulators, excitons. The response is regulated by the optical and thermal properties of the target. For pulses longer than 20 ps, ablation is mainly thermally driven. The excited electrons transfer their energy to the lattice within a few picoseconds and heating begins within the optical absorption depth of the material $1/\alpha$, where α is the optical absorption coefficient. Then the ejection of atoms from the bulk material induced by the laser pulse occurs in a non-equilibrium state.

Ablation of metals is somehow different. Since the penetration depth is typically of 10 nm. Thus, all the photonic energy is absorbed into this very thin layer, and is efficiently transfered to the rest of the target due to its high thermal conductivity. Moreover, for ns pulse ablation, the situation is complicated by ionization of the nascent erosion cloud before the laser pulse is over, which has the effect of dissociating species ejected from the surface.

The temperature of the plasma is typically few thousands of kelvin degrees. This plasma is characterized by an extremely high degree of supersaturation (10^5 J/mole), i.e. far away from the thermodynamical equilibrium, a high degree of ionization, and by the presence of species having high kinetic energies. Depending on the laser parameters and the background gases these kinetic energies can range from 10^{-1} eV to several 10^{2}'s eV.

Characteristics of PLD

One of the advantages of this technique is that the vacuum system is totally independent from the laser source. This implies that PLD can easily be adapted to different operational modes without any constraints imposed by the use of internally powered evaporation sources. This allows modifying the ablation conditions by modifying the laser parameters. Moreover, in the case of alternate PLD, targets of different materials are moved alternatively into the beam, thus allowing the alternate deposition of different materials leading to the growth of multilayer structures in a single step process, without breaking the vacuum conditions. The stoichiometry of the target is generally preserved in the deposited films. This makes PLD suitable for the deposition of complex oxides with the desired composition, although in many cases an O_2 background is required to achieve the stoichiometry.

1.1.2 Film growth mechanisms

The deposition of the material ejected from the target generally starts by the formation of small clusters on the substrate surface. The formation (nucleation) of these clusters involves several processes, as illustrated in Fig. 1.3. The species arrive to the surface at a rate that depends on their kinetic energies and therefore on the ablation parameters. These atoms can subsequently diffuse over the substrate or cluster surface, encounter other mobile atoms to form moving or fixed clusters, attach to pre-existing film-atom clusters, to be re-evaporated from the substrate or from a cluster, or be detached from a cluster and remain on the substrate surface.

All these processes depend strongly on the presence of a background gas and on the substrate temperature as they affect the kinetics of the plasma species and the mobility of the atoms on the surface, respectively. In this work all the samples have been produced in vacuum and at room temperature. Hence, the kinetic energy and the mobility of the species depend only on the laser parameters and target characteristics.[?]

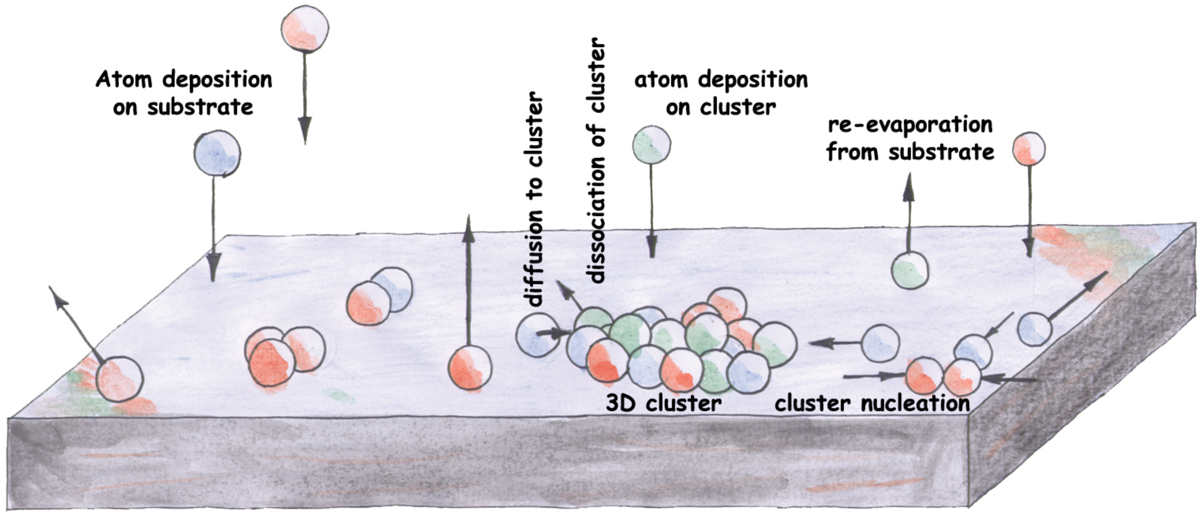

Figure 1.3: Possible nucleation mechanisms during film growth

The formation of clusters and their growth at the surface, depend mainly on the interaction energies of substrate atoms and atoms reaching the surface; i.e. adatoms. Perfect flat surfaces do not exist in nature, and defects, such as dislocations, vacancies, and edges, act as favorable nucleation sites. Thus, the comparison of the bond strength of the adatom with the substrate to the bond strength of adatom to its surrounding neighbors determines the initial stage of film growth. The relation between the surface energy of the substrate γ_s and the surface energy of the growing film γ_f is given by Young's equation,

$$\gamma_s = \gamma_i + \gamma_f \cos\phi, \tag{1.1}$$

where γ_i is the film-substrate interface energy and ϕ is the wetting angle of a nucleus on the substrate. Depending on the relative values of these interaction energies one can distinguish three modes of film growth[?] (Fig. 1.4):

- **a) Frank-van-der-Merwe**: *Layer-by-Layer growth*: In this case the interaction between substrate atoms and adatoms is higher than between adjacent adatoms ($\gamma_s > \gamma_f + \gamma_i$). Energetically, it is more favorable to form layers. Full-monolayer growth still involves the nucleation and growth of islands, but these are only one

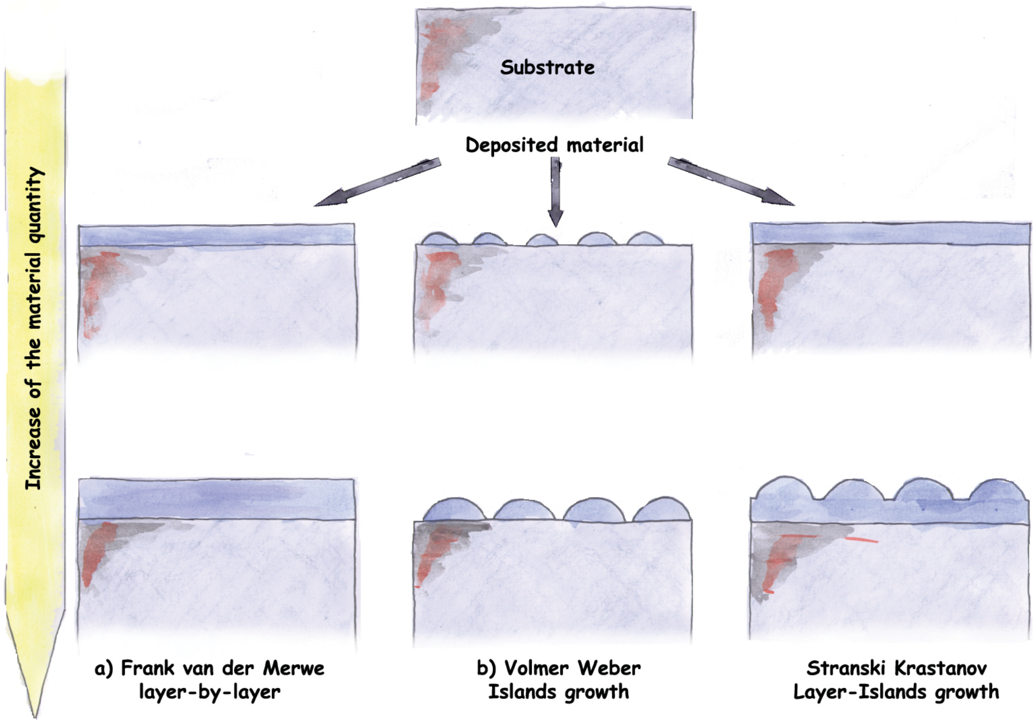

Figure 1.4: Possible film growth modes

monolayer thick and essentially lead to complete coalescence before significant clustering occurs.

- **b) Volmer-Weber mode**: *Island growth*: Separated three-dimensional islands are formed on the substrate if the interaction between adatoms is higher than between adatoms and substrate atoms ($\gamma_s < \gamma_f + \gamma_i$). Island growth occurs mainly by surface diffusion of adatoms, which leads to condensation of the adatoms in clusters and finally to the growth of islands.

- **c) Stranski-Krastanov mode**: *Layer-plus-Island*: This mode is an hybrid form of the two growth modes described above. The adatoms initially form complete monolayers (Frank-van-der-Merwe), typically 1 to 5 monolayers. Then, since the stress induced by the mismatched lattice spacings increases with the thickness of the deposited layer, adatoms begin to condensate on the surface and nucleate (Volmer-Weber).

Thin film growth mode will thus depend on the pair substrate-film atoms. The amorphous-Al_2O_3 (a-Al_2O_3) has been deposited on top of silicon (covered by a native

SiO_2 layer) or glass substrates, following in both cases the Franck-van-der-Merwe growth mode. Instead, we take advantage of the Volmer-Weber growth mode of a metal layer on top of an oxide surface to nucleate metal nanoparticles (NPs) on a-Al_2O_3.[?,?] If the amount of deposited metal is below a certain threshold, the atoms agglomerate forming NPs. Above this threshold, the distance among NPs decreases leading to coalescence of neighbouring NPs. Figure 1.5 is a simplified scheme of the coalescence process that can be defined roughly as “a melting of contiguous NPs into one unique NP”. If we increase the amount of metal above the coalescence threshold, the percolation of all NPs occurs and the process ends with the formation of a continuous layer. Then, the film follows the Franck-van-der-Merwe growth mode.

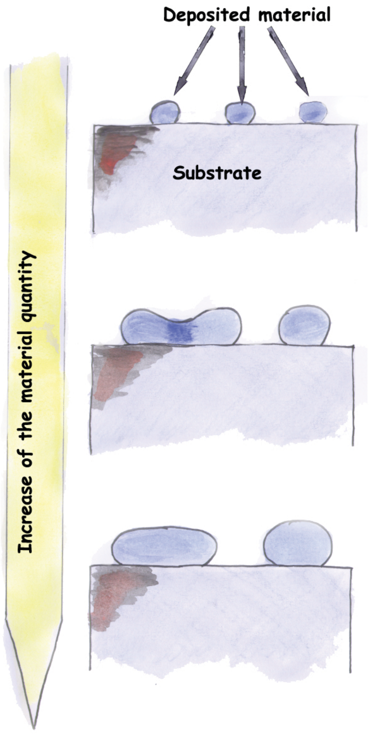

Figure 1.5: Schematic of the coalescence process.

1.1.3 Relevant features of PLD: Implantation and Re-Sputtering

As mentioned above, a significative fraction of species present in the plasma have high kinetic energies (>100 eV). These species can influence both positively and negatively the growth process, since they can either improve or deteriorate the overall morphology, stoichiometry, and microstructure of the growing film depending on their actual value of the kinetic energy.? In the negative side, the impact of high-energy species on the surface of the growing film can result in bond breaking, subsurface vacancy production and displacement or removal of surface atoms. Implantation and re-sputtering are direct consequence of these phenomena. Indeed, high speed species can be implanted into the substrate, meanwhile others can be ejected from the substrate (Fig. 1.6). Although it is possible to minimize these effects through an adequate control of the experimental parameters, they always exist and must be taken into account for better understanding of the final morphology of the samples.

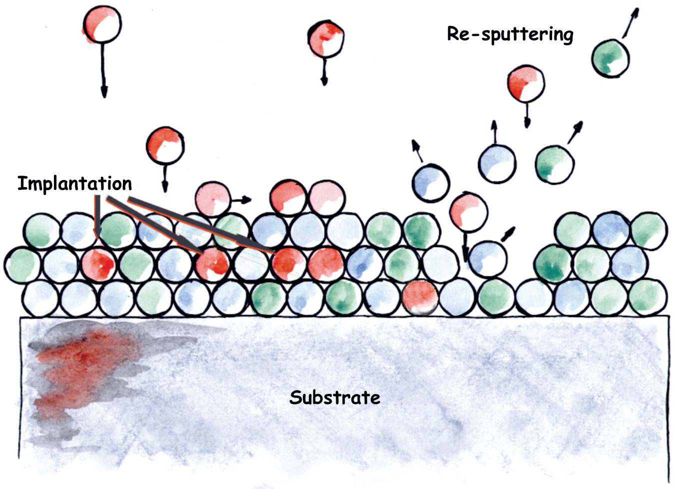

Figure 1.6: Schematic of the implantation and re-sputtering effects

1.2 Experimental equipment

The PLD set-up used in this work is schematically shown in Fig. 1.7. The main component is a stainless steel vacuum chamber containing target and substrate holders. An ArF excimer laser (Lambda Physics LPX 210i) operating at a wavelength, $\lambda_{ArF}=$ 193 nm and having a pulse duration of $\tau_{ArF}=$ 20 ns (FWHM) was computer controlled via a frequency generator.

The beam enters the vacuum chamber at an angle of incidence of 45° with respect to the target normal. A lens was used to focus the beam on the target surface (focal length = 250 cm). The spot size at the target surface was typically $\approx$ 0.02 cm^2 and the average fluence used 2.0 ± 0.2 J/cm^2. This fluence was kept constant for all the experiments. However, there is an uncertainty in the fluence related to the pulse-to-pulse

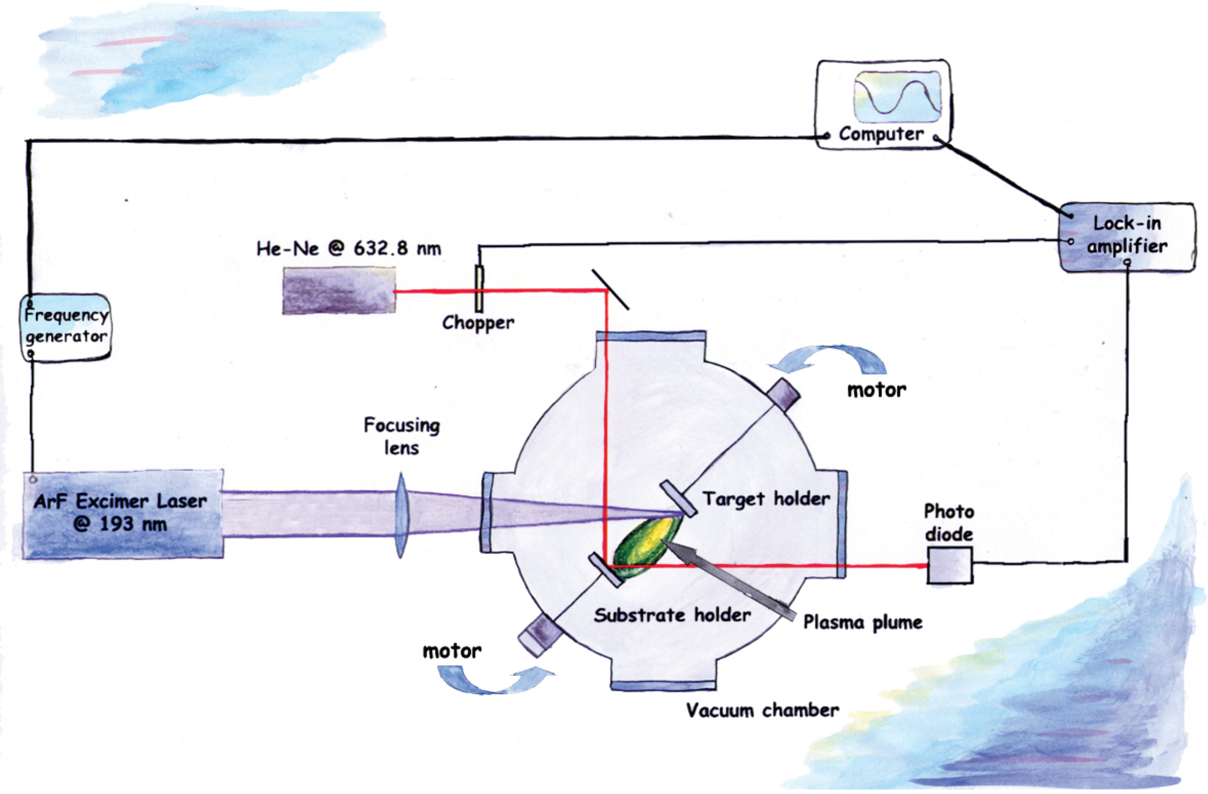

Figure 1.7: PLD experimental setup

energy stability ($\approx$ 10%) and the indetermination on the spot size. In all cases, thin films were produced in vacuum at room temperature. We used targets of Ag ($\geq$ 99.99%), Co ($\geq$ 99.99%), and polycrystalline Al_2O_3 that were pre-ablated prior to the deposition process to remove any possible surface contamination. The repetition rate was varied from $\nu = 5$ Hz to 20 Hz depending on the target type. Prior to ablation, the chamber was evacuated with a turbo molecular pump down to $p_1 = 2.0\times10^{-6}$ mbar, for Ag and Al_2O_3, and $p_2 = 8.0\times10^{-7}$ mbar for Co.

Target and substrate holders were both rotating and their relative geometries, shown in Fig.1.8, were chosen to improve the thickness uniformity of the deposit in a large area ($\approx$ cm^2). The substrate was placed at a distance of 35 mm in front of the target and rotated by an angle θ_{sub} of 32° with respect to the vertical. As shown in Fig. 1.8 it is possible to attach up to four targets and four substrates in their respective holders. This design has the advantage that multi-layered systems and several samples can be prepared without opening the vacuum chamber. To avoid any undesired deposition, three unused substrates are placed behind a protective screen. A mobile screen can also

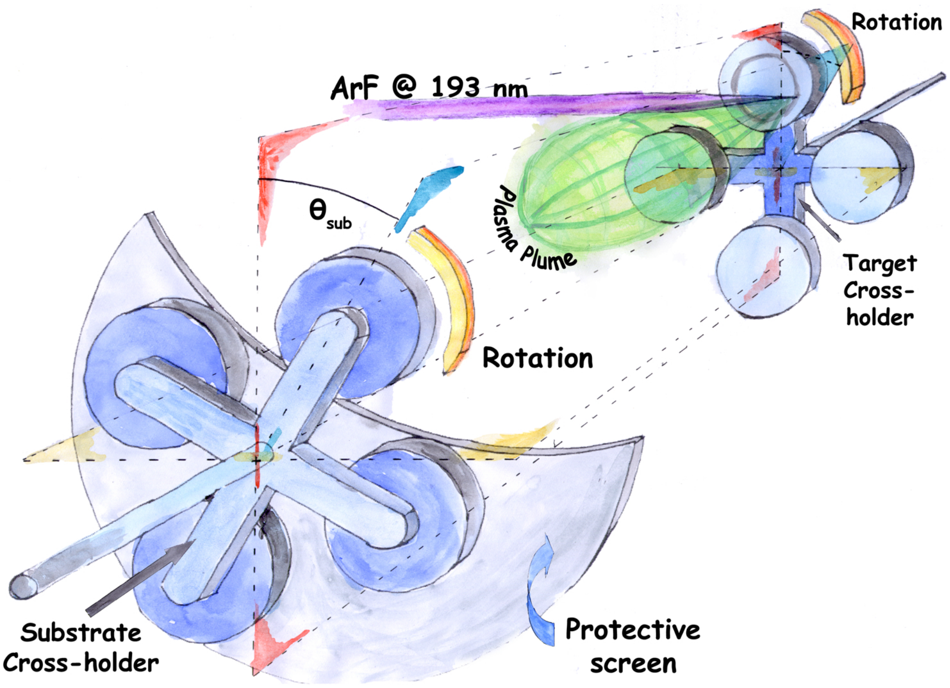

Figure 1.8: Geometrical configuration of the Target-Substrate holders system

be placed between the target and the remaining substrate to avoid deposition during cleaning of the target surface. The duration of an ablation sequence is defined by the number of laser pulses, laser frequency and the time required for the displacements of the target holders.

In this work, three types of substrates have been used: glass, silicon covered with its native SiO_2, and carbon coated mica. Prior to deposition, glass and silicon substrates were ultrasonically cleaned in a sequence of trichlorethylene, acetone, and ethanol. Glass was used for the optical characterization, whereas silicon and carbon coated mica were used for cross-section and planview imaging by electron microscopy. Samples were simultaneously produced on the three types of substrates to ensure that the film structure was the same.

Film thickness and growth rate were determined by "in-situ reflectometry" using a He-Ne laser (λ_{HeNe}= 632.8 nm) and a lock-in detection technique. This measurement was performed on a silicon substrate since it leads to a better reflectivity contrast. However, the change of substrate type does not have a significant influence on the growth rate. A more complete description of the reflectivity measurements is given in Chapter 2.

2

Nano-Design with a-PLD

Whatever the technique used, the requirement for material nano-engineering is always the same: ***control over the size and shape parameters of the nanostructures with a high precision and reduced size dispersion***. This chapter presents the protocol, developed in the GPL during the last years, used to embed metals NPs in an oxide matrix. This protocol takes advantage of the special features of PLD described in Chapter 1. After a short description of the relevant features for the implementation of the structures presented in this work, detailed guidelines for metal:oxide nanocomposite preparation using PLD are given. These guidelines describes the production of structures containing multilayers of NPs and nanocolumns (NCls) produced in this work.

2.1 Control of deposition rates

In order to achieve the required size control, it is first necessary to relate the deposition rate to the characteristic size parameters of both the a-Al_2O_3 matrix (layer thickness) and metal NPs (average diameter).

Amorphous-Al_2O_3 deposition rate

The deposition rate of a-Al_2O_3 is determined from “in-situ” reflectivity measurements obtained during deposition.

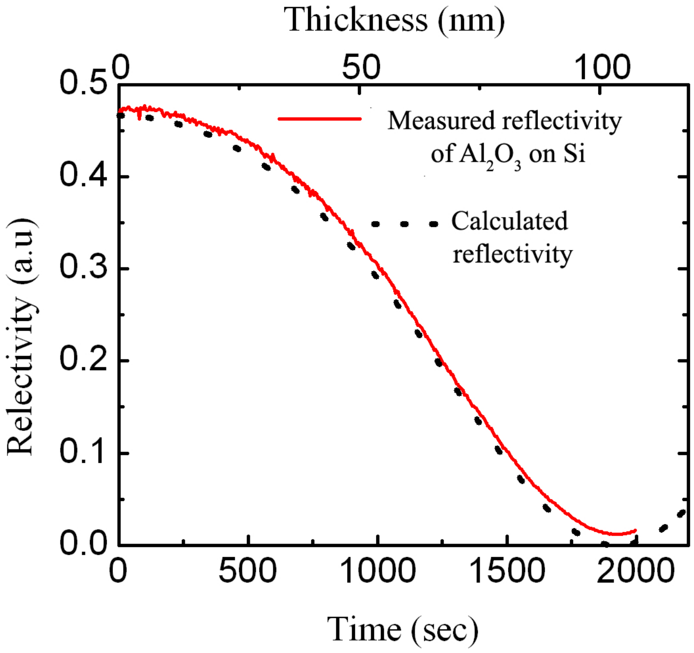

Figure 2.1: Simulated and measured reflectivity (632.8 nm) of a growing a-Al_2O_3 film on silicon as a function of film thickness and ablation time respectively.

Figure 2.1 presents the reflectivity of a growing a-Al_2O_3 on top of a silicon substrate simulated using the refractive index of a-Al_2O_3 deduced from previous measurements? and considering that the film grows in the Franck van der Merwe mode. The experimental data obtained with a repetition rate of 20 Hz are compared to the simulated data. The observed behavior is typical of dielectric materials on absorbing substrate showing interference maxima and minima as thickness increases. The comparison of R_{exp} and R_{sim} allows converting time into thickness (bottom and top horizontal axis of Fig. 2.1, respectively). In the experimental conditions used in this work, we have determined an average deposition rate of ~0.05 nm/s at 20 Hz, i.e 2.7×10^{-3} nm/pulse and we estimate that the precision over the total deposited thickness is close to ± 0.1 nm.

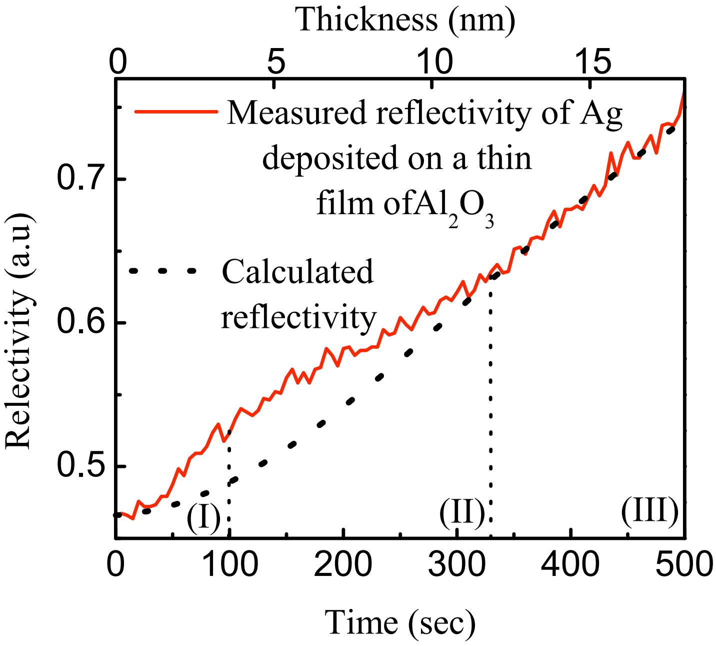

Figure 2.2: Simulated and measured reflectivity of a growing Ag film on a-Al_2O_3 as a function of film thickness and ablation time, respectively.

Metal deposition rate

The growth rate is more difficult to estimate in this case since metal strongly absorbs light. Figure 2.2 presents the simulated reflectivity R_{sim} of a growing Ag film on a-Al_2O_3, for which the metal film is again considered to grow in a layer-by-layer mode. The simulation does not take into account the formation of metal clusters on the oxide surface. However, the measured data does evidence this fact as it is shown in Fig. 2.2 for a film deposited at a repetition rate of 5 Hz. We observe that the real reflectivity, R_{exp}, is higher than the simulated one at the initial stages of growth while for longer times both the experimental and simulated values become similar. This initial difference is the signature of metal NPs formation. Thus, it is possible to distinguish three regimes in the growth process of metal on an oxide surface.

- **Regime I:** Volmer Weber regime: Metals atoms form well separated NPs.
- **Regime II:** Coalescence regime: The amount of metal deposited is large enough for NPs becoming close enough and coalesce.

- **Regime III:** Franck van der Merwe regime: The percolation threshold has been reached. The space among the NPs is filled and metal growth follows a layer-by-layer mode.

The separation between regimes **I** and **II** is only approximate. We consider it occurs when $\Delta R = R_{exp} - R_{sim}$ is maximum. Therefore, it is necessary to remain in regime **I**, to achieve control over the morphology of the NPs, as coalescence is a random process, which prevents precise control.

Thus, in regimes **I** and **II**, the ablation time is first related to the equivalent thickness of metal if the metal layer were continuous. From this value, it is possible to deduce the average diameter knowing the NPs number density on the surface. Figure 2.3 shows schematically the relation between the equivalent thickness of Ag X_{Ag} and the final diameter of the Ag NPs D_{Ag}.

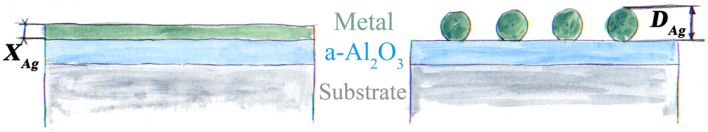

Figure 2.3: Schematic view showing the relationship between X_{Ag} and D_{Ag}

If we consider an area of 1 cm^2, the volume occupied by X_{Ag} nm of silver is:

$$V\ (\mathrm{nm})^3 = X_{Ag} \times 10^{14} \tag{2.1}$$

This volume is equal to that occupied by the NPs whose number density is ρ_{NPs} expressed in (NPs/cm^2). If we consider that all NPs are spheres of diameter D_{Ag}, the diameter of one NP is:

$$D_{Ag}\ (\mathrm{nm}) = \left(\frac{6}{\pi \rho_{NPs}} \times 10^{14} X_{Ag}\right)^{1/3} \tag{2.2}$$

For example, if the number density of Ag NPs is ρ_{NPs} =8×10^{12} NPs/cm^2 and X_{Ag}=2 nm, the diameter of the NPs should be D_{Ag} ≈3.6 nm. However the areal density of NPs produced by PLD, ρ_{NPs}, depends on the NPs size.[?,?] Thus, it is necessary to calibrate the morphological characteristics of the NPs as a function of the number of pulses used to ablate the target. Fortunately, such a calibration is available from the previous experience of the GPL? in the deposition of Ag NPs. Concerning the case of Co, this calibration has been done during this thesis.

Equivalent thickness of a-Al_2O_3

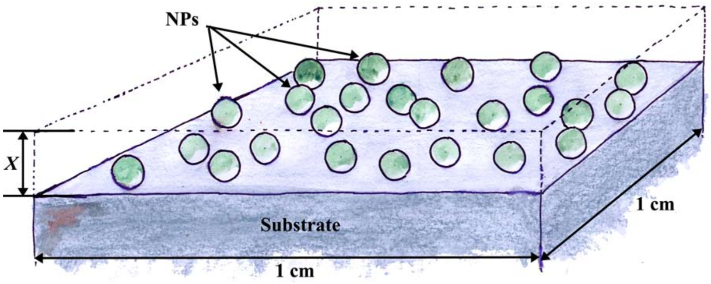

Figure 2.4: Schematic showing the relationship between X_{Ag} and D_{Ag}

In the previous cases we have considered that the substrate surface is perfectly flat. Yet, the NPs are embedded, which means that the layer of a-Al_2O_3, that covers them, is deposited on a rough surface. The result will be a nanocomposite layer formed by metal NPs embedded in a-Al_2O_3 matrix. In this case, for the same deposition time of a-Al_2O_3, the layer produced will be apparently thicker than the value determined using the procedure described above.

Then, it is also necessary to introduce the concept of equivalent thickness of a-Al_2O_3 to tailor correctly the nanostructures. In this case, the value is defined as the thickness of a-Al_2O_3 deposited among the space between NPs, i.e. the thickness of the nanocomposite layer, plus the thickness of the a-Al_2O_3 layer deposited further. Figure 2.4 presents a schematic to understand these considerations.

As a first step, it is necessary to determine the volume of a single NP (V_{NP}), which is defined as following:

$$V_{NP}\ (\mathrm{nm}^3) = \frac{4}{3}\pi \times a \times b \times c \tag{2.3}$$

where a,b and c are the three semi-axis in the general case of a non-spherical NP given in nm. Then the total volume ($V_{totalNPs}$) occupied by the NPs on a surface of 1 cm^2 is calculated as:

$$V_{totalNPs}\ (\text{nm}^3) = V_{NP} \times \rho_{NPs} \tag{2.4}$$

where ρ_{NPs} is the number density of NPs by surface unit. The total volume of the parallelepiped is defined as:

$$V_{totalpara}\ (\text{nm}^3) = 1 \times 10^{14} \times X \tag{2.5}$$

where X is the desired equivalent thickness of a-Al_2O_3 expressed in nm. The real volume of a-Al_2O_3 we need to deposit is the volume of a layer of thickness T, which is given by:

$$V_{a-Al_2O_3}\ (\text{nm}^3) = V_{totalpara} - V_{totalNPs} = T \times 10^{14}\ (\text{nm}^3) \tag{2.6}$$

Where T is the real thickness of a-Al_2O_3 required to obtain a nanocomposite layer having an equivalent thickness X. For example, an equivalent thickness X of 6 nm, that includes Ag NPs with diameter of 3 nm and number density of $8{\times}10^{12}$ NPs/cm^2, corresponds to a thickness T of 4.8 nm.

2.2 Production of complex nanostructures

Basic principle for the production of homogenous“multi-layered” thin films containing metal NPs

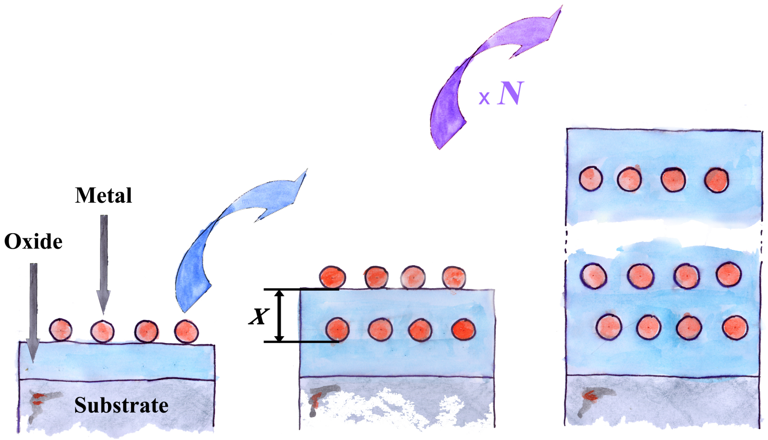

Figure 2.5: Schematic for the production of metal nanostructures

The deposition protocol is illustrated in Fig. 2.5 and described below.

1. Deposition of a thin layer of oxide. This layer acts as a buffer layer to smooth any possible defect as long as they are smaller than few nanometers as well as providing the same surface for NPs to nucleate in the multilayer nanostructure.

2. Growth of NPs. If the equivalent thickness, X_{Ag}, is lower than 5 nm, metal NPs will be produced.

3. Deposition of an oxide layer. The spaces among the NPs are first *"filled"* in leading to a continuous layer and then the desired thickness of oxide is deposited on top of it.

4. Repetition of steps 2 and 3 as many times (N) as desired.

5. Deposition of a final protective layer of oxide.

According to the structure of the desired thin film, the appropriate parameters (repetition rate, laser energy, deposition times) must be selected. The number of targets, the ablation sequence, the parameters in each step, etc... can indeed be modified to obtain more elaborated structures, such as those described in the following sections.

Production of heterogenous "multi-layered" thin films containing metal NPs.

Here we describe the extension of the growth protocol to the case of multilayers containing bilayers of Co and Ag NPs. Figure 2.6 shows cross-section schematics of one of these heterogenous "multi-layers" that consists of five "bilayers" of Co and Ag NPs layers embedded in a-Al_2O_3. The spacing between the bilayers was fixed to 25 nm. Co NPs are spherical and defined by their diameter $\boldsymbol{D_{Co}}$ while Ag NPs are oblate spheroids defined by their average diameter, $\boldsymbol{D_{Ag}}$ and height $\boldsymbol{H_{Ag}}$. The spacing X within the bilayers can easily be controlled through the deposition of the matrix following the procedure described above.

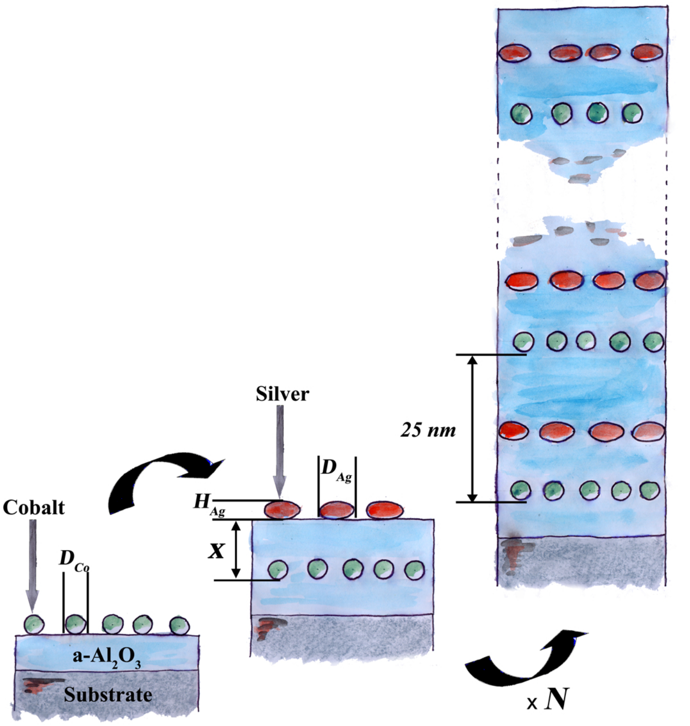

Figure 2.6: Schematic for the production of CoAg multilayers

The deposition protocol can be summarized as:

1. Deposition of a thin a-Al_2O_3 buffer layer.
2. Growth of Co NPs. The ablation time was chosen to obtain spherical NPs.
3. Deposition of an equivalent thickness X of a-Al_2O_3.
4. Growth of coalesced Ag NPs to obtain oblate spheroids.
5. Deposition of a second layer of a-Al_2O_3, having a thickness of $(25 - X)$ nm.
6. This protocol is repeated from the step 2 as many times as the number of desired bilayers.
7. The last layer of NPs is covered with an equivalent thickness of 10 nm of a-Al_2O_3.

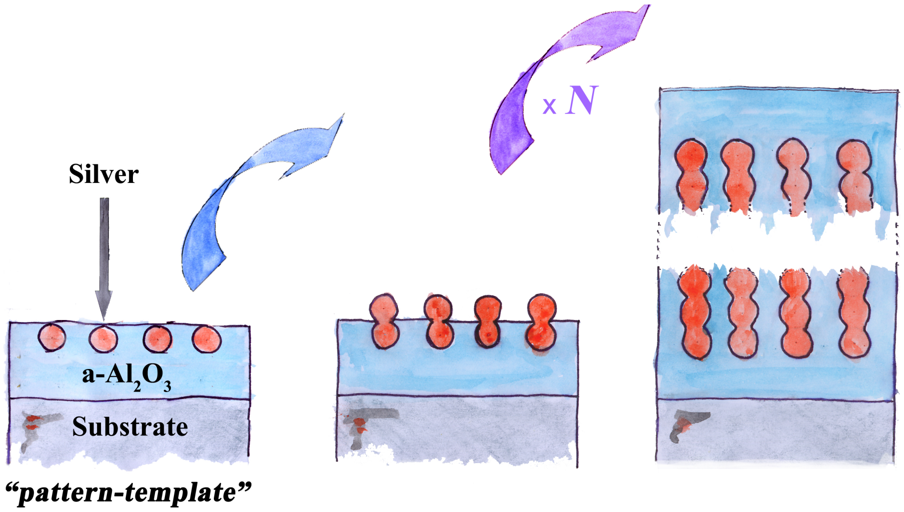

Figure 2.7: Schematic for the production of Ag NCls

Production of Ag NCls

The procedure used to produce NCls is an extension of the approach used to produce Co-Ag NPs bilayers. Figure 2.7 shows cross-section schematics of one film that consists of "multilayers" of Ag NPs embedded in a-Al$_2$O$_3$ with average diameters D_{Ag}. In this case, the spacing X between consecutive layers of Ag NPs was reduced down to values close to D_{Ag}.

The first layer of Ag NPs acts as a pattern that defines the number density and the diameter of the final NCls produced, while the matrix acts as a template allowing their oriented growth. The critical step for the production of NCls resides in the very precise control (i.e. within less than 1 nm) of the equivalent thickness of both metal and a-Al$_2$O$_3$.

The sequence can be repeated an arbitrary number of times N to increase the height of the NCls to lead to the situation sketched in Fig. 2.7. The produced NCls are oriented perpendicular to the substrate.

3

Morphology of nanodesigned structures produced by a-PLD

In Chapter 2 we have presented the protocols used in this work to produce the nanostructures. In this chapter we describe the morphology of the resulting Co:Ag:a-Al_2O_3 and Ag:a-Al_2O_3 nanocomposite thin films. First, we briefly present the techniques used for the morphological characterization of our samples. Then we describe the morphology of the samples produced and its dependence on the deposition parameters.

3.1 Electron microscropy

The morphology and structure of the films have been studied by transmission electron microscopy (TEM), high resolution TEM (HREM) and scanning TEM (STEM) in collaboration with M.I. Ortiz and C. Ballesteros from the University Carlos III of Madrid (Spain) and U. Hörmann, M.D. Rossell and G. Van Tendeloo from the University of Antwerp (Belgium). These three types of microscopies have been employed to access different types of information such as: NP size and morphology, NP distribution and crystallinity, and metal distribution.

The electron beam is generated in all cases by thermo-electronic emission from a tungsten filament. The beam is accelerated by a difference of potential of few hundred kV, whose value determines the wavelength of the electrons (typically 10^{-1} to 10^{-3} Å). It is then focused on the sample by a condensing electromagnetic lens. The whole system is in vacuum to avoid interactions of electrons with impurities and the beam transmitted through the sample is acquired using a CCD camera or a photographic plate.

In TEM (or HREM) images dark areas correspond to the material that absorbs the electrons. The material interacts with the electron beam mostly by diffraction, although the intensity of the transmitted beam is affected by the volume and density of the material through which it passes. Thus, dark areas in the TEM images correspond to a high electronic density, which in our samples corresponds to the metals. Using HREM (with a resolution of 0.2 nm) it is possible to obtain images of the lattice fringes of crystalline areas. In STEM, the process to obtain images is different as the electron optics focus the beam into a narrow spot which is scanned over the sample. By coupling the STEM with an electron dispersive X-ray (EDX) detector, it is possible to obtain atomic resolution images in which the contrast is directly related to the atomic number. Thus, bright areas correspond to the heaviest material, i.e. the metal in our case.

One of the challenges in electron microscopy is the preparation of samples thin enough (less than 15 nm) to allow the transmission of electrons. In the case of plan-view images, sandwich thin films were directly deposited on top of carbon coated mica substrates. These films consist of buffer and covering a-Al_2O_3 layers and a single layer of NPs in order to avoid overlapping images of NPs laying in different layers. They were separated from the substrate by immersion in de-ionized water and collected on top of 3 mm diameter grids. In the case of cross-section views, the preparation is much more complex. We have used two techniques to obtain samples thin enough. The first technique consists in polishing mechanically the sample to obtain 200 nm thick samples. The thickness of the samples is further reduced by dimpling and finishing with ion beam milling. This technique is time consuming and delicate. An alternative is the use of a focused ion beam (FIB) technique. It allows milling very thin membranes from a specific area of the sample. For this preparation we have used the FIB with internal lift out FEI Nova 200 NanoLab dual beam SEM/FIB system.

The microscopes used and their characteristics are summarized below:

- A Philips Tecnai 20F FEG, TEM/STEM operating at 200 kV with point-to-point resolution of 0.20 nm and equipped with an EDX detector, and a dark-field high angle annular detector for Z-contrast analysis. (Madrid)
- A JEOL 4000EX, TEM operating at 400kV with point-to-point resolution of 0.18 nm. (Antwerp)

3.2 Nanoparticles

Before presenting the results on the complex structures produced in this work, it is convenient to present some results obtained for the simple case of embedded NPs. Indeed, the essential point of the nano-design process is inherent to the NPs since the starting NPs morphology determines the properties of the complex nanostructures, and in the case of the production of Ag NCls, the nano-design itself.

As it was mentioned in chapter 1, NPs produced by PLD in vacuum are nucleated on the substrate surface and they evolve from small spheres to oblate ellipsoids due to coalescence. However, this evolution depends on the type of metal. The expertise of the GPL has shown that magnetic metals (such as Co,[?,?] Ni, Fe[?]) tend to form continuous layer very quickly, while noble metals (such as Ag,[?] Au[?]) coalesce in large NPs before forming a continuous layer. Thus, the obtainable Co NPs are always almost spherical with a diameter varying in the range from 2 to 4 nm. Instead, in the case of Ag NPs, the in-plane average dimensions of the NPs increases as the amount of Ag increases while the dimension along the direction perpendicular to the substrate surface remains smaller and tends to a saturation value.

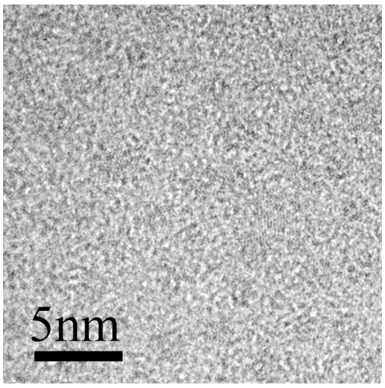

Figure 3.1: Plan-view TEM image of Co NPs in a-Al_2O_3.

Figure 3.1 shows the image of a sandwich film containing a single Co NPs layer embedded in a-Al_2O_3, grown on carbon coated mica. Since most particles are round and their size dispersion is quite small, we can conclude that the NPs are spherical with a mean diameter of 2.7 ± 0.3 nm and they are well separated from each other.

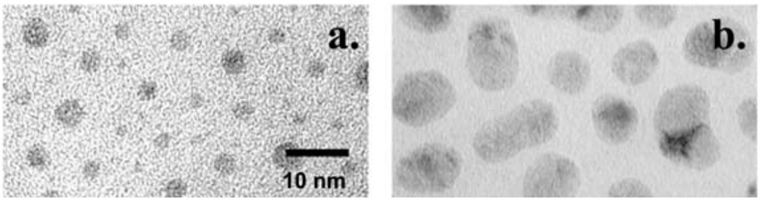

Figure 3.2: Plan-view TEM images of two samples containing (a) spherical and (b) coalesced Ag NPs embedded in a-Al_2O_3.

Figure 3.2 shows two TEM plan view images of Ag NPs produced using different deposition times before (Fig. 3.2 a.) and after (Fig. 3.2 b.) the onset of coalescence (Chapter 2). Figure 3.2 a. shows spherical NPs with an average diameter D_{sph}= 3.4 ± 0.2 nm. When the amount of Ag is large enough and the NPs start to coalesce (Fig. 3.2 b.), a fraction of the NPs simply increase their volume, while others "connect" to form ellipsoids. This leads to smaller number density of NPs and to the increase of size and shape dispersions. The NPs in Fig. 3.2 b. have an average in-plane diameter D_{obl}= 9 ± 1 nm and a height H_{obl}= 5.2 ± 0.2 nm.

The use of long deposition times leading to non-spherical NPs is a problem for the production of NCls, since once nucleated, the ellipsoidal NPs are randomly oriented on the surface and thus, it is extremely difficult to anticipate if the self-organization will be preserved.

3.3 Co-Ag bilayers

In order to study the relationship between spatial organization and optical properties of the nanocomposite thin films we have produced samples containing spherical Co and oblate Ag NPs pair of layers (bilayers) within which we have varied the separation, X, between the layers of Co and Ag NPs as described in Chapter 2.

Figure 3.3 shows cross-section HREM images of individual Ag and Co NPs where it is clearly evidenced the crystalline structure of both type of particles. The Ag NP is polycrystalline (Fig. 3.3 a.), while the small Co NP is monocrystalline (Fig. 3.3 b.).

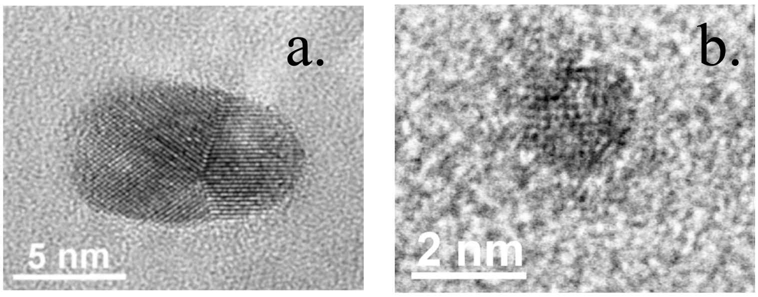

Figure 3.3: Cross-section HREM images of: (a) individual Ag NP which grew as random polycrystals; (b) individual monocrystalline Co NP.

These images also allowed us to determine the average heigth H_{Ag}= 6.0 ± 0.5 nm and diameter D_{Ag}= 10 ± 2 nm of Ag NPs, and the diameter D_{Co}= 3.0 ± 0.4 nm of Co NPs. To produce this sample the time deposition, t_{dep}, of Co and Ag was slightly longer than in the situations presented in the previous section, which explains the larger NPs sizes. However, plan-view and cross-section images confirm respectively the spherical and the oblate shape of the Co and Ag NPs, produced in this work.

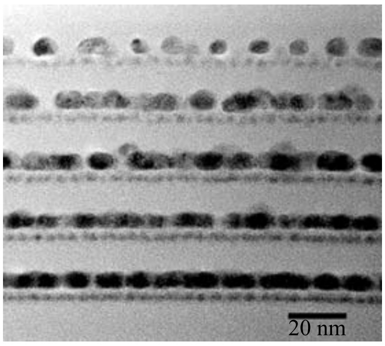

Figure 3.4: Cross-section TEM images of a thin film containing five pairs of NPs layers Co-Ag separated by 25 nm.

Figure 3.4 shows a cross section TEM image of a nanocomposite film containing layers of Co NPs and Ag NPs. The composite system is build up of five bilayers of NPs in which the large oblate NPs are made of Ag while the small spherical ones are made of Co. The structure is defined by the average in depth spacing X= 4.0 ± 0.2 nm between the layers of Co and Ag NPs within each bilayer and the spacing of 25 nm between bilayers. This image also shows the very good reproducibility achieved in the samples, which evidences the high degree of control achievable by a-PLD in the production of nanostructures.

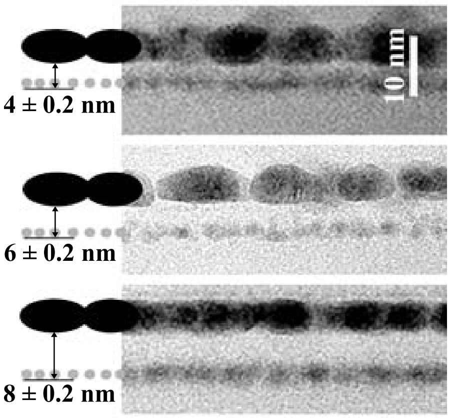

Figure 3.5: Cross-section TEM images. From top to bottom the images correspond to X= 4.0, 6.0 and 8.0 nm (The error is estimated to be $\Delta X \pm 0.2$ nm).

In this work we have only modified the in-depth separation between the Co NPs and Ag NPs layers of each bilayer while maintaining constant the size of Ag and Co NPs and the separation between bilayers. Figure 3.5 shows TEM images of three bilayers with different in depth spacings: X= 4.0 ± 0.2 nm, 6.0 ± 0.2 nm and 8.0 ± 0.2 nm. This image again illustrates that the reproducibility of the NPs size, is also preserved from sample to sample.

3.4 Ag nanocolumns

As presented in Chapter 2, the nanodesign of NCls is determined by the features of the NPs in the first layer. Once selected the deposition time of Ag in order to obtain Ag NPs with the correct size for the "pattern-template layer", the fundamental parameter that determines the formation of oriented NCls, consecutive planes of Ag NPs or randomly distributed nano-wires is the amount of a-Al_2O_3 deposited between consecutive layers of NPs. To analyze its influence, we selected a t_{dep}= 25 seconds for the Ag, which correspond to NPs having average diameter $D\approx$ 2 nm and a number of cycles N=5, while the thickness of the matrix layer was varied from X= $2D$ to X= $0.5D$. The cross-section TEM images are shown in Fig. 3.6.

For X= $2D$, no columnar growth occurs, instead the formation of 5 well separated layers of Ag NPs is observed. In this case, the value of X is large enough to totally cover the NPs with a thin layer of a-Al_2O_3 on which the following NPs nucleate randomly.

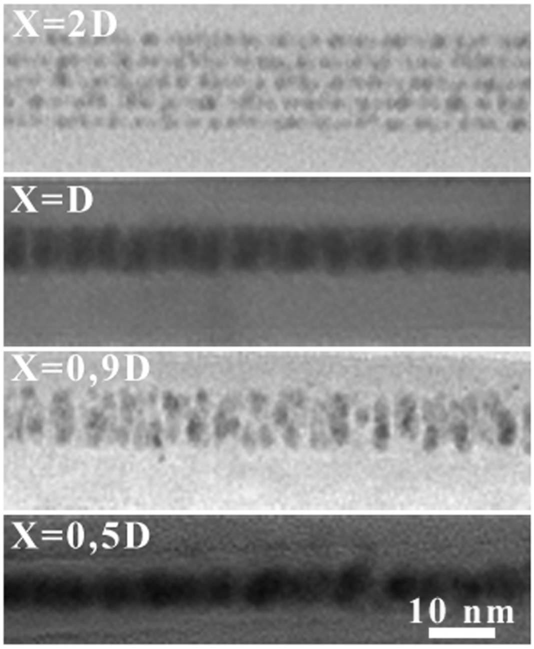

Figure 3.6: Cross-section TEM images of films produced using different effective thicknesses of the matrix layer X with respect to the diameter D of Ag NPs.

When decreasing X to D it is not possible to distinguish 5 consecutive layers of NPs. Instead, elongated dark areas perpendicular to the substrate (oriented along the growth direction) are observed. It is also seen that these elongated structures are well separated one from another for $X \approx D$.

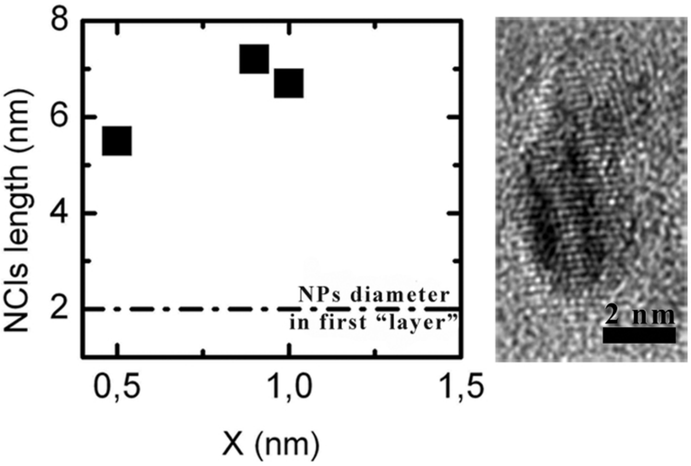

Figure 3.7: Height, H, of NCls as a function of the effective thickness of the matrix layer X and cross-section HREM image of one of the NCls produced with X=D.

If we reduce further X (X=0,9D), the height of the NCls slightly increases, but some discontinuities appear as if the thin film was composed by both NCls and NPs. Reducing X further down to $0.5D$ leads to a drastic decrease of the height ($5.5 \pm 0{,}2$ nm).

The height H of these elongated structures as a function of X is summarized in Fig. 3.7. The figure also shows a high resolution image of one of the NCls obtained for $X{=}D$ where lattice fringes are observed evidencing their crystalline structure. The NCls are not single crystals since regions having fringes with different orientations are clearly visible. This fact is most likely due to the growth procedure, i.e. each NCl is made from a stack of five NPs. From the results presented in Fig. 3.6 and Fig. 3.7 it is evident that the highest value of H and the best morphology is achieved for $X \approx D$.

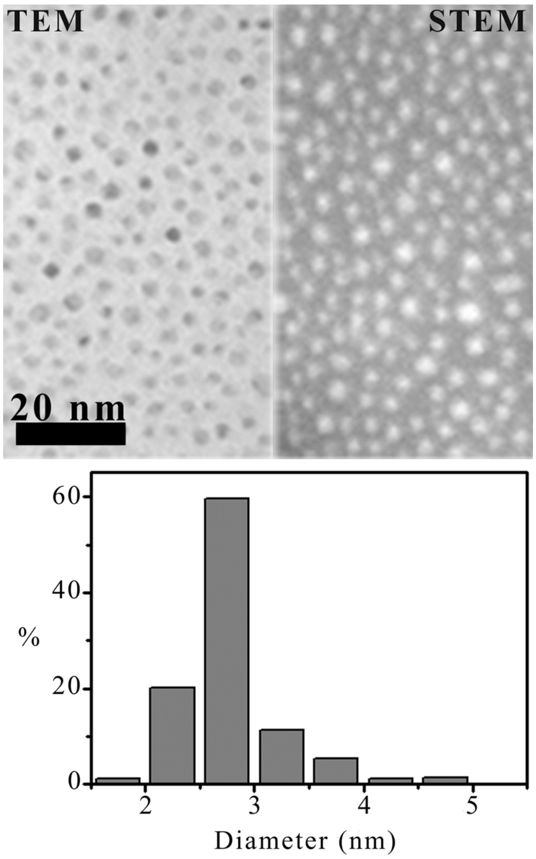

Figure 3.8: Plan-view TEM and STEM images of the sample produced with $X{=}D$, the latter being imaged with Ag signal. The plot includes the diameter dispersion measured from the TEM image.

Figure 3.8 shows plan view images of the sample grown with $X{=}D$ obtained both with TEM and STEM microscopy, the latter showing the areas having large concentration of Ag as bright areas. The good match of dark and bright areas in both images together with the X-ray fluoresence spectra confirms that the NCls are isolated and oriented in the direction perpendicular to the substrate. The NCls have an approximately round section of 2.7 ± 0.2 nm as shown in the histogram included in Fig. 3.8. It is worth to point out the very low size and shape dispersion achieved.

The results presented in this section confirm the efficiency of the protocol introduced in Chapter 2 for producing NCls. The pair "first layer of NPs + matrix" acts indeed as a "pattern-template" mask for the production of NCls. The next ablated metal atoms nucleate preferentially on top of the previous metal NP layer that is partially uncovered. This is due to the higher metal/metal than metal/oxide adhesion energy and the high mobility of the atoms at the surface due to the high kinetic energies involved in PLD.[?] This self-organization process leads to the production of self assembled NCls when the process is repeated a number N of times. The first layer of NPs constitutes thus the seeds for the NCls and determines their number density.

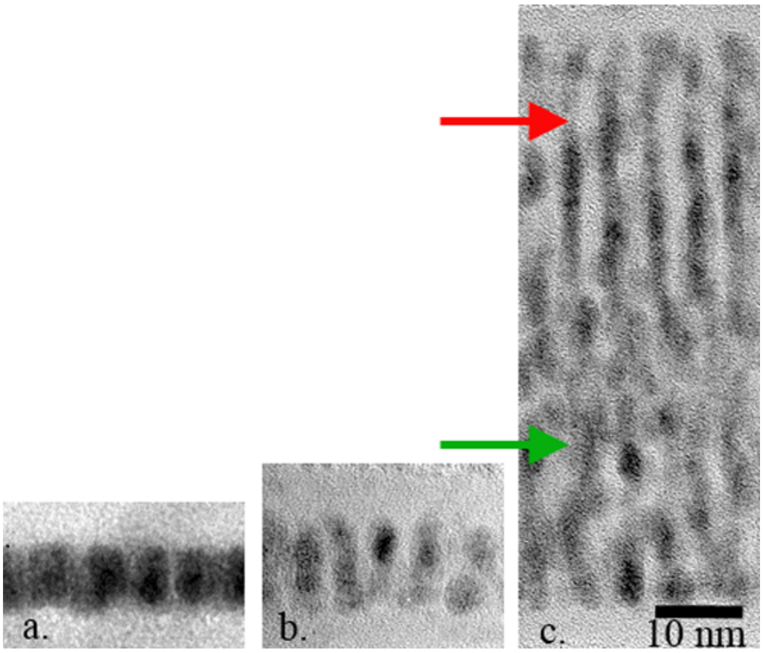

Figure 3.9: Cross-section TEM images of films produced with N=5, 10 and 50 (a., b., and c., respectively) with X= D. The red arrow shows discontinuites while the green one shows misalignement of NCls

The thickness X of the matrix layer has to have a critical value $D \leq X_T \leq 2D$ within which the self-organization process starts. If the NPs are not covered, the next metal atoms nucleate on almost all the surface of the NPs and leads to coalesced NPs. Instead, if they are totally covered, there is no preferential nucleation sites, and well separated layer of NPs will be produced. It is thus essential to keep a small part of NPs uncovered.

As X decreases below this value, the size of the uncovered areas in the matrix template and the amount of metal exposed to next metal arrival increases thus promoting NCls with larger diameter and consequently shorter height.

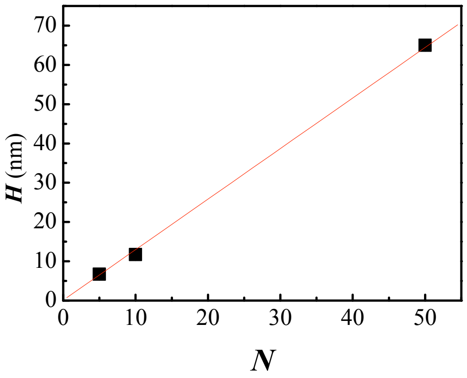

Figure 3.10: Average heigth H as function of the number of cycles N. The red line is a linear fit.

In principle, the maximum height of the NCls achievable by this method is defined by the number of cycles N and thus, only limited by the stability of the production system. We have explored this limit by increasing the number of cycles in order to increase the aspect ratio of the NCls. We have maintained constant the conditions previously defined to produce the NCls, in order to achieve the same average diameter $D \approx$ 2.7 nm while increasing N. Figure 3.9 shows cross-section TEM images of samples produced with $X=D$ and increasing number of cycles N (5, 10, and 50). H clearly increases with N and the aspect ratio was varied from 2.5 ($N = 5$) to 25 ($N = 50$). The height H of these NCls is plotted in Fig. 3.10 as a function of N. As it was expected H increases linearly with N. Nevertheless, Fig. 3.9 c. shows that there are some defects in the NCls for $N = 50$. Two types of defects can be observed in this figure. The first one are discontinuities in the NCls (Fig. 3.9 c. red), as if some of the NPs did not nucleate correctly or in the good position. The other defect is the misalignment of some of the NCls (Fig. 3.9 c. green), i.e some of the NCls close to each other are linked. This defects are most likely related to slight variations in the ablation parameters and the NP nucleation conditions during growth.

3.5 Conclusion

In this chapter we have presented the results obtained with our approach to "nano-design" structures based on the alternate-PLD technique described in Chapter 2. The protocols we have implemented allow achieving a precise control on the size, shape and spatial organization of metallic nanostructures embedded in an oxide matrix. In the first part we have demonstrated how to control the equivalent thickness of a-Al_2O_3, X, in order to produce Co-Ag bilayers, having in-depth separations from 8 to 4 nm.

This excellent in-depth control allowed us to decrease X until NPs of consecutive layers got in contact and led to Ag NCls. The number density, diameter and height of NCls can potentially be controlled by varying the amount of metal deposited in the first cycle (deposition time), the amount of metal deposited in subsequent cycles and the number of cycles, respectively. These results open new possibilities for material nano-engineering since they provide a simple route based on a single step process at room temperature to produce oriented metal nanocolumns with diameters typically $\leq$4 nm and with low dimension and shape dispersion. These features are not easily accessible with other techniques.

In Chapters 7 and 8 we present the results related to the optical and vibrational properties of the nanostructures produced and shown in this Chapter. However, in order to fully understand these results, Chapters 4 and 5 introduce the basic theory needed to understand and interpret these results.

Part III

Optical and vibrational properties of metallic nanoparticles

4

Introduction to the optical and vibrational properties of bulk metals

In this chapter we describe the optical and vibrational properties of bulk metals, and particularly that of noble metals, that will be used for the analysis of the experimental results in Part IV. All the equations are given in the international system of units.

4.1 Optical properties

The optical properties of metals are determined by the response of the conduction band electrons to an applied electromagnetic field. The first approach is to consider that these electrons are free. This ideal situation is described by the Drude model. We will also use this classical approach to introduce the notion of dielectric function, which characterizes of the optical properties of a solid. We will finally show that the core electrons affect the optical properties in the case of noble metals.

4.1.1 Dielectric function and electric susceptibility

The electric field $\boldsymbol{E}$, and the electric displacement $\boldsymbol{D}$ in a material, are related by the following expression:

$$\boldsymbol{D} = \epsilon_0 \boldsymbol{E} + \boldsymbol{P}, \tag{4.1}$$

where ϵ_0 is the vacuum permitivity and $\boldsymbol{P}$ the polarization induced by the electric field $\boldsymbol{E}$. In a linear, homogenous and infinite medium, the polarization $\boldsymbol{P}$ is linearly related to $\boldsymbol{E}$ through the electric susceptibility, $\tilde{\chi}$, of the medium:

$$\boldsymbol{P} = \epsilon_0 \tilde{\chi} \boldsymbol{E} \tag{4.2}$$

which allows to establish a relationship between $\boldsymbol{D}$ and $\boldsymbol{E}$ through the complex dielectric function, $\tilde{\epsilon}$:

$$\boldsymbol{D} = \epsilon_0 \tilde{\epsilon} \boldsymbol{E} \quad \text{with} \quad \tilde{\epsilon} = 1 + \tilde{\chi}. \tag{4.3}$$

We must note that for an anisotropic medium, $\tilde{\chi}$ is a tensor. Consequently $\tilde{\epsilon}$ is similarly a tensor, which is generally written under a complex form given by:

$$\tilde{\epsilon} = \epsilon_1 + i\epsilon_2. \tag{4.4}$$

4.1.2 Absorption coefficient

When a metal is placed in an electromagnetic field, a polarization is induced inside the metal. This optical response can be described by the dielectric constant $\tilde{\epsilon}(\omega)$. Let us assume that the metal is placed in vacuum. Then, the electric wave equation is given by (Helmholtz):?

$$\nabla^2 \boldsymbol{E} + \frac{\omega^2}{c^2} \tilde{\epsilon}(\omega) \boldsymbol{E} = 0, \tag{4.5}$$

where c is the light velocity in vacuum. The solutions of this equation are of the type of a plane monochromatic wave, $\boldsymbol{E} = \boldsymbol{E}_0 \exp[i(\boldsymbol{k}z - \omega t)]$ which leads to a particular solution of the form:

$$\boldsymbol{E} = \boldsymbol{E}_0 \exp\left[i\omega\left(\frac{\tilde{n}}{c}z - t\right)\right]. \tag{4.6}$$

$\tilde{n}$ is the complex refractive index of the metal, defined by:

$$\tilde{n} = n + i\kappa = \sqrt{\tilde{\epsilon}}. \tag{4.7}$$

where n is the refractive index and κ the extinction coefficient of the metal. When the wave propagates in an absorbing material, damping (energy loss) occurs leading to a decrease of intensity. In the case of a plane wave the intensity is related to the amplitude of the electric field by:

$$I = \frac{n}{2}\ c\ \epsilon_0 \langle E^2 \rangle \tag{4.8}$$

We can therefore conclude from Eq. 4.6 that the intensity falls off exponentially in the medium as:

$$\exp(-\frac{2\omega\kappa}{c}z). \tag{4.9}$$

On comparing this to the Lambert-Beer's law ($I(z) = I_0 exp(-\alpha z)$) we can define the absorption coefficient of the material as:

$$\alpha_{abs}(\omega) = 2\frac{\omega}{c}\kappa(\omega). \tag{4.10}$$

4.1.3 The Drude model

The dielectric function of an electron gas can be obtained from the equation of motion of a free electron immersed in an electrtic field $\boldsymbol{E}$. For a free electron, of mass m_e and charge $-e$ this equation is given by:

$$\frac{\mathrm{d}^2\boldsymbol{u}}{\mathrm{d}t^2} = -\frac{e}{m_e}\boldsymbol{E}, \tag{4.11}$$

where $\boldsymbol{u}$ stands for the vector displacement of the electron. However, when the electron is moving inside a material, the forces due to the presence of the atoms affect its motion. The concept of effective mass, m_{eff}, is introduced to take this into account.**?**

In order to describe the situation of the electron in a material, with the corresponding interactions (electron-phonon, electron-electron,...), the Drude model introduces a damping factor γ_0, which is inversely proportional to the mean free path l of the electron in the metal and is given by:

$$\gamma_0 = \frac{v_F}{l}, \tag{4.12}$$

where v_F is the Fermi velocity. This damping factor is introduced in the equation of motion as an additional term in the form:

$$\frac{\mathrm{d}^2\boldsymbol{u}}{\mathrm{d}t^2} + \gamma_0\frac{\mathrm{d}\boldsymbol{u}}{\mathrm{d}t} = -\frac{e}{m_{eff}}\boldsymbol{E}. \tag{4.13}$$

In the case of a monochromatic planar light wave of frequency ω, we can express the electric field as:?

$$\boldsymbol{E} = \boldsymbol{E}_0(\boldsymbol{r})exp(-i\omega t). \tag{4.14}$$

Equation 4.13 allows a solution of the type $\boldsymbol{u} = \boldsymbol{u}_0 exp(-i\omega t)$, leading to:

$$-m_{eff}\omega^2\boldsymbol{u}_0 - i(m_{eff}\gamma_0\omega\boldsymbol{u}_0) = -e\boldsymbol{E}_0 \quad \text{with} \quad \boldsymbol{u}_0 = \frac{e}{m_{eff}\omega(\omega + i\gamma_0)}\boldsymbol{E}_0 \tag{4.15}$$

The displacement of the electrons from their equilibrium position produces a time varying dipole moment $(e.\boldsymbol{u})$. If N is the number of free electrons per volume unit, then:

$$\boldsymbol{P} = Ne\boldsymbol{u} = \boldsymbol{P}_0 exp(-i\omega t) \quad \text{with} \quad \boldsymbol{P}_0 = (1 - \tilde{\epsilon}(\omega))\epsilon_0\boldsymbol{E}_0 \tag{4.16}$$

From Eqs. 4.15 and 4.16 we can deduce the Drude expression for the dielectric function:

$$\tilde{\epsilon}^{Drude}(\omega) = 1 - \frac{\omega_p^2}{\omega(\omega + i\gamma_0)}, \tag{4.17}$$

where

$$\omega_p = \sqrt{\frac{Ne^2}{m_{eff}\epsilon_0}} \tag{4.18}$$

is the plasma frequency. For optical frequencies ($\omega >> \gamma_0$), the real and imaginary parts of the dielectric function are:?

$$\epsilon_1^{Drude}(\omega) \approx 1 - \frac{\omega_p^2}{\omega^2} \quad \text{and} \quad \epsilon_2^{Drude}(\omega) \approx \frac{\omega_p^2}{\omega^3}\gamma_0. \tag{4.19}$$

4.1.4 Noble metals

The traditional definition of noble metals is that they are resistant to corrosion or oxidation, for example Au, Ag, Ta, Pt, Pd and Rh. However, a more precise physical definition of a noble metal is that the d-bands of the electronic structure are completely filled. Taking this into account, only Cu, Ag and Au are "true" noble metals.

For these metals, the Drude approximation, which involves only the response of free electrons, is not valid, since, in most cases, the core electrons influence the response of the metal when excited by an electromagnetic wave.

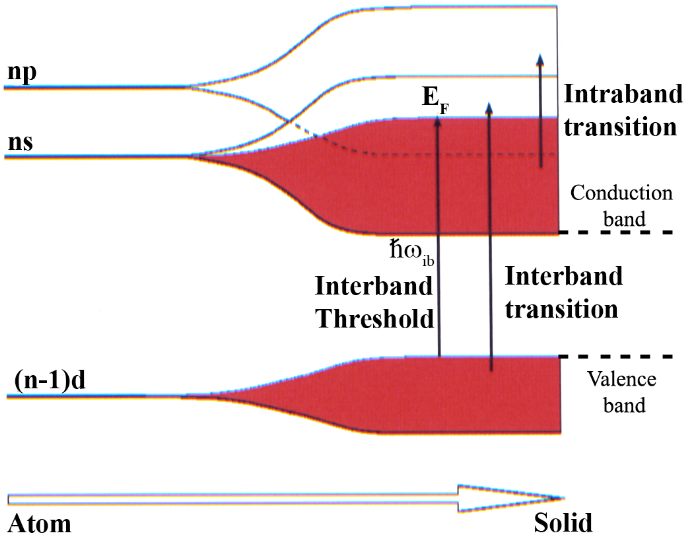

Figure 4.1: Schematic of the evolution of the electronic structure characteristic of the noble metals, from atomic energy level to bulk energy bands. Interband and intraband transitions can correspond to photons energies in the visible or UV region of the spectra. $\hbar\omega_{ib}$ is the threshold energy for interband transitions.?

Figure 4.1? schematizes for noble metals the evolution of the band structure from the energy levels charcteristic of an atom to the bulk energy bands. The fact that the "s" and "p" bands overlap in bulk metals lead to the hybridization of the conduction band. The transitions involving levels within the conduction band are called intraband transitions (Fig. 4.1), and the intraband contribution to the dielectric constant is given by the Drude model (Eq. 4.17):

$$\tilde{\epsilon}^{Intra} = \tilde{\epsilon}^{D} = 1 - \frac{\omega_p^2}{\omega(\omega + i\gamma_0)}. \tag{4.20}$$

Noble metals are charcterized by the presence of a filled "d" band (valence) very close to the conduction band. Transitions from the core levels of the "d" band to the levels of the conduction band located above the Fermi level are thus possible. These transitions are called interband transitions, and are allowed when the energy of the photon is larger than a threshold value $\hbar\omega_{ib}$ (interband threshold). In the particular case of the noble metals this threshold lies in the visible (Au and Cu) or near UV (Ag) range.

Figure 4.2 compares the real and imaginary parts of the experimental? ($\tilde{\epsilon}(\omega)$) and calculated ($\tilde{\epsilon}^{Intra}(\omega)$) dielectric functions.

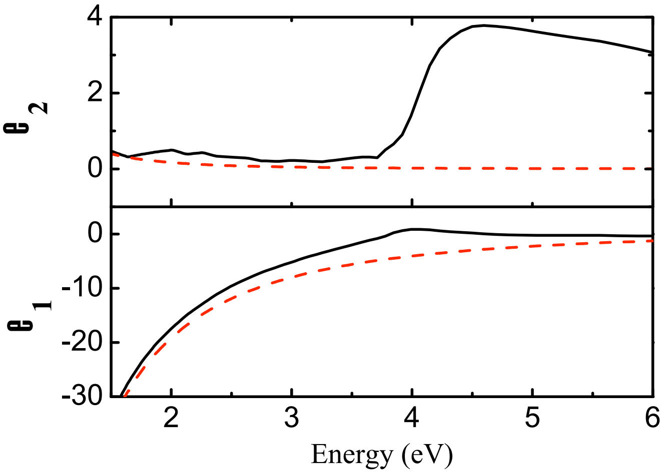

Figure 4.2: Real, ϵ_1, and imaginary ϵ_2, parts (black) of the experimental dielectric function of bulk Ag, $\tilde{\epsilon}(\omega)$, and (red) calculated intraband contribution to the dielectric function $\tilde{\epsilon}^{Intra}(\omega)$.

There is a clear difference between the experimental and calculated values, particularly for energies higher than 3.9 eV. Moreover, a strong increase of the experimental value of ϵ_2 is observed around 3.9 eV, which marks the beginning of the interband transitions $\hbar\omega_{ib}$. For photons with energy lower than $\hbar\omega_{ib}$, only the electrons of the conduction band can be excited (intraband transitions), while for higher energies, the electrons of the "d" band can be excited to levels above the Fermi level and thus contribute to the dielectric function of the metal.

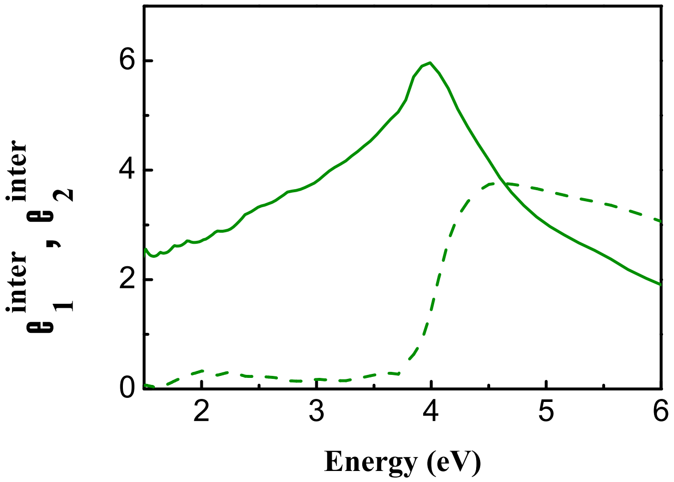

Figure 4.3: (continuous line) Real, ϵ_1^{inter}, and (dash line) imaginary, ϵ_2^{inter}, parts of the interband contribution to the dielectric function, $\tilde{\epsilon}^{inter}$, of Ag deduced from Eq. 4.21.

Hence it is necessary to add a new term to account for that contribution, which leads to:?

$$\tilde{\epsilon}(\omega) = \tilde{\epsilon}^{intra}(\omega) + \tilde{\epsilon}^{inter}(\omega), \tag{4.21}$$

Interband transitions are characterized by a broad light absorption, which leads to an increase of the imaginary part of $\tilde{\epsilon}^{inter}(\omega)$ above the interband threshold. Such increase is visible in Fig. 4.3 where the real and imaginary parts of $\tilde{\epsilon}^{inter}$ are plotted in the case of Ag. The spectra have been deduced from Eqs. 4.21 using the experimental value of the dielectric function? and the parameters presented in Table 4.1 for Ag.

We observe a sharp increase of ϵ_2^{inter} above the interband threshold and the appearance of one peak in the spectrum of ϵ_1^{inter} around 3.9 eV. These behaviors are responsible for the color of noble metals; yellow, red-orange, and gray, for bulk Au, Cu, and Ag respectively. Table 4.1? summarizes the essential electronic properties of Cu, Ag and Au.

Metal	Electronic structure	ϵ_F (eV)	m_{eff}/m_e	$\hbar\omega_p$ (eV)	$\hbar\omega^{Inter}$ (eV)
Cu	$[Ar]3d^{10}4s^1$	4.67	1.5	8.82	2.1
Ag	$[Kr]4d^{10}5s^1$	5.49	1	8.98	3.9
Au	$[Xe]4f^{14}5d^{10}6s^1$	5.53	1	9.01	2.4

Table 4.1: Electronic properties of noble metals: electronic configuration, energy of the Fermi level, relative effective mass, plasma energy, threshold energy of the interband transitions.

4.2 Vibrational properties

In this section we recall some general notions of inelastic light scattering by a crystal and we especially describe the Raman process. However, a detailed description is out of the scope of the present work and can be found elsewhere.[?, ?]

4.2.1 Vibrations of a crystal

At room temperature each atom of the crystal is moving. The motion of each atom is coupled with its neighbors. Due to these atomic displacements and to the translation symmetry of the crystal, delocalized vibrations appear in the whole crystal. The energy of the vibrations is quantized: these "phonons" can be defined as a vibrational quantum of energy[?] by analogy with photons and electromagnetic waves. A phonon is also characterized by a frequency Ω and a wave vector $\mathbf{Q}$. This is illustrated in Fig. 4.4 where the dispersion curves of phonons in Ag measured at room temperature are shown.[?]

In the case of Ag there is only one atom in the primitive cell, thus only acoustic branches are observed in the phonon dispersion curves. In Fig. 4.4, T_1 and T_2 label the branches associated to transverses waves (the direction of propagation is perpendicular to the motion of the atoms), while the L branches are related to longitudinal waves (the direction of propagation is parallel to the motion of the atoms). For each branch, the number of eigenmodes of vibration is equal to the number of atoms N_c in the crystal. In the case of bulk crystals, N_c is very large and the vibrational energy levels form a quasi-continuum of energy. The energy of a vibration mode is $\hbar\Omega$ and the number of excitations occupying this mode is given by $n(\Omega)$ that, at thermal equilibrium and

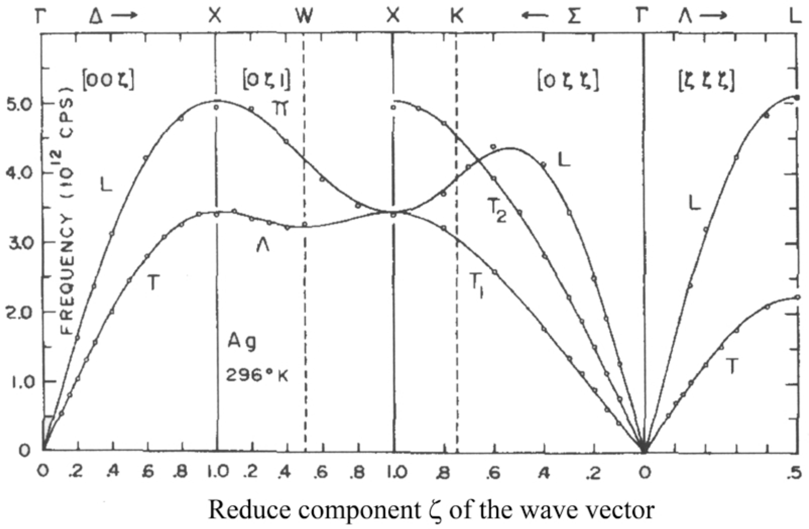

Figure 4.4: Phonon dispersion curve of Ag determined at room temperature using inelastic scattering of neutrons.[?]

temperature T, is given by the Bose-Einstein distribution:

$$n(\Omega) = \frac{1}{\exp\left(\frac{\hbar\omega}{k_B T}\right) - 1}, \tag{4.22}$$

where k_B is the Boltzmann constant.

4.2.2 Mechanism for light scattering

Inelastic light scattering describes the phenomenon by which a light beam is scattered by a medium and changes its frequency and wavevector during the process.

The detection of the scattered light offers valuable information on the structure of the scattering medium. We provide a basic description of the light scattering by a crystal, although the problem of the interaction of an electromagnetic wave with a crystal will not be described in detail.

Origin of the scattering

The response of the charges to the optical excitation is defined by the electric susceptibility tensor $\tilde{\chi}$. The motion of the atoms induces small variations of the electric susceptibility tensor that is expressed as a function of time and position ($\tilde{\chi}(\mathbf{r},t)$). The tensor $\tilde{\chi}(\mathbf{r},t)$ can be thus written under the form:

$$\tilde{\chi}(\mathbf{r},t) = \tilde{\chi}_0 + \delta\tilde{\chi}(\mathbf{r},t), \tag{4.23}$$

where $\tilde{\chi}_0$ is a constant and $\delta\tilde{\chi}(\mathbf{r},t)$ denotes the fluctuations of the electric susceptibility. Eq. 4.2 can be then rewritten as:

$$\mathbf{P}(\mathbf{r},t) = \epsilon_0 \left[\tilde{\chi}_0 + \delta\tilde{\chi}(\mathbf{r},t)\right] \mathbf{E}(\mathbf{r},t). \tag{4.24}$$

For an incident electromagnetic plane wave of wave vector $\mathbf{k}_0$ and circular frequency ω_0, the polarization is thus given by:

$$\mathbf{P}(\mathbf{r},t) = \epsilon_0 \mathbf{E}_0 \left[\tilde{\chi}_0 + \delta\tilde{\chi}(\mathbf{r},t)\right] \exp\left[i(\mathbf{k}_0.\mathbf{r} - \omega_0 t)\right]. \tag{4.25}$$

The electric field, scattered by the crystal, generated at a point $\mathbf{r}$ and at an instant t by the oscillation of the polarization can be written as:[?,?]

$$\mathbf{E}^{sca}(\mathbf{r},t) = \frac{1}{4\pi\epsilon_0 c^2} \int \frac{1}{\|\mathbf{r}-\mathbf{r}'\|} \left(\frac{\partial^2 \mathbf{P}(\mathbf{r}',t')}{\partial t'^2} \times \mathbf{e_u} \right) \times \mathbf{e_u} d^3\mathbf{r}', \tag{4.26}$$

where $t' = t - \|\mathbf{r}-\mathbf{r}'\|/c_n$ is the delayed time, c_n is the light velocity of a medium of index n and $\boldsymbol{e_u}$ is a unitary vector in direction $\mathbf{r}-\mathbf{r}'$. When the electric field oscillates quickly compared to the fluctuations of the susceptibility we have

$$\frac{\partial^2 \mathbf{P}}{\partial t'^2} \approx -\omega_0^2 \mathbf{P}, \tag{4.27}$$

and,

$$\mathbf{k}_0.\mathbf{r}' - \omega_0 t' = (\mathbf{k}_0 - \mathbf{k}_s).\mathbf{r}' + \mathbf{k}_s.\mathbf{r} - \omega_0 \tag{4.28}$$

where $\mathbf{k}_s$ is the wave vector of the scattered light.

We can finally deduce the electric field $\mathbf{E}(\mathbf{r}, t)$:

$$\mathbf{E}^{sca}(\mathbf{r}, t) \propto \omega_0^2 \exp\left[i(\mathbf{k}_s.\mathbf{r} - \omega_0 t)\right](\mathbf{E} \times \mathbf{e_u}) \times \mathbf{e_u} \int [\tilde{\chi}_0 + \delta\tilde{\chi}(\mathbf{r}', t')] \exp\left[i(\mathbf{k}_0 - \mathbf{k}_s).\mathbf{r}'\right] d^3\mathbf{r}'. \tag{4.29}$$

This expression is the sum of two terms. The term containing $\tilde{\chi}_0$, refers to the incident wave of frequency ω_0, which propagates along $\mathbf{k}_0$, while the other containing $\delta\tilde{\chi}$ shows that the scattered field is indeed due to fluctuations of the electric susceptibility $\delta\tilde{\chi}$. From this second term it is thus possible to differentiate two types of light scattering:[?,?,?,?]

- Static fluctuations, i.e. $\delta\tilde{\chi}(\mathbf{r}, t) \sim \delta\tilde{\chi}(\mathbf{r})$. The radiation is scattered with the same frequency as the incident light one. This process is known as Rayleigh scattering. The light is elastically scattered along all directions $\mathbf{k}_s$.
- If the fluctuations of the susceptibility are caused by a periodic modulation of the atomic bonds in the crystal, typically by vibrational waves, the light scattering is inelastic. This scattering is known as Raman scattering.[?]

Thus, Raman scattering relates to vibration modes of the crystal under light excitation. The vibrational wave modifies the optical properties of the crystal, modifying its refractive index, and thus can interact with the incident electromagnetic wave. Reciprocally, the incident electromagnetic wave generates a periodic mechanic deformation, i.e. a vibrational wave, and thus, modifies the elastic properties of the medium. In the following we describe in more detail the Raman scattering process.

4.2.3 Raman scattering process

A vibration mode j propagating with a wave vector $\mathbf{Q}_j$ and a frequency Ω_j generates fluctuations of the susceptibility that can be written as follows:[?]

$$\delta\tilde{\chi}_j(\mathbf{r}', t') = \delta\tilde{\chi}_j(\mathbf{Q}_j) \exp\left[i(\mathbf{Q}_j.\mathbf{r}' - \Omega_j(\mathbf{Q}_j)t')\right]. \tag{4.30}$$

The electric field associated to the scattered wave induced by these fluctuations is given by:

$$\mathbf{E}_j^{sca}(\mathbf{r},t) \propto (\omega_0\Omega_j)^2 exp\{i[\mathbf{k}_{sca}.\mathbf{r} - (\omega_0 \pm \Omega_j(\mathbf{Q}_j))t]\}(\mathbf{E}_0 \times \mathbf{u}) \times \mathbf{u}\delta\chi(\mathbf{Q}_j) \tag{4.31}$$

$$\times \int exp[i(\mathbf{k}_0 - \mathbf{k}_s\mathbf{Q}_j).\mathbf{r}']d^3\mathbf{r}'. \tag{4.32}$$

In this process, the scattered wave has not the same energy as the excitation wave. There is an inelastic scattering of a photon with creation or annihilation of a phonon. Indeed, if $\mathbf{k}_{sca}$ and ω_{sca} are the wave vector and frequency of the scattered photon, respectively, the laws of wave vector and energy conservation provide the following relations:

- Conservation of the wave vector:

$$\mathbf{k}_{inc} = \mathbf{k}_{sca} \pm \mathbf{Q}, \tag{4.33}$$

- Conservation of energy:

$$\hbar\omega_{inc} = \hbar\omega_{sca} \pm \hbar\Omega, \tag{4.34}$$

where $\mathbf{Q}$ and Ω are the wave vector and frequency of the phonon, respectively. When the energy of the scattered photon is smaller than the energy of the incident photon, the scattering process is know as Stokes scattering. The creation of a phonon $(\mathbf{Q},\Omega)$ is accompanied by a scattered photon of frequency $\omega_{sca} = \omega_{inc} - \Omega$. The crystal gains an energy $\hbar\Omega$ and is excited from the vibrational level n to the level $n+1$. A process in which a phonon is annihilated is called anti-Stokes. The crystal, passing from a vibrational level n to $n-1$, losses energy $\hbar\Omega$. Therefore the scattered photon has an energy higher than the incident photon. This is illustrated in Figure 4.5 which shows Stokes (Fig. 4.5(a)) and anti-Stokes (Fig. 4.5(b)) diagrams of the Raman scattering.

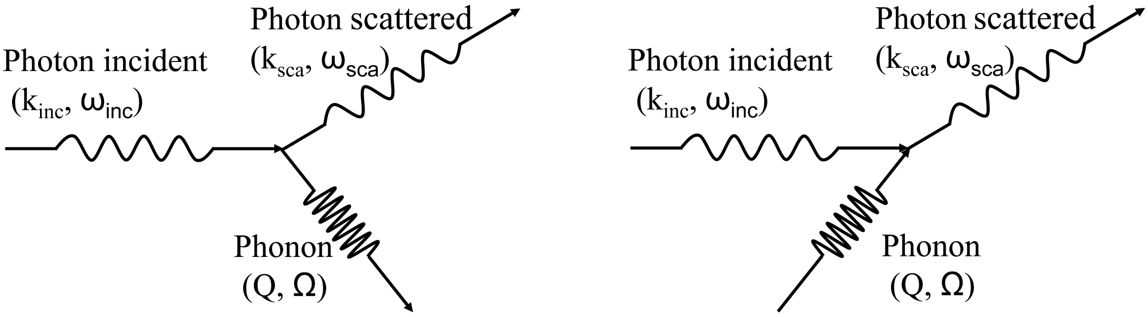

(a) Creation of a phonon (Stokes)

(b) Annihilation of a phonon (anti-Stokes)

Figure 4.5: Diagrams representing the inelastic scattering process of a photon $(\mathbf{k}_{inc}, \omega_{inc})$ with (a) creation or (b) annihilation of a phonon $(\mathbf{Q}, \Omega)$. The scattered photon is characterized by $(\mathbf{k}_{sca}, \omega_{sca})$.

5

Optical and vibrational properties of metal nanoparticles

The optical and vibrational properties of bulk metals have been presented in Chapter 4. In this chapter we will describe the effect of reducing the characteristic dimensions of metals down to the nanometer scale and structuring the NPs (organization, size and shape).

5.1 The dielectric constant

In the case of a finite system, such as a metal NP with characteristic dimensions of few nanometers, two size related effects that have a strong influence on the optical properties of the NPs appear. The energy levels of the conduction band are discrete and second, there are collisions of the electrons of the conduction band with the NP surface. Both processes have a clear impact on the electronic susceptibility and thus on the dielectric function.[?,?]

We have seen in Chapter 4 that the dielectric constant can be expressed as the sum of the intraband and interband contributions. When we reduce the size of the system, the interband contribution is almost independent of the size for diameters > 1 nm,[?,?] while the intraband contribution is size-dependent. In finite systems the Drude model is no longer valid to calculate the intraband contribution, $\tilde{\epsilon}^{intra}$, but it is still possible to obtain a similar expression to Eq. 4.17 where the size dependence of the dielectric constant is taken into account by introducing an additional term to the damping constant (γ_0) that depends on the NP diameter, D, and frequency, ω. The intraband contribution is then given by:

$$\tilde{\epsilon}^{Intra}(\omega) = 1 - \frac{\omega_p^2}{\omega^2 + i\omega\gamma(\omega, D)} \tag{5.1}$$

with

$$\gamma(\omega, D) = \gamma_0 + g_s(\omega)\frac{2v_F}{D}, \tag{5.2}$$

where v_F is the Fermi velocity and $g_s(\omega) \approx 1$ is a coefficient slowly varying with ω.[?] γ_0 is the bulk damping due to collisions (electron-phonon, electron-electron, and electron-defects), while the term $2g_s(\omega)v_f/D$ accounts for the damping due to the size reduction (collision with the surface). This damping is important when the diameter of the particle, D, becomes comparable or smaller than the mean free path of the electrons. Thus the dielectric constant of a spherical NP with diameter D can be deduced from Eq. 5.1 and Eq. 4.21 using the data available for bulk materials ($\tilde{\epsilon}_{exp}(\omega)$):[?]

$$\tilde{\epsilon}(\omega, D) = \tilde{\epsilon}_{exp}(\omega) + \frac{\omega_p^2}{\omega^2 + i\omega\gamma_0} - \frac{\omega_p^2}{\omega^2 + i\omega\gamma(\omega, D)}. \tag{5.3}$$

Figure 5.1 shows the behavior of the real and imaginary part of the dielectric constant in the case of bulk Ag[?] and Ag NPs with diameter of 20 and 4 nm. As the diameter of the NP decreases, the values of the real and imaginary parts of the dielectric function increase. This is clearly visible for wavelengths above the interband transition threshold 3.9 eV (≈320 nm). The figure also shows the importance of the size dispersion since a small variation of the diameter induces a large change of the dielectric function. These changes will affect the optical properties of the NP, and thus the optical properties of

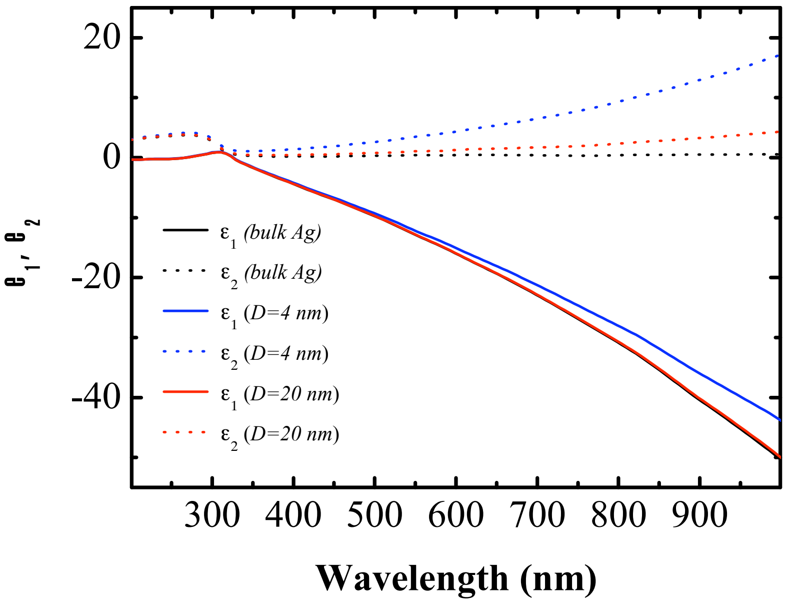

Figure 5.1: Real (ϵ_1) and imaginary (ϵ_2) parts of the dielectric function of bulk silver and Ag NPs having diameters of 20 nm and 4 nm.

the nanocomposites. The next section introduces the optical properties of metal NPs. From now on, $\tilde{\epsilon}(\omega)$ will refer to the size dependent dielectric function of the NP.

5.2 Optical properties of embedded metal nanoparticles

In addition to the modification of the dielectric function, the reduced size of the metal NPs introduces spatial limits that impose new boundary conditions to the electromagnetic field and thus, new electromagnetic states, known as plasmons, appear.

5.2.1 Plasmons, plasmon-polaritons, volume plasmons, surface plasmons:

Before describing the optical properties of metal NPs we aim in this section to clarify the nomenclature used in this work. Plasmons are collective oscillations of the free electron gas. When these plasmons interact strongly with light, this results in a mixing of collective electronic oscillations with light known as plasmon-polaritons. Moreover, there are two types of plasmons. If a NP is excited by an electron beam, charges are generated inside the volume of the NP which induces fluctuations of the electron density inside the NP (volume plasmon). On the contrary, if the NP is excited with light, polarization charge oscillations, namely the surface plasmon oscillations, are generated at the surface. The surface plasmons are surface plasmon-polaritons in the sense that they are coupled to the incident light.

In this work, we will deal with surface plasmons (SPs) of Ag NPs. In the following we describe their origin using different models. We start first with the simplest case of an isolated spheroidal NP in vacuum, and we consecutively introduce new parameters, such as the matrix, the size, the shape, and the number density of NPs, by considering more elaborated models.

5.2.2 Isolated spherical particle

Quasi static approximation

We consider in Fig.5.2 an isolated spherical NP of diameter D characterized by the size dependent dielectric function, $\tilde{\epsilon}(\omega, D)$, introduced above, and embedded in a dielectric matrix with a real dielectric function, ϵ_m. This NP is immersed in the electric field $\boldsymbol{E}$ of a plane electromagnetic wave of frequency ω, and wavelength $\lambda >> D$. In this case we can consider that an instant t, the electromagnetic field is uniform. Thus, we can consider the quasi static approximation (only the term dipolar electric is considered in the determination of the optical response). Under these conditions, the electric field inside the sphere is given by the Clausius-Mossotti formula extended to the mesoscopic scale:[?]

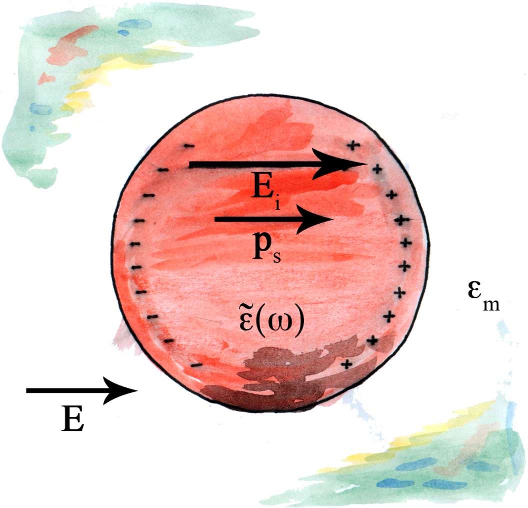

Figure 5.2: Interaction of a spherical particle of diameter D with an electromagnetic wave in the quasi-static approximation.

$$\mathbf{E}_i = \frac{3\epsilon_m}{\epsilon(\omega) + 2\epsilon_m}\mathbf{E} \tag{5.4}$$

In the medium surrounding the NP, the electromagnetic field is the sum of the applied field and the field generated by a dipole located at the center of the NP. The dipolar moment is given by

$$\mathbf{p} = 3V\epsilon_0\epsilon_m\frac{\tilde{\epsilon} - \epsilon_m}{\tilde{\epsilon} + 2\epsilon_m}\mathbf{E} \tag{5.5}$$

where V is the volume of the NP. The polarizability $\tilde{\alpha}(\omega)$ of a dipole immersed in a dielectric medium of dielectric function ϵ_m in the presence of a field $\mathbf{E}$ of frequency ω is defined by the relation:

$$\mathbf{p} = \epsilon_0\epsilon_m\tilde{\alpha}(\omega)\mathbf{E} \tag{5.6}$$

Then, from Eqs. 5.5 and 5.6, the polarizability can be written as:

$$\tilde{\alpha}(\omega) = 3V\frac{\tilde{\epsilon} - \epsilon_m}{\tilde{\epsilon} + 2\epsilon_m} \tag{5.7}$$

The absorption cross section is related to the polarizability by:?

$$\sigma_{abs} = \frac{\omega\sqrt{\epsilon_m}}{c} Im[\tilde{\alpha}(\omega)], \tag{5.8}$$

where Im$[\tilde{\alpha}(\omega)]$ is the imaginary part of the NP polarizability, c is the light velocity in vacuum. Thus, from Eqs. 5.7 and 5.8 we can deduce the expression of the absorption cross section:

$$\sigma_{abs} = \frac{9V\omega\epsilon_m^{3/2}}{c}\frac{\epsilon_2}{(\epsilon_1 + 2\epsilon_m)^2 + \epsilon_2^2}. \tag{5.9}$$

σ_{abs} varies with the frequency ω, and shows a resonant behavior when:

$$\left(\epsilon_1(\omega) + 2\epsilon_m\right)^2 + \epsilon_2^2(\omega) \quad \text{is minimum.} \tag{5.10}$$

Thus the resonance condition is:

$$\epsilon_1(\omega_{SPR}) = -2\epsilon_m^{\omega_{SPR}} \tag{5.11}$$

where ω_{SPR} is the frequency of the SP resonance. At ω_{SPR}, the electric field inside the particle (Eq. 5.4), is also strongly enhanced. Considering that $\epsilon_1 \approx \epsilon_1^{inter} - \omega_p^2/\omega^2$ (Eq. 4.18), the frequency of the surface plasmon resonance is given by:

$$\omega_{SPR} = \frac{\omega_p}{\sqrt{\epsilon_1^{inter}(\omega_{SPR}) + 2\epsilon_m}} \tag{5.12}$$

From the previous equation we see that, in the quasistatic approximation and for a given metal, the SPR wavelength only depends on the dielectric function of the surrounding medium. Figure 5.3 shows extinction cross section of a silver NP of diameter 4 nm, embedded in different matrices, calculated using Eq. 5.9 and using the dielectric constant of the Ag NP obtained from equation 5.3 considering $g_s = 1$.

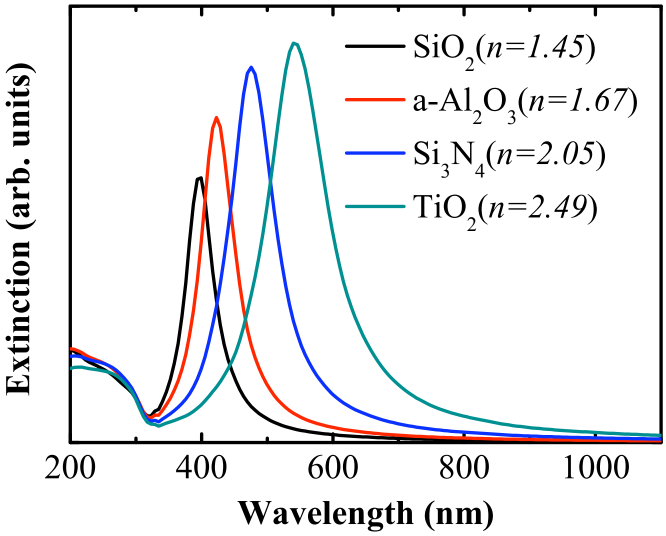

Figure 5.3: Calculated extinction spectra of Ag NP of a 4 nm diameter embedded in different matrices

It can be seen in Fig.5.3 that $\hbar\omega_{SPR}$ is always well separated from the interband absorption edge. It also shows that the SPR wavelength shifts to the red when increasing the refractive index of the matrix. In the present work, the matrix used is a-Al_2O_3 ($n = 1.67$).

The quasi-static approximation is valid in the case of small NPs. However, as the diameter of the NP increases multipolar terms must be taken into account. Gustav Mie? developed in 1908 a theory for the interaction of an electromagnetic wave with a metallic particle based on the multipolar development of the electromagnetic field.

Mie theory

In this case, the NP is placed in an electromagnetic field varying in time and space, i.e. at an instant t, the electromagnetic field is no longer uniform. Fig. 5.4 presents a scheme of the problem considered. The NP is placed into an electromagnetic field

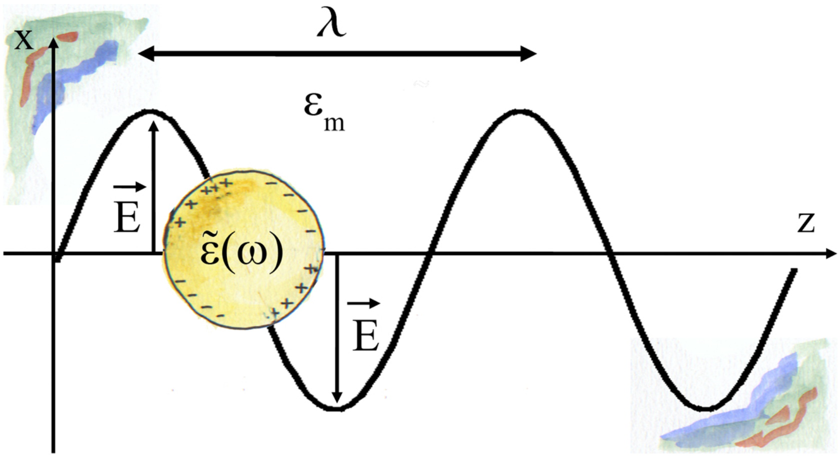

Figure 5.4: Surface polarization charges distribution inside "a large particle" which gives rise to a quadrupolar contribution to the SPR.

polarized along the x-axis. Mie theory[?] describes the wave scattered by this metallic particle as a linear superposition of diverging spherical waves, each wave being radiated by an electric or magnetic multi-pole with amplitude a_l and b_l, where l is the order of the multipole, respectively given by:[?, ?, ?]

$$a_l = \frac{n\psi_l(nx)\psi_l'(n_m x) - n_m\psi_l'(nx)\psi_l(n_m x)}{n\psi_l(nx)\eta_l'(n_m x) - n\psi_l'(nx)\eta_l(n_m x)} \tag{5.13}$$

$$b_l = \frac{n_m\psi_l(nx)\psi_l'(n_m x) - n\psi_l'(nx)\psi_l(n_m x)}{n_m\psi_l(nx)\eta_l'(n_m x) - n\psi_l'(nx)\eta_l(n_m x)} \tag{5.14}$$

with $n = \tilde{n} = \sqrt{\tilde{\epsilon}}$ and $n_m = \sqrt{\epsilon_m}$. $\psi_l(z) = \sqrt{\pi z/2}J_{l+1/2}(z)$ is a Bessel-Riccati function (($J_{l+1/2}$) is a Bessel function (semi-integer)), and $\eta_l(z) = \sqrt{\pi z/2}H^{(1)}_{l+1/2}(z)$ ($H^{(1)}_{l+1/2}$ is a Hankel function semi-integer of the first kind). In these expressions, $x = k_0 R$ where k_0 is the wave vector of the incident wave in vaccum and R the radius of the sphere. The scattering cross section of the particle, independent of the state of polarization of the incident wave, is the sum of contributions of the different multi-poles. The $l = 1$ term is the dipolar term, $l = 2$ the quadrupolar, etc...The scattering cross section is given by:

$$\sigma_{sca} = \frac{2\pi}{n_m^2 k_0^2} \sum_{l=1}^{\infty} (2l+1)\{|a_l|^2 + |b_l|^2\}, \tag{5.15}$$

while the extinction cross section is given by:

$$\sigma_{ext} = \frac{2\pi}{n_m^2 k_0^2} \sum_{l=1}^{\infty} (2l+1) Re\{a_l^2 + b_l^2\}. \tag{5.16}$$

The absorption cross section is deduced from σ_{sca} and σ_{ext}:

$$\sigma_{abs} = \sigma_{ext} - \sigma_{sca}. \tag{5.17}$$

As we have seen before, the SPR appears as a peak in the absorption cross section. However, experimentally we always measure the extinction cross section, in which both scattering and absorption contribute. We have used Mie theory to calculate the extinction, scattering and absorption cross sections. Figure 5.5 shows the results obtained for Ag NPs of 4 nm (Fig. 5.5(a)) and 100 nm of diameter (Fig. 5.5(b))

In the case of small particles $\sigma_{sca} \approx 0$ and $\sigma_{abs} \approx \sigma_{ext}$. This is valid for NPs having diameters smaller than 10 nm, which corresponds to the quasistatic approximation ($\lambda << D$). However, when the diameter increases (>10 nm), the extinction spectra is dominated by scattering and presents several peaks (Fig. 5.5(b)). These peaks are due to multi-poles induced in this large NP, as it will be shown at the end of this section. Only the extinction cross-section is plotted in the following.

The extinction cross-section spectra calculated using the Mie theory are plotted in Fig. 5.6, as a function of the diameter. For diameters smaller than 10 nm the SPR peak remains at the same wavelength since the dipolar term is dominant. Indeed, the lower term in σ_{ext} is the dipolar term determined with the quasi static approximation. When the NP size increases ($D >$ 10nm) multi-polar terms are not negligible and the SPR shifts to the red. As the diameter of the particle increases these multi-polar terms are also responsible for the multi-polar SPR peaks observed in Fig. 5.5(b) and in the calculated spectra presented in Fig. 5.7.

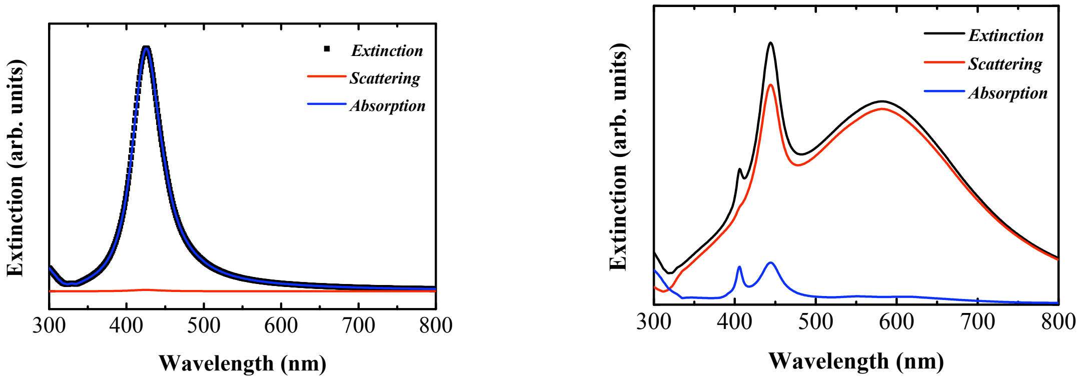

(a) (b)

Figure 5.5: Calculated extinction, scattering and absorption spectra of spherical Ag NPs embedded in a−Al_2O_3, calculated using Mie theory for (a) D= 4 nm and (b) D= 100 nm.

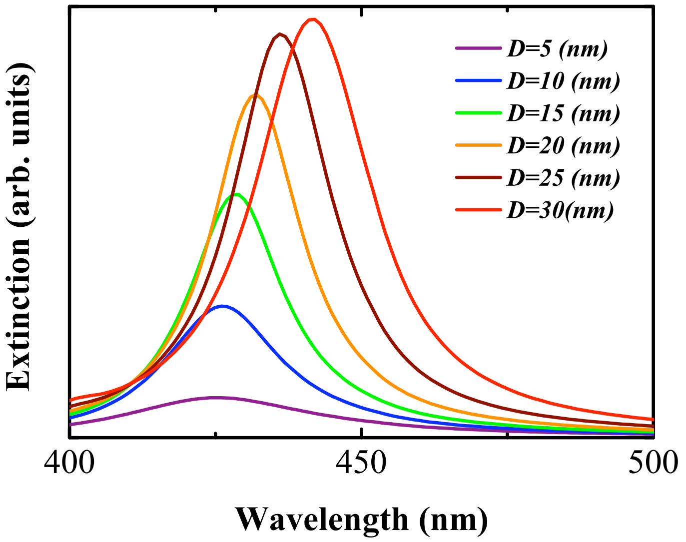

Figure 5.6: Calculated extinction cross-section of Ag NPs embedded in a−Al_2O_3 with diameter ranging from 5 nm to 30 nm

As discussed above, multipolar peaks are not observed in the experimental spectra measured in the present work, since the NPs produced are smaller than 10 nm.

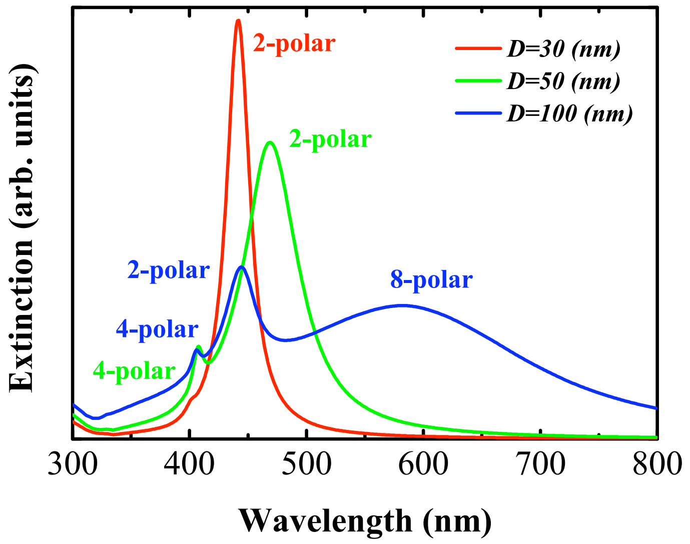

Figure 5.7: Calculated extinction of Ag NPs embedded in $a{-}\mathrm{Al_2O_3}$ with diameter ranging from 30 nm to 100 nm. 2-polar, 4-polar, and 8-polar stand for dipolar, quadrupolar, and octupolar modes, respectively.

We have presented the case of an isolated spherical NP embedded in a dielectric matrix. Since in this work we are also interested in elongated NPs, we need to modify these models for spheroids. This was done by Gans who extended Mie's theory to non-spherical particles.[?]

5.2.3 Isolated spheroidal particle: Rayleigh-Gans Model

An ellipsoidal particle is defined by three axis a, b, and c with a≠b≠c. In the case of b=c, then a is parallel to the revolution axis. This is a particular ellipsoid named spheroid. If a<b=c the spheroid is oblate, while if a>b=c the spheroid is prolate as shown in Fig. 5.8.

The extinction cross-section of a prolate ellipsoid is given by the Rayleigh-Gans model:[?,?,?]

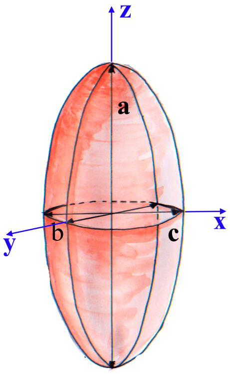

Figure 5.8: Prolate spheroid. Two of its axes are equal ($b = c$) and shorter than the third one $a > b, c$.

$$\sigma_{ext} = \frac{2\omega}{3c} V \epsilon_d^{3/2} \sum_{j=a}^{c} \frac{\left[\frac{1}{P_j^2}\right] \epsilon_2}{\left[\epsilon_1 + \frac{1-P_j}{P_j}\epsilon_d\right]^2 + \epsilon_2^2} \tag{5.18}$$

where P_j is the depolarization factor along the j axis of the ellipsoid given by:

$$P_a = \frac{1-e^2}{e^2}\left[\frac{1}{2e} ln\left(\frac{1+e}{1-e}\right) - 1\right], \tag{5.19}$$

and

$$P_b = P_c = \frac{1-P_a}{2}, \tag{5.20}$$

with

$$e = \left[1 - \left(\frac{a}{b}\right)^2\right]^{1/2}. \tag{5.21}$$

Figure 5.9 shows a calculated extinction cross section spectrum of an isolated prolate Ag NP considering that the z-axis forms an angle of 45° with respect to the direction

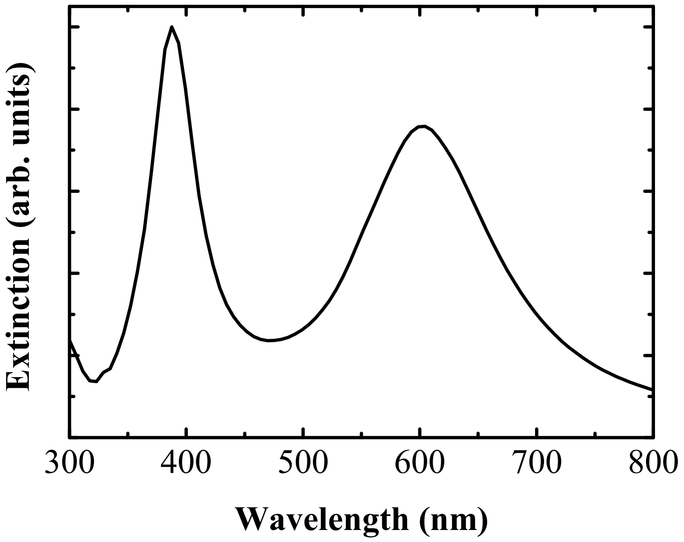

Figure 5.9: Calculated extinction of a prolate Ag NP with $a = 7$ nm and $b = c = 3$ nm embedded in $a\text{−}Al_2O_3$.

of light propagation. Two peaks are observed at 390 nm and 600 nm corresponding to the transverse SPR (oscillations of the electron gas in the plane defined by x and y) and to the longitudinal SPR (oscillations of the electron gas along a direction parallel to the z-axis) respectively. Obviously, the shape (prolate or oblate) affects the SPRs. This is shown in fig. 5.10 where the wavelengths of the transverse and longitudinal SPR are plotted as a function of the aspect ratio a/b.

For a spherical NP both SPRs are degenerated due to the spherical symmetry: the amplitude of the oscillations is the same along all axes of symmetry. When the particle evolves to a spheroid, the SPRs are not longer degenerated and the splitting into transverse and longitudinal SPRs appears.[?,?] In the case of prolate particles the longitudinal mode is shifted to longer wavelengths (high amplitude of oscillations). In the case of oblate particles it is instead shifted to shorter wavelengths (small amplitude of oscillations).

At this point, we are able to calculate the extinction cross section of small isolated NPs of different shapes. However, in real samples, NPs are rarely isolated. Thus, it is necessary to take into account the number density of NPs. The simplest way to take into account the number density is to use effective medium theory.

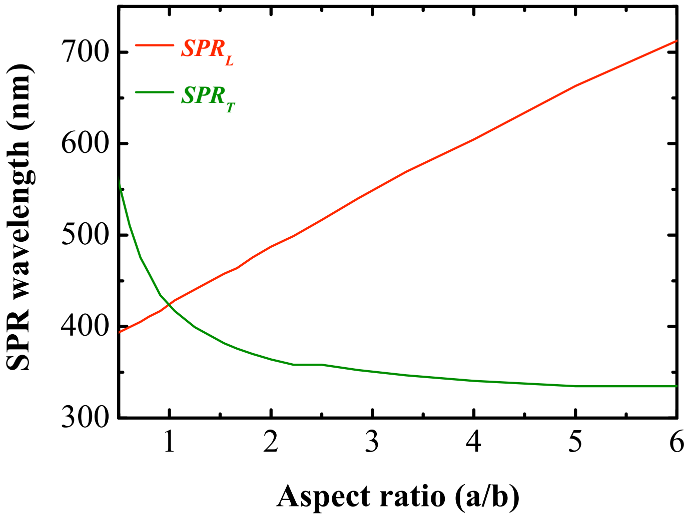

Figure 5.10: Calculated position of the transverse, SPR$_T$, and longitudinal, SPR$_L$, SPRs of a Ag ellipsoidal NP embedded in $a-\mathrm{Al_2O_3}$ as a function of the aspect ratio a/b

5.2.4 Effective medium containing spheroidal nanoparticles: Maxwell-Garnett

Effective medium theories are valid when the NPs are much smaller than the optical wavelength. In this case the material formed by the NPs embedded in a matrix can be approximated to an optically homogenous medium that is characterized by an effective dielectric constant.

In the case of Maxwell-Garnett theory,[?,?] the distribution of the NPs in the medium is described by the volume fraction of metal f dispersed in the dielectric matrix. The interaction of the electromagnetic wave with this composite medium is described by the total induced polarization: sum of the polarization due to the metal NPs ($\mathbf{P}_{NPs}$) and to the dielectric matrix ($\mathbf{P}_m$). In the quasi static approximation we obtain:

$$\mathbf{P} = \mathbf{P}_{NPs} + \mathbf{P}_m = \frac{f}{V}\mathbf{p} + \epsilon_0(\epsilon_m - 1)\mathbf{E} \tag{5.22}$$

where $\mathbf{p}$ is the dipolar momentum of one NP. In the case of an ellipsoid we have seen that the dipolar momentum can be expressed as a function of the depolarization factors

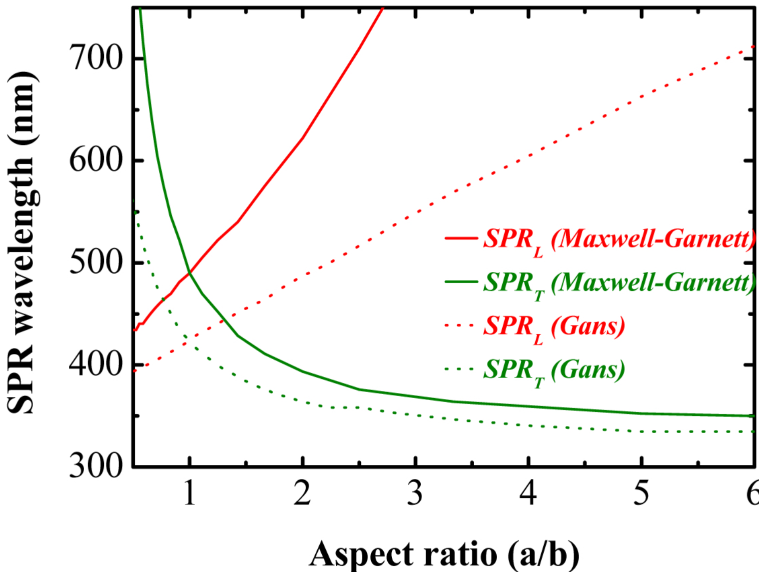

Figure 5.11: Calculated position of transverse, SPR$_T$, and longitudinal, SPR$_L$, SPRs of Ag NPs (f = 30%) embedded in $a{-}Al_2O_3$ as a function of the aspect ratio a/b. The dot lines show the calculations for isolated NP (Gans model)

$\mathbf{P}_j$. Thus, the effective dielectric constant of the composite medium $\tilde{\epsilon}^{eff}$ is defined using the relation $\tilde{\epsilon}^{eff}\epsilon_0\mathbf{E} = \epsilon_0\mathbf{E} + \mathbf{P}$ that gives, replacing all the terms in Eq. 5.22, the Maxwell-Garnett relation:

$$\epsilon_j^{eff} = \epsilon_m + f\epsilon_m \frac{\tilde{\epsilon} - \epsilon_m}{\epsilon_m + (\mathbf{P}_j - \frac{f}{3})(\tilde{\epsilon} + 2\epsilon_m)}. \tag{5.23}$$

As seen in this equation, this effective medium theory neglect the interactions among NPs.

The total absorption cross-section is obtained by replacing $\tilde{\epsilon}$ by $\tilde{\epsilon}_j^{eff}$ in Eq. 5.9. Figure 5.11 shows the wavelength of the SPRs for f=30%, as a function of the aspect ratio of spheroidal Ag NPs embedded in a-Al$_2$O$_3$. The values are compared to the case of an isolated NP. We observe that both the transverse and longitudinal SPR modes are red-shifted with respect to the case of an isolated particle. For prolate ellipsoids the predicted split between both modes is much larger in the case of Maxwell-Garnett model.

5.3 Vibrational properties of metal nanoparticles

5.3.1 Vibration of a spherical nanoparticle

When the size of a metal is reduced down to the nanoscale, the vibrations of the metal atoms are confined leading to size quantization of the vibrational density of states. The free oscillations of an isotropic and homogenous elastic sphere were studied very early by Lamb[?] using the theory of elasticity. This model is valid for NPs with sizes much larger than the inter-atomic distance, which is generally the case in this work since the diameter of the particles studied ranges from 1 to 10 nm. In this section we present the most important steps needed to define the vibration modes and to calculate their vibration frequencies.

When a vibration wave propagates in a medium, an elementary volume dV is displaced by a quantity $\mathbf{U}$ with respect to its original position. This generates a deformation characterized by a deformation tensor given by:[?,?]

$$\epsilon_{i,j} = \frac{1}{2}\left(\frac{\partial U_i}{\partial x_j} + \frac{\partial U_j}{\partial x_i}\right). \tag{5.24}$$

To describe the vibrational properties, it is imperative to know the forces that are imposed by the external medium on the element dV. They are pressure forces, that can be introduced using a tensor of stress σ. The sum of forces applied to the surface is thus given by:[?]

$$\mathbf{F} = \oint \sigma \mathbf{e}_n . dS \tag{5.25}$$

where $\mathbf{e}_n$ is the vector normal to the surface. The relation between stress and deformation is not trivial. However in the case of an isotrope medium, we can use the Lamé coefficients,[?] λ and μ, to express the stress tensor:

$$\sigma_{i,j} = \lambda \delta_{ij} \sum_k \epsilon_{kk} + 2\mu\epsilon_{ij} \tag{5.26}$$

where δ_{ij} is the Kronecker symbol. Neglecting the volume forces, we obtain:?

$$\rho\frac{\partial^2\mathbf{U}}{\partial t^2} = (\lambda + 2\mu)\nabla(\nabla \bullet \mathbf{U}) - \mu\nabla \times (\nabla \times \mathbf{U}) \tag{5.27}$$

where ρ is the volume mass. This is the equation of Navier which allows to introduce the longitudinal, v_l, and transverse, v_t, velocities given by:

$$v_l = \sqrt{\frac{\lambda + 2\mu}{\rho}} \quad \text{and} \quad v_t = \sqrt{\frac{\mu}{\rho}}. \tag{5.28}$$

In the case of a NP in vacuum, the Navier equation must be solved in spherical coordinates and written as:

$$\rho\frac{\partial^2\mathbf{U}}{\partial t^2} = A_l\nabla[j_l(Q_l r)Y_{lm}(\theta,\phi)] + B_l\nabla \times [j_l(Q_t r)Y_{lm}(\theta,\phi)\mathbf{r}] + C_l\nabla \times (\nabla \times [j_l(Q_t r)Y_{lm}(\theta,\phi)\mathbf{r}]) \tag{5.29}$$

where Q_l and Q_t are defined as:

$$Q_l = \frac{\Omega}{v_l} \quad \text{and} \quad Q_t = \frac{\Omega}{v_t} \tag{5.30}$$

Each vibration mode is labeled by integer numbers l = 0,1,2,3 ... and $-l \leq m \leq l$, according to the spherical harmonic $Y_l^m(\theta,\varphi)$ functions. The vibration mode frequency $\omega_{l,m}$ is $2l+1$ fold degenerated. The additional integer $n \geq 1$ refers to the harmonic frequencies.

Then, surface forces are given by:

$$\mathbf{F} = \left[\lambda\nabla \bullet \mathbf{U} + \mu\frac{\mathbf{U}.\mathbf{e}_r}{r}\right] + \mu\nabla(\mathbf{U}.\mathbf{e}_r) + \mu\frac{\partial\mathbf{U}}{\partial r} - \mu\frac{\mathbf{U}}{r} \tag{5.31}$$

where $\mathbf{e}_r$ is a unitary vector along $\mathbf{r}$. For a free standing NP, the forces at the NP surface are null, thus:

$$\mathbf{F}(R\mathbf{e}_r) = \mathbf{0}. \tag{5.32}$$

Two types of vibration modes, $\mathbf{U}$, are solutions for this equation:

1. Torsional modes, purely transverse. The volume of the NP remains constant, the vibration propagates "rotating" around the axis of symmetry of the sphere whose number is infinite.
2. Spheroidal modes. The vibration propagates along the radius of the NP which induces volume changes.

The torsional modes are not observed by Raman scattering? and will be thus disregarded in the following. Moreover, only two types of spheroidal modes contribute to the Raman scattering :

- the radial mode not degenerated ($l = 0, n$)
- the quadrupolar mode which is five-fold degenerated ($l = 2, n$).

Experimentally it has been observed that mainly quadrupolar modes (n, l= 2) contribute to the low-frequency Raman scattering,?,?,? since the modulations of the dipolar SPPs produced by the radial modes (n, l=0) are much weaker. The vibration band observed experimentally arises from the modulation of surface polarization charges via a deformation potential mechanism. The modulation is due to a modification of the NP surface orientation during the NP oscillations.?,?

For a homogenous sphere of diameter D, the frequency of a vibration mode expressed in cm^{-1} and characterized by the numbers l and n is inversely proportional to the sphere diameter, and is given by:

$$\omega_{l,n} = S_{l,n}\frac{v_l}{Dc}, \tag{5.33}$$

where $S_{l,n}$ is a coefficient which depends on the v_l/v_t ratio for each pair of l and n values. In this equation, the diameter of the sphere and the light velocity must be expressed in centimeters and v_l in cm.s^{-1}. Table 5.1 shows some values of this coefficient for the case of a Ag sphere.?

$S_{l,n}$	$n = 1$	$n = 2$	$n = 3$
$l = 0$	0.90	1.96	2.97
$l = 1$	0.53	1.06	1.36
$l = 2$	0.38	0.75	1.26

Table 5.1: First values of $S_{l,n}$ for a free Ag sphere

We have chosen here to introduce the simple Lamb's model. However, the vibration frequencies calculated in the rest of this work have been obtained using Molecular Dynamic simulations or the resonant ultra sound method.?

5.3.2 Some considerations for the case of an ellipsoid

In the case of ellipsoidal NPs, such as those presented above for the Gans model, to the equation 5.32 must be solved in spheroidal coordinates. In that case the quadrupolar vibration modes are not truly spheroidal, and will be referred to as spheroidal-like modes. Since the symmetry is different from that of spherical NPs, vibrations with different amplitudes will appear along the axis of symmetry, exactly as in the case of the transverse and longitudinal SPR. When increasing the aspect ratio, the degeneracy of the spheroidal-like modes is partially lifted. Then if $a \neq b \neq c$, three levels of energy corresponding to $m = \pm 2$, $m = \pm 1$ and $m = 0$ appears and thus, three vibration peaks are expected in the Raman spectrum. Nevertheless, these vibration modes depend on the incident light polarization and wavelength, and therefore might not be necessarily simultaneously observed.

5.4 Conclusions

The theoretical models used to describe the optical and vibrational properties summarized in this chapter have pointed out the importance of several parameters on the final properties of our nanostructures, since each parameter induces changes on the SPR and vibrations modes. The main parameters are:

- **The matrix:** The SPR shifts to the red as ϵ_m increases.
- **The NP Size:** The dielectric function, the SPR and the acoustic vibration modes are generally size dependent. Nevertheless, for NPs having a diameter smaller than 10 nm, which is the case considered in this work, the SPR wavelength is almost not affected while the acoustic vibrations are clearly affected, since the frequency of vibration shifts to lower values as D increase. Moreover, the orientation of the incident electric field plays an important role in the case of spheroidal NPs.
- **The NP shape:** The SPR and acoustic vibration modes of a spherical NP are degenerated. However, when the aspect ratio of NPs is different from one, this degeneracy is broken leading to the appearence of transverse and longitudinal SPRs and vibration modes with different frequencies. Thus, it is possible to tune the SPR wavelength and acoustic vibrations frequency by changing the shape.
- **The NPs number density and volume fraction:** The splitting of the transverse and longitudinal SPR is dependent on the number density of NPs, while the acoustic vibration modes are not affected since they are confined to the NPs volume. In this work, the number density of Ag NPs is kept almost constant, nevertheless this parameter should be taken into account in future work.

In the present work $\epsilon_m \approx 2.8$ in the spectral range studied, the metal is Ag, the characteristic dimensions of the NPs are smaller than 10 nm, and the volume fraction is almost constant ($f = 30\%$) in all the sampe containing only Ag NPs. Therefore, the parameters that can be varied are the shape and the size.

Part IV

Optical and Vibrational properties of the nanocomposite thin films

6

Optical & vibrational characterization

This chapter describes the experimental techniques used in this work for the optical and vibrational characterization of the nanocomposite films. The extinction/transmission measurements and the low frequency Raman spectroscopy are complementary tools for the analysis of "nano-designed" samples, since they provide information on the optical and vibrational properties that can be related to the morphology and organization of the metal NPs.

6.1 Optical extinction of thin films

The optical measurements were recorded using a WVASE JA Woollman spectroscopic ellipsometer. A scheme of the setup is presented in Fig. 6.1. The sample is mounted on a substrate holder, and placed into the light beam. The light transmitted trough the sample is detected by a photo-multiplier (detector) and the signal is recorded by the computer. The angle of incidence can be varied by rotating the sample holder and the light beam can be either p- or s-polarized. The spectral resolution of the monochromator is $\Delta\lambda$=3.5 nm and the investigated spectral range is 300-800 nm.

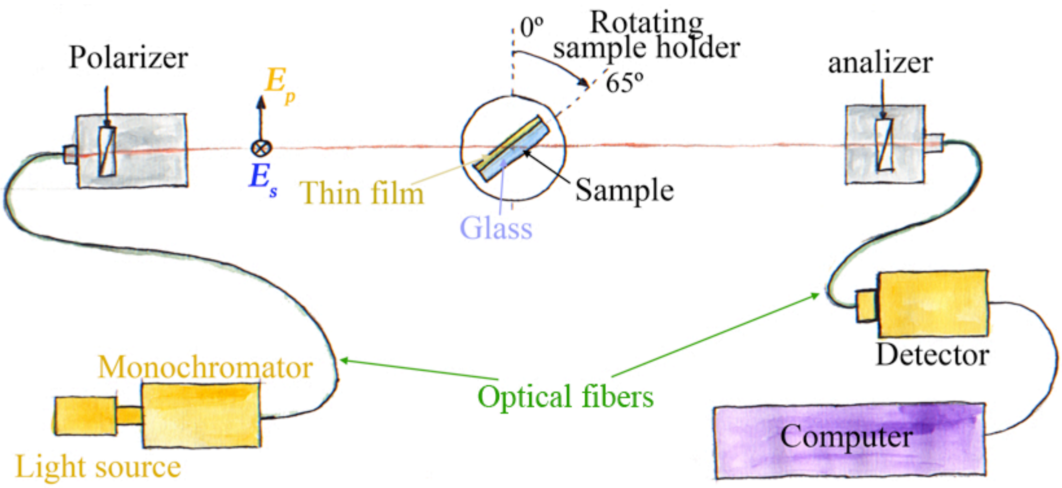

Figure 6.1: Scheme of the experimental setup used for extinction measurements. The letters p and s in the scheme correspond to the p- and s-polarization of the incident electric field, respectively.

According to the Lambert-Beer law, the transmitted light intensity is:

$$I(x) = I_0 e^{-\alpha x}, \quad \text{with} \quad ln(1/T) = ln(I_0/I(x)) = \alpha x \tag{6.1}$$

where T is the transmission, x the thickness of the absorbing medium, and I_0 and $I(x)$ are the incident and transmitted intensities, respectively. Thus, the extinction spectrum $\alpha(\lambda)x$ is given by $ln(1/T)$.

In this case, we need to take into account the reflections at the air/film and film/substrate interfaces. Figure 6.2 presents a schematic of a thin film, having a complex refractive index $\tilde{n} = n + i\kappa$, deposited on top of a purely dielectric transparent material with refractive index n_2, the whole sample being in air ($n_0 = 1$).

The incident wave impinges on the thin film with an angle of incidence θ_{inc}. This corresponds to an angle of incidence θ_{mat} inside the thin film given by the Snell-Descartes law:?

$$n_0 \sin\theta_{inc} = \mathcal{R}e(\tilde{n}) \sin\theta_{mat}. \tag{6.2}$$

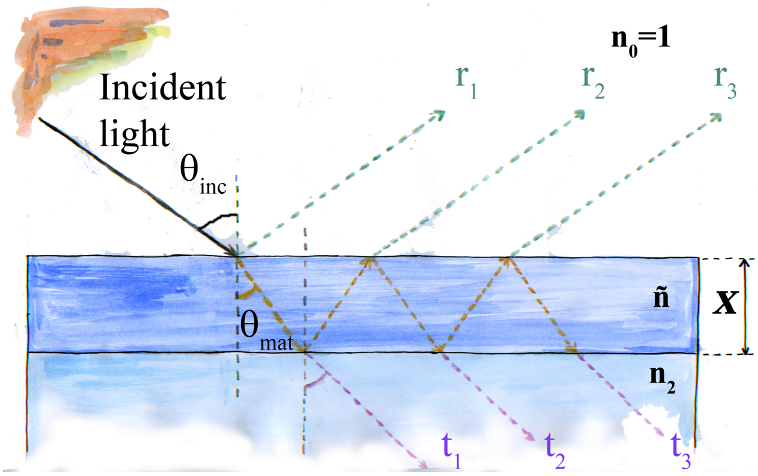

Figure 6.2: Reflected and transmitted beams at the interface between the air and an optical thin film of thickness X and refractive index $\tilde{n}$, deposited on top of a semi-infinite dielectric medium with refractive index n_2. The reflected and transmitted waves are r_i and t_i, respectively.

Reflected and transmitted waves are formed by the superposition of the reflected and transmitted beams at both interfaces. r_1 and t_1 are the principal reflected and transmitted waves respectively, while $r_{2,3,\ldots}$ and $t_{2,3,\ldots}$ correspond to the partial reflected and transmitted waves. The transmitted wave is thus the sum of the principal transmitted wave, t_1, with all the partial transmitted waves $t_{2,3,\ldots}$ which are de-phased due to the different paths followed by the waves.

Transmission of thin films containing NPs

In thin a-Al_2O_3 films containing NPs, optical extinction is caused by the NPs since $a - Al_2O_3$ is transparent in the visible optical range ($\kappa \approx 0$).

Figure 6.3 shows a schematic of a thin film containing metal NPs of different shapes (a) prolate ellipsoid, (b) sphere, and (c) oblate ellipsoid with their symmetry axis perpendicular to the substrate surface. For spherical NPs whatever the polarization of the light, the SPR should not change due to the spherical symmetry. However, in the case of oblate or prolate NPs there is only one axis of symmetry, along the revolution axis z. If the incident beam is s-polarized, whatever the angle of incidence, the polarization is perpendicular to z and only the transverse SPR can be observed. When the light is p-polarized the polarization has two components along x and z. In this case the extinc-

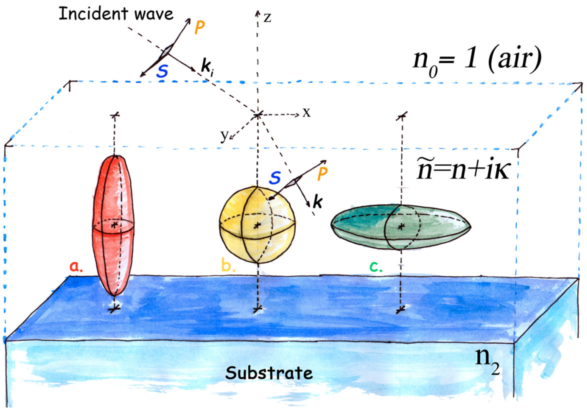

Figure 6.3: Schematics of a thin film containing NPs of different shapes. From left to right prolate, spherical and oblate NPs. The angle of incidence is 65° outside of the thin film and 33° inside it. P and S stand for the components of ***E*** parallel and perpendicular to incident plane.

tion spectra presents two peaks corresponding to the transverse (x) and longitudinal (z) SPRs for prolate and oblate spheroids.

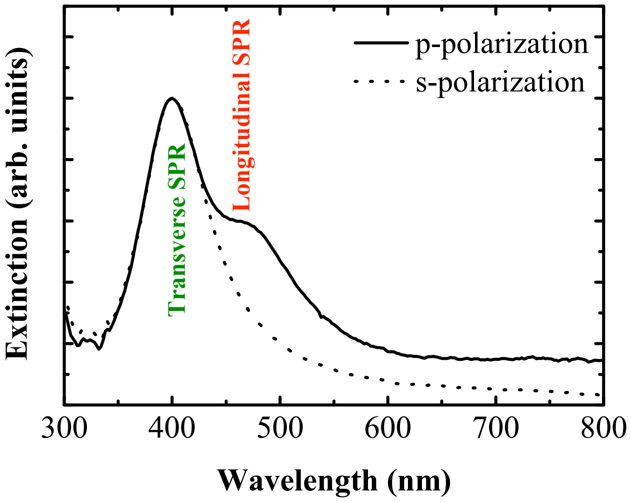

Figure 6.4: Experimental extinction spectra of Ag NCls recorded using p- (continous line) and s-polarized light (dotted line) and an angle of incidence of 65°.

Most of the measurements presented in this work correspond to p-polarization at an angle of incidence of 65 degrees since this allowed to clearly observe the splitting of the SPRs upon a modification of the NP shape. Figure 6.4 presents a typical extinction spectrum of NCls obtained under these conditions. As expected, for p-polarization, two peaks are observed at 390 nm and 470 nm, which correspond to the transverse and longitudinal SPR, respectively, whereas only the transverse SPR is observed for s-polarization.

6.2 Low Frequency Raman Spectroscopy

Raman experiments have been performed using a triple spectrometer with a high rejection of the Rayleigh scattering, which is presented schematically in Fig. 6.5. The sample is excited using the emission lines of Argon or Krypton lasers that cover the 400 to 800 nm wavelength range. The sample is kept in vacuum to avoid the low frequency lines of air. The scattered light is then analyzed by a triple monochromator (CODERG T800). Each monochromator uses a diffraction grating of 1800 grooves/millimeter. Finally, a photomultiplier (single channel detector) is used for the photon counting.

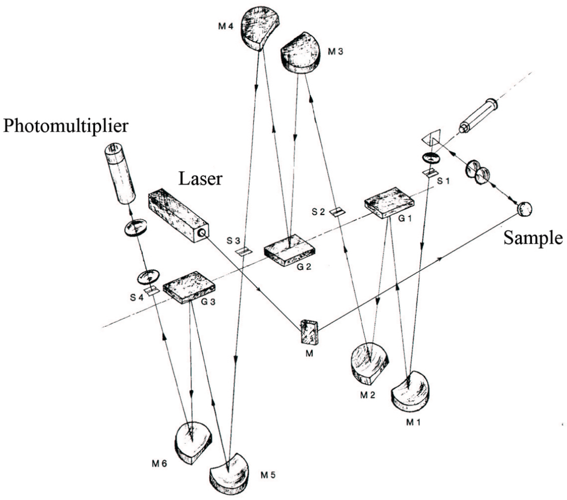

Figure 6.5: Scheme of the experimental setup used for Raman analysis. The scattered beam is analyzed using a triple monochromator (Coderg T800). The letters G in the scheme correspond to the diffraction gratings, S to the entrance and exit slits, and M to the mirrors.

Raman spectra have been acquired mostly in p-polarization close to the SPR_T or SPR_L. In Fig. 6.6 a typical Raman spectrum of a sample containing NCls ($H = 6.7$ nm and $D = 2.7$ nm) is plotted. The central peak at 0 cm^{-1} corresponds to Rayleigh scattering. Anti-Stokes and Stokes Raman signals due to acoustic vibrations of the NCls are observed. In the following, we will often present only the Stokes part.

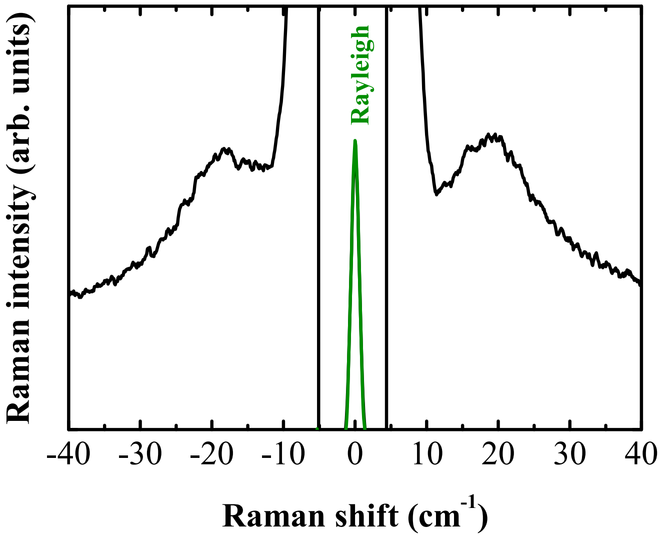

Figure 6.6: Experimental Stokes and anti-Stokes room temperature Raman spectrum of Ag NCls excited at 488 nm. The incident laser beam was p-polarized and the polarization of the scattered beam was not analyzed.

The band observed at ≈ 20 cm^{-1} correspond to the acoustic vibration modes of Ag NCls. Its position depends on the morphology of the NPs. Therefore, the combination of the extinction and Raman analysis provides useful information about the morphology of the nanostructures. In Chapters 7 and 8 we used these techniques to characterize our samples and we present the results of these studies.

7

Tuning Plasmons and Vibrations of Ag nanostructures

We have shown in Chapter 3 that it is possible to modify the size, shape and distribution of metal NPs using a-PLD, while in Chapter 5 we have introduced the models that describe their optical response. In this chapter we study the optical behavior of the nanocomposites produced by PLD described in Chapter 3. In order to establish the correlation between the deposition parameters and the SPR features, each deposition parameter is studied independently to avoid simultaneous contributions to the optical response.

7.1 Size and shape effects on the optical and vibrational response

In Chapter 3 we have shown that we can increase the size of the NPs by increasing the ablation time of the Ag target. When the multipolar terms are neglected, the models presented in Chapter 5 predict for the case of perfectly spherical and isolated NPs that the SPR should not be affected by a change of the NPs size for diameters smaller than ∼10 nm. Therefore, we can check if these models allow explaining the observed optical and vibrational response of the produced NPs. Fig. 7.1 shows the optical extinction spectra, measured using the configuration presented in Chapter 6, of samples consisting of Ag NPs embedded in a-Al_2O_3. The deposition time of the Ag NPs has been varied in the range from 30 to 70 seconds, which, according to Fig. 2.2 in Chapter 2, leads to NPs of average diameters ranging from 3 to 5 nm.

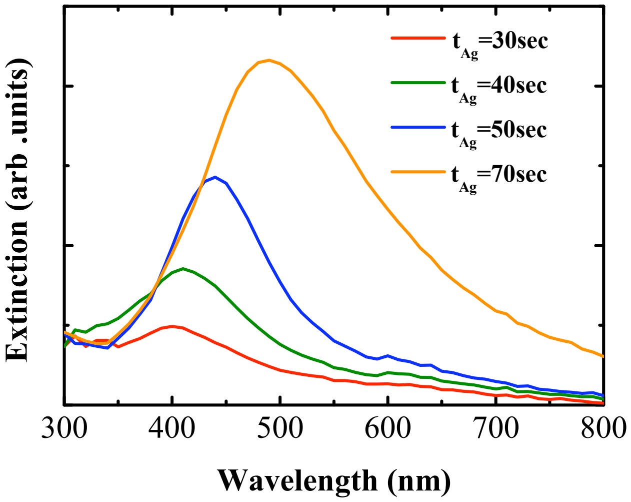

Figure 7.1: Experimental extinction spectra of samples containing silver NPs recorded using p-polarized light at normal incidence.

For t_{Ag}= 30 seconds and 40 seconds, the wavelength of the SPR and the FWHM are almost constant, which implies that the NPs diameters are small and the size dispersion is low. For t>40 seconds, the SPR shifts to the red as the NP diameter increases while the SPR width broadens. The origin of this discrepancy with the theoretical models lies is twofold. First, the experimental NP size dispersion (σ) is not zero and second, the shape of the NPs changes from spherical to oblate spheroidal once the amount of metal deposited reaches a certain threshold (limit between Region I and Region II Fig. 2.2). This is due to the coalescence effect described in Chapter 2. As it would be expected, this behavior is much more evident for the sample containing the largest NPs.

The evidence for non-spherical NPs is shown in Fig. 7.2, where the optical exctinction spectra measured for the largest NPs using p-polarized light at two angles of incidence

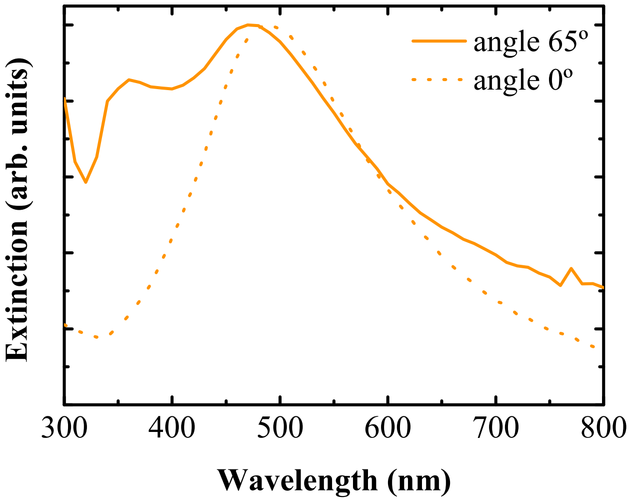

Figure 7.2: Experimental extinction spectra of silver NPs (t_{Ag}=70 sec) recorded using p-polarized light and an angle of incidence of (dotted-line) 0° and (continuous-line) 65°.

(0° and 65°) are presented. As expected for normal incidence, only the transverse SPR is observed at 470 nm (see Chapter 6), while for non-normal incidence two peaks are visible. The transverse SPR is still observed at 470 nm while the longitudinal peak appears around 360 nm. The blue shift of the longitudinal SPR and the red shift of the transverse SPR are characteristic of oblate spheroidal NPs, and confirm the in plane coalescence.

We have measured the low frequency Raman spectra of these NPs. Figure 7.3 shows the Stokes Raman spectra recorded at low frequencies close to the Rayleigh scattering (centered at 0 cm^{-1})[*]. Fig. 7.3 presents spectra excited at λ=413 nm, which is close to resonance with the SPR for t_{Ag} in the range 30 to 50 seconds (Fig. 7.1). However,this wavelength is out of resonance with transverse or longitudinal SPR for the case of t_{Ag}=70 seconds. As discussed in Chapter 5 the observed Raman bands are associated with the quadrupolar acoustic modes of the NPs. Their frequencies are in the range 15 cm^{-1} to 20 cm^{-1}, and downshift of the Raman signal is observed with increasing NPs size (t_{Ag} increases). The frequencies, ω, at the maximum intensity of the Raman peaks are summarized in Table 7.1. We have used Lamb's theory (Chapter 5) to calculate the diameters, D_{cal}, of the NPs using the experimental values of ω. They are also

---

[*] This has been performed recently on a new T64000 spectrometer

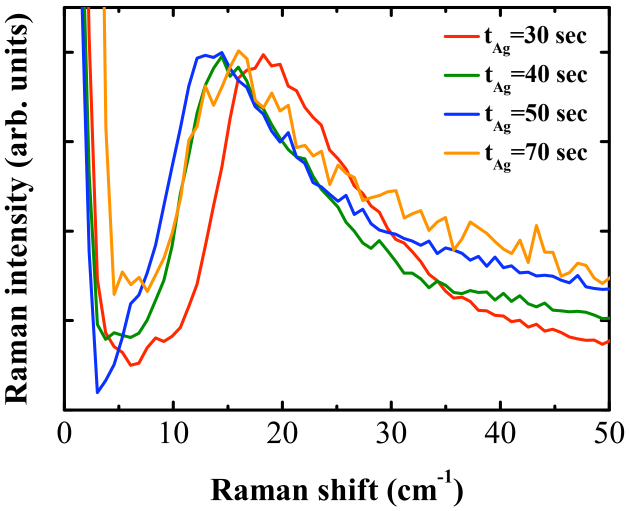

Figure 7.3: Experimental Stokes Raman spectra of Ag NPs of different sizes excited at 413 nm. The incident laser beam was p-polarized and the polarization was not analyzed.

summarized in Table 7.1.

$\mathbf{t}_{Ag}$	ω (cm^{-1})	D_{cal} (nm)
30 sec	18 ± 1	2.8 ± 0.1
40 sec	15 ± 1	3.3 ± 0.1
50 sec	13.5 ± 1	3.6 ± 0.1
70 sec	14.5 ± 1	3.5 ± 0.1

Table 7.1: Raman peak frequencies and estimated diameters

For $t_{Ag} = 30$, 40 and 50 seconds, D_{cal} values agree very well with the expected diameters, while in the case of $t_{Ag} = 70$ seconds, D_{cal} is smaller than expected. For $t_{Ag} < 50$ seconds, the NPs are nearly spherical, and the samples are excited close to the resonance with the SPR. Instead, for $t_{Ag} = 70$ seconds, this is not the case, since the NPs are clearly oblate spheroids (Fig. 7.2). As shown in Chapter 6, the experimented were performed using p-polarized light under an incidence of 65 degrees, thus both plasmons can be excited. Here, at 413 nm, neither the transverse nor the longitudinal SPR are excited in resonance. In this case, the shape effect should be taken into account and thus the diameters cannot be calculated using the Lamb's model. Nevertheless, extinction and Raman spectra and the simple Lamb's model provide already relevant information on the size and shape of NPs.

7.2 Shape effect: From nanolentils to nanocolumns

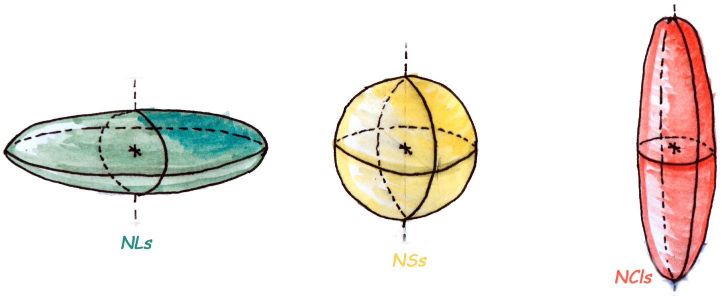

Figure 7.4: Different NPs shapes considered in the present work

We have studied the optical response of the three different NP morphologies that have been produced by a-PLD : spheres (nanospheres: NSs), oblate spheroids (nanolentils: NLs), and prolate spheroids (nanocolumns: NCls).[?,?,?] Figure 7.4 illustrates these different shapes that are considered in this section.

TEM images of the samples were presented in Fig. 3.2 and Fig. 3.6, therefore we summarize in table 7.2 their average diameter D and height H.

Shape	D (nm)	H (nm)
NS	3.4±0.2	3.4±0.2
NL	9.1±1.0	5.2±0.2
NCl	2.7±0.2	6.7±0.2

Table 7.2: Average diameter, D, and height, H, determined from TEM analysis of the NPs considered in this section.

The production of NPs having different morphologies is based on the different nucleation and growth mechanisms that were discussed in Chapter 2. The production of NSs is limited to small NPs and requires to remain below the coalescence threshold. On the contrary, oblate NPs arise from coalescence and thus, their in-plane average dimensions increase as the amount of metal increases, while the dimension along the direction perpendicular to the substrate remains smaller and tends to saturate. Such spheroids are randomly oriented in the plane parallel to the substrate, and their optical response is dominated by the NP average in-plane dimension. Therefore, the randomly oriented coalesced NPs behave optically as NLs characterized by their diameter, D, and height, H. Finally, prolate ellipsoids or NCls are obtained by producing nearly overlapping layers of spherical NPs as it was described in Chapter 2.

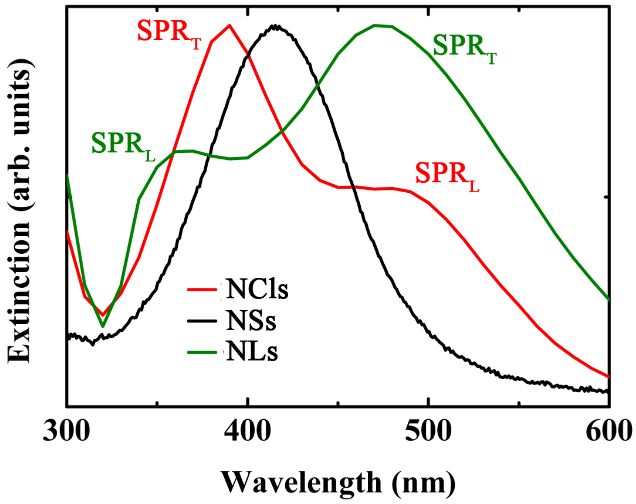

Figure 7.5: Experimental extinction spectra of samples containing NCls, NSs, and NLs, recorded using p-polarized light and an angle of incidence of 65°. T and L indicates the transverse and longitudinal modes of the SPR.

Figure 7.5 shows extinction spectra of nanocomposite films containing each type of NPs recorded using p-polarized light. As expected, the transverse and the longitudinal SPRs are degenerate in the case of NSs due to spherical symmetry, and a single SPR band appears at 420 nm. When the NPs are distorted to NLs or NCls, the spherical symmetry is broken and the SPR band splits into transverse, observed at 470 and 390 nm, and longitudinal SPRs at 360 and 470 nm, for NCls and NLs, respectively. According to the models presented in Chapter 5, this splitting depends on the aspect ratio of the NPs and their number density. The transverse resonance is shifted into the blue when H/D is smaller than 1 and the opposite occurs for H/D larger than 1. The experimental observation of splitting evidences that it is possible to identify the oblate or prolate shape of the NPs through the spectral shifts of the transverse and longitudinal modes.

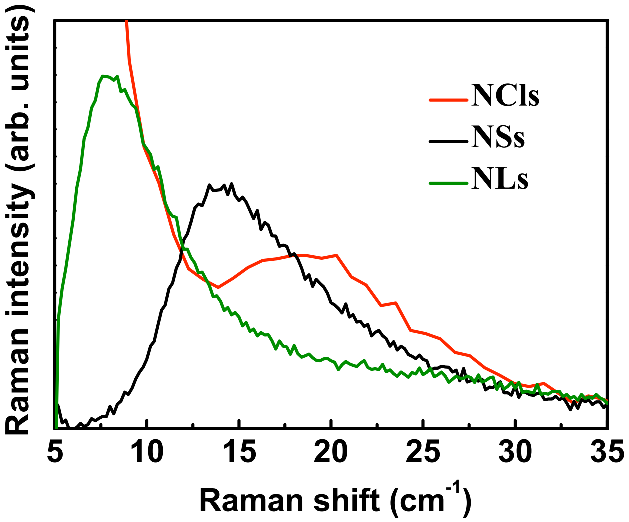

Figure 7.6: Experimental Stokes Raman spectra of Ag NCls, NSs, and NLs excited at 413 nm (NCls and NSs) and 514 nm (NLs). The incident laser beam was p-polarized and the polarization of the scattered light was not analyzed.

As discussed in section 7.1, the Raman spectra are also influenced by the shape of the NPs. We can analyze in detail this issue by comparing the Raman spectra of the three types of NPs. Figure 7.5 shows low-frequency Raman spectra of NCls, NSs, and NLs where it is seen that the vibration band shifts to lower frequencies as the shape evolves from NCl to NL. The Raman spectra are measured with p-polarized light, and the wavelength was chosen to be close to the SPR (NSs) or SPR_T (NLs and NCls). The band observed at 15 ± 1 cm^{-1} for NSs is due to the scattering by spherical quadrupolar acoustic vibration modes. The calculated diameter using Lamb's model is D_{cal} = 3.3 ± 0.1 nm, which agrees very well with the diameters determined by TEM (Table 7.2). Vibration bands close to 19 ± 1 cm^{-1} and 8 ± 1 cm^{-2} are associated with acoustic vibrations of NCls and NLs, and are shifted to higher or lower frequencies with respect to that of the NSs. In the experimental conditions used[?,?] the shifts are not only due to change in diameter D as predicted by Lamb's theory, but also due to change in shape.[?,?] The vibration modes are not degenerated in the case of NCls and NLs and the change of the NP geometry from spherical to oblate or prolate spheroids splits the five-fold-degenerate quadrupolar vibration modes. However, due to selection rules (Chapter 5), the splitting is not observed, and only one band can be observed in the Raman spectrum.

To identify the vibration modes observed it was necessary to calculate the frequency of vibrations of each fold for NCls and NLs. These frequencies have been calculated using the resonant ultra-sound,[?,?,?] or molecular dynamics methods[?,?,?] using the values of D and H shown in table 7.2. These models do not take into account the effect of the matrix. However, in the case of Ag NPs embedded in a-Al_2O_3, we have been able to determine that the matrix induces a blue shift of 2 cm^{-1} (i.e. to higher frequencies). Taking into account this effect, in the case of NCls, we found that the active vibration fold ($l = 2$, $m = \pm 2$, $n = 0$), has a frequency of vibration of 19.2 cm^{-1}, while, for NLs, the active vibration fold ($l = 2$, $m = 0$, $n = 0$) has a frequency of 8.8 cm^{-1}. These values are in very good agreement with the experimental values presented in Fig. 7.5.

In this section we have seen that the modification of the aspect ratio, H/D, allows tuning the transverse (NLs) or longitudinal (NCls) SPRs into the infra red. However, the control is partial in the first case, since the growth of the NLs is random. On the contrary it is possible to achieve a very good control over the aspect ratio of the NCls trough the control of D and/or H, and this should lead to a better control of the optical response.

7.3 Silver nanocolumns

In Chapter 2 we introduced the protocol used to produce oriented NCls. The method consists basically to reduce the thickness X of a-Al_2O_3 (Fig. 7.7), deposited after each layer of Ag NPs, to a value equivalent to the average diameter, D, of the NPs. According to this procedure there are two possible ways to modify the aspect-ratio of the NCls : increasing the number of cycles, N, for X constant, or changing X with a fixed N.

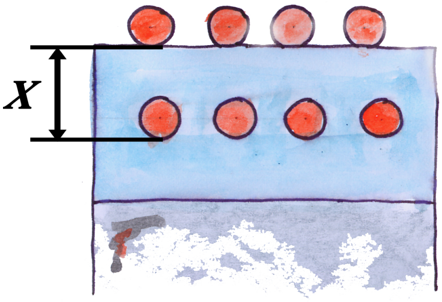

Figure 7.7: Equivalent thickness X of the a-Al_2O_3 layer between consecutive NP layers.

7.3.1 Control of the aspect ratio.

The first approach is to modify the aspect-ratio by increasing N. This should lead to an increase of H while maintaining D constant. Figure 7.8 shows the extinction spectra of four samples obtained by increasing N: 5, 10, 20, and 50, which corresponds to estimated aspect-ratios of 2.5, 5, 10, 25 . All spectra present both transverse and longitudinal SPRs, and their peak wavelengths are summarized in table 7.3.

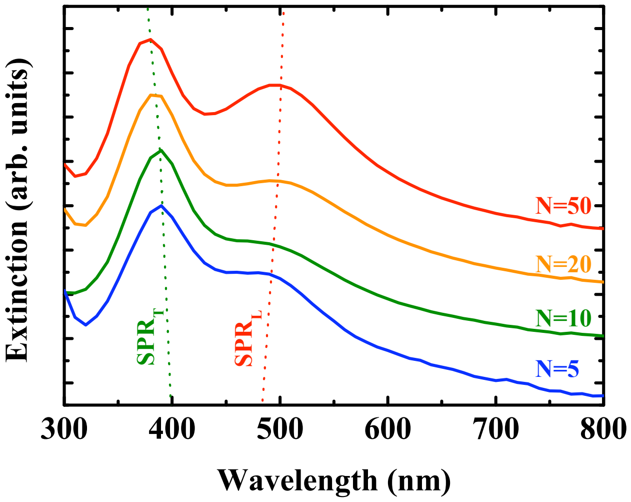

Figure 7.8: Experimental extinction spectra of samples containing Ag NCls produced with increasing N, recorded using p-polarized light and an angle of incidence of 65°. SPR_T and SPR_L stands for transverse and longitudinal SPR, respectively.

As expected the transverse and longitudinal SPRs shift to the blue and red spectral regions, respectively, as the aspect ratio increases. Even though these shifts are small they confirm the increase of the aspect-ratio of the NCls as seen in Fig. 3.9 of Chapter 3 for $N = 5$, 10 and 50. Nevertheless, the shift is much smaller than expected.

The increase of the height cannot be observed in the Raman spectra. Nevertheless, Raman analysis can demonstrate that D is kept constant when N is increased. Fig. 7.9 shows stokes Raman spectra of the four samples excited with p-polarized light at 488 nm, which is close to the longitudinal SPR.

For $N = 5$ to 20 the maximum of the vibration band is observed around ≈ 19 cm^{-1} which corresponds to NCls with $D \approx 2.7$ nm. This is in good agreement with the TEM values presented in Chapter 3. However, for $N = 50$ in addition to the band at ≈ 19

number of cycles	λ(SPR$_T$) (nm)	λ(SPR$_L$) (nm)
5	389	490
10	388	492
20	384	497
50	379	500

Table 7.3: Experimental wavelengths of the SPRs as a function of the number of cycles N.

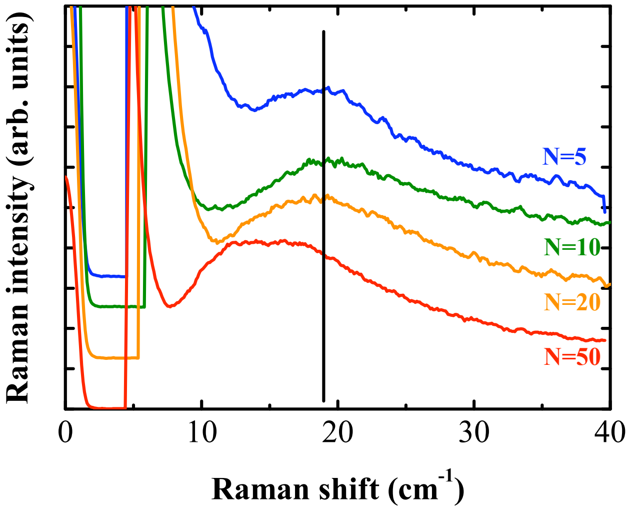

Figure 7.9: Experimental Stokes Raman spectra of Ag NCls with increasing N, excited at 488 nm. The laser beam was p-polarized and the polarization of the scattered light was not analyzed.

cm^{-1}, an additional vibration appears at ≈ 13 cm^{-1}. This is evidenced by the double peak structure observed as a broad band in Fig. 7.9.

To understand this result, we must remember the morphology of the sample produced with $N = 50$. Figure 7.10 shows a cross-section TEM image of that sample. A careful inspection of the NCls shows two important features. We observe discontinuities in certain NCls, while others present a clear misalignment. The discontinuities, about 1 nm, lead to NCls with different heights. However this fact has no effect on the Raman spectra. We must also remember that vibrations are confined in the NCls volume. Thus a modification of the volume should induce a shift of the vibration frequency. However, the

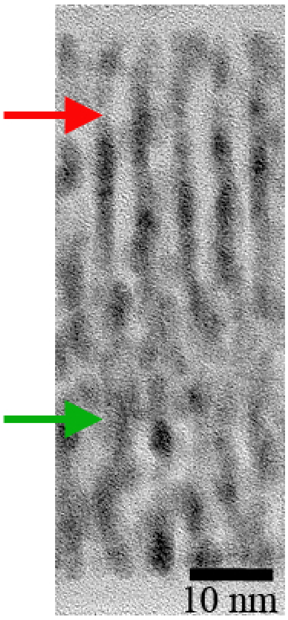

Figure 7.10: Cross-section TEM image of the sample $N = 50$. The red arrow shows discontinuities while the green one shows misalignment of NCLs.

volume changes are due to a variation of H, but the experimental Raman configuration used is only sensitive to changes of D. Thus the the band around 13 cm^{-1} should not be due to the discontinuities.

On the contrary the misalignement of the NCls (red arrow in Fig. 7.10) leads to "connecting zones" that have effective D in the range of 3 nm to 4 nm that should be detected. This is in good agreement with the fact that using the simple model of Lamb, we can calculate roughly that the vibration frequencies associated to this range of diameters should occur at ≈ 12 cm^{-1}. However, this question is still under investigation at the time of writing this thesis.

The second way to modify the aspect ratio of the NCls is to vary X while maintaining the amount of Ag and the number of cycles constant. Figure 7.11 presents the extinction spectra of three samples having decreasing a-Al_2O_3 deposition times, t_{Al2O3} of 50 seconds (X_{50}), 30 seconds (X_{30}), and 25 seconds (X_{25}), N =10 and D= 2.2 ± 0.2 nm. For X_{50} only one broad peak is observed in the extinction spectra. This indicates that the NPs layers are well separated (one peak) although close enough to interact (broad peak). When t_{Al2O3} is reduced, two peaks appear in the extinction spectra, which evidences the formation of NCls. From the deposition rate determined in Chapter 2 we have estimated the X values X_{cal}. They are summarized in table 7.4 together with the wavelengths of

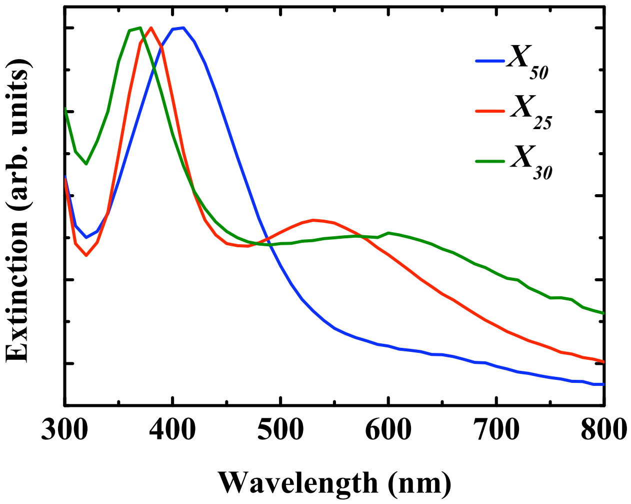

Figure 7.11: Experimental extinction spectra of samples containing Ag NCls produced with decreasing X, recorded using p-polarized light and an angle of incidence of 65°

.

the SPRs. We recall that X is defined as the thickness of a-Al_2O_3 deposited among the space between NPs, i.e. the thickness of the nanocomposite layer, plus the thickness (T_{cover}) of the a-Al_2O_3 deposited further, defined as $T_{cover} = X\text{-}D$. For X_{50}, a thin a-Al_2O_3 layer of thickness $T_{cover} = 1.6$ nm covers the nanocomposite. The consecutive layers of Ag NPs are physically well separated as suggested by the extinction spectrum shown in Fig. 7.11.

Sample name	$t_{Al_2O_3}$	X_{cal} (nm)	$\lambda(SPR_T)$ (nm)	$\lambda(SPR_L)$ (nm)
X_{50}	50	3.8	405	405
X_{30}	30	2.7	363	610
X_{25}	25	2.5	380	540

Table 7.4: Experimental wavelengths of the SPRs as a function of the Al_2O_3 deposition time. The values X_{cal} are determined using the deposition rates.

When X decreases, the consecutive NPs layers start to “connect” forming the NCls. This is confirmed by the appearance of transverse and longitudinal SPRs in the extinction spectra (Fig. 7.11). However, the thickness T_{cover} of a-Al_2O_3 deposited between consecutive NPs layers should be 0.5 and 0.3 nm, for 30 sec and 25 sec, respectively.

These values of T$_{cover}$ could be due to an error in the determination of X or related to the amount of material re-sputtered during deposition of Ag or a-Al$_2$O$_3$.? Cross-section images of these samples confirm the formation of NCls as shown in Fig. 7.12. In addition, NCls embedded in sample X_{25} (H_{25} = 11.2 ± 0.2) are shorter than those embedded in X_{30} (H_{30} = 13.4 ± 0.2). This is confirmed by the extinction spectra since the splitting of the transverse and longitudinal mode is larger in the latter case ($\Delta\lambda_{25}$ = 160 nm < $\Delta\lambda_{30}$ = 247 nm).

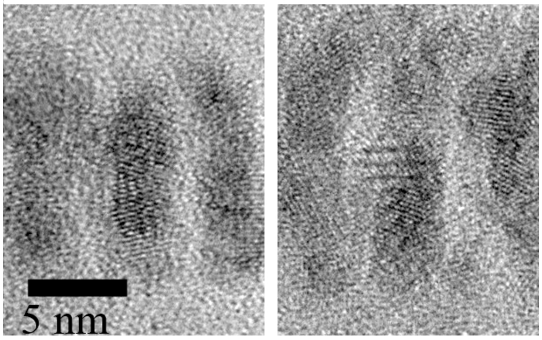

Figure 7.12: Cross-section TEM images of NCls thin films produced with (left) X_{25} and (rigth) X_{30}.

Figure 7.13 is a scheme of the proposed morphology of the NCls as a function of X. In the case X_{25}, consecutive NPs layers overlap while they simply connect for X_{30}. Thus, the latter leads to higher NCls. The pattern (first layer of NPs) as well as the quantity of metal deposited is similar in both cases. Thus, the diameter of the NCls for X_{25} should be larger, and the in-plane surface to surface distance between two NCl should be smaller than in the case of X_{30}.

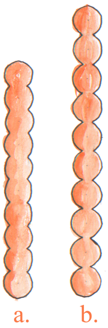

Figure 7.13: Proposed morphology for NCls produced with (a) X_{25} = 2.5 nm and (b) X_{30} = 2.7 nm.

For X_{25} we must have then a change of diameter that should be observed in the Raman spectra. Fig. 7.14 presents the stokes Raman spectra of the three nanocomposites. The frequencies of the observed peaks and the average diameter calculated using Lamb's model* are summarized in table 7.5.

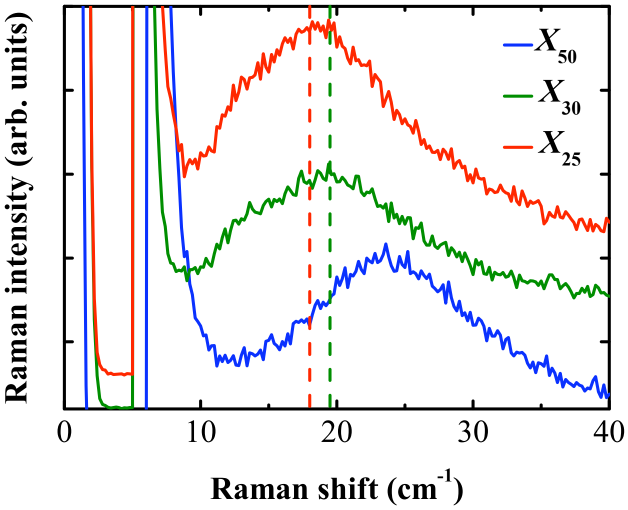

Figure 7.14: Experimental Stokes Raman spectra of samples containing Ag NCls produced with decreasing X. The incident laser beam was p-polarized and the polarization of the scattered light was not analyzed. Dashed lines are only guides for the eyes.

Sample name	ω (cm^{-1})	$D_{cal}(nm)$
$\boldsymbol{X_{50}}$	24.0 ± 1	2.1 ± 0.5
$\boldsymbol{X_{30}}$	19.5 ± 1	2.6 ± 0.5
$\boldsymbol{X_{25}}$	18.0 ± 1	2.8 ± 0.5

Table 7.5: Experimental frequencies of the Raman bands as a function of the Al_2O_3 deposition time.

For X_{50}, the Raman spectrum shows the typical vibration peak due to the quadrupolar vibration mode of a spherical NP, for which D_{cal} agrees well with the expected diameter. When X is small enough to nucleate NCls, the peaks shifts to lower frequencies

---

[*] We consider NPs with the same diameter as the NCl

indicating that the diameter has slightly increased for the shortest values of X. Moreover, the small variation of ω demonstrates that the diameter slightly increases for the shortest value of X.

In this section we have shown that the splitting of transverse and longitudinal SPRs is smaller when N increases than when X decreases. This is due to the small changes observed in the NCls diameter, as shown by the Raman measurements. Thus, the variation of the in-plane NCls surface to surface distance must be taken into account. This factor can affect the optical response of the nanocomposites as described in the next section.

7.3.2 Real morphology: from theory to experiment

Up to now, we have considered that the NCls are perfect prolate ellipsoids oriented along the same direction. However, section 7.3.1 has shown that we must take into account that while NSs and NLs nucleate in a one-step process, the NCls can be considered as a stack of NSs, more or less overlapped, which nucleate in a multiple step process that leads to the formation of a kind of "nanonut" (NN) (Fig. 7.13), rather than a NCl. The formation of one or another type of nanostructure is relevant since it may affect the characteristic morphological parameters that determine the SPR.

Figure 7.15 shows the experimental extinction spectrum of a sample having NCls produced with 10 cycles and having D and H values of 2.3 ± 0.2 nm and 10.5 ± 0.3 nm, respectively. We clearly observe a splitting of the transverse and longitudinal SPRs peaking at 390 and 535 nm, respectively. We have calculated the optical extinction spectra using the average values of D and H in order to correlate the measured SPR wavelengths to the aspect ratio of the NCls. In a first approximation we have assumed that the NCls are prolate spheroids and we have considered Gans model for an isolated prolate NP. The simulated spectrum is included in Fig. 7.15. It predicts a longitudinal SPR at 900 nm, which is red-shifted by 365 nm with respect to the experimental value.

Alternatively, we have considered a NN structure formed by a stack of 5 NPs of diameter D slightly overlapped and a total height H using the discrete dipole approximation.* Figure 7.16 illustrates the NNs morphology. The optical extinction spectra obtained by this method is also included in Fig. 7.15. The longitudinal SPR now appears at 750 nm, whereas the transverse SPR is at 378 nm, both values being closer to

---

*Simulations made by A. Arbouet, CEMES, France

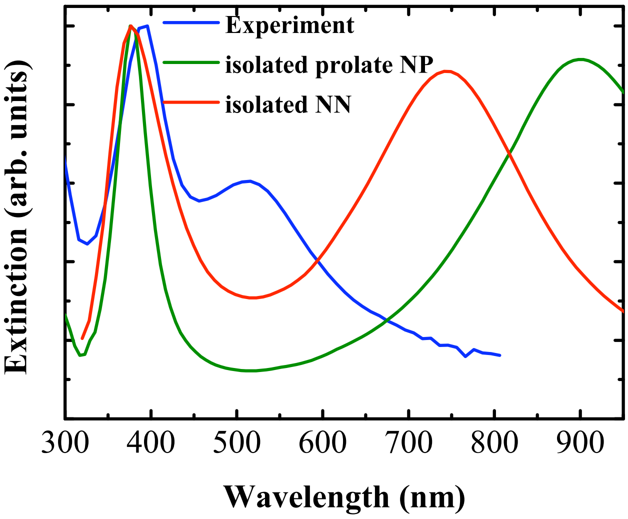

Figure 7.15: Experimental extinction spectrum recorded using p-polarized light and an angle of incidence of 65°. Theoretical extinction spectra are calculated for an isolated prolate NCls (Gans model) and an isolated NN (DDSCAT).

experimental values than the ones obtained with Gans model. However, there is still a huge discrepancy between experimental and calculated extinction spectra. Nevertheless, these results indicate that the NCls may be closer to NNs than to prolate ellipsoids.

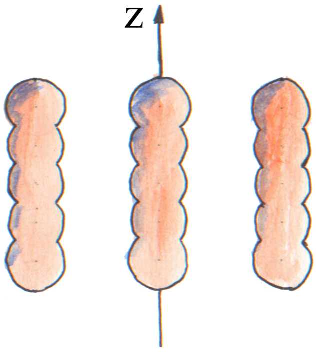

Figure 7.16: Schematic of the NNs shape (cross-section) used for DDSCAT calculations.

In order to evaluate the effect of the high NCls number density we have calculated extinction spectra using Maxwell-Garnet model for prolate ellipsoids having D= 2.3±0.2

nm and $H = 10.5 \pm 0.3$ nm and a NCl number density of 7.8×10^{12} NCls/cm^2, which corresponds to a volume fraction of $f \simeq 30\%$.

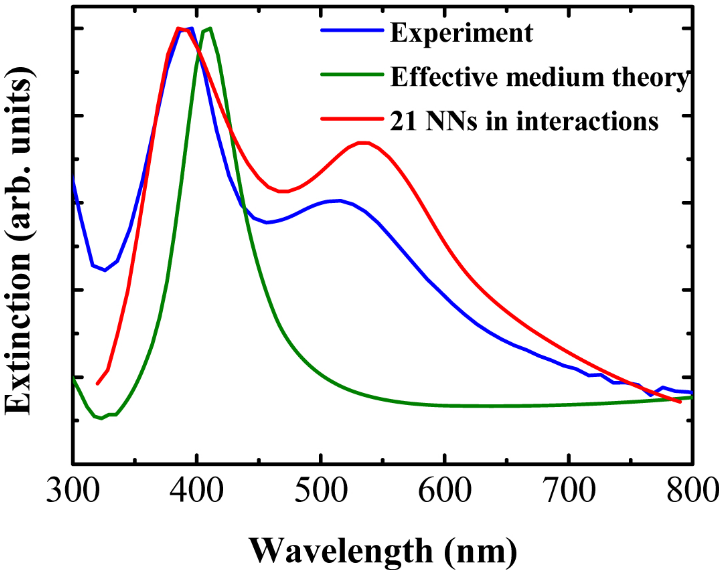

Figure 7.17: Experimental extinction spectra of Ag NCls (blue), recorded using p-polarized light and an angle of incidence of 65°. Green and red curves, respectively, show the spectra calculated using Maxwell-Garnett model, adapted to prolate NPs, and DDSCAT considering 21 NNs.

The calculated spectra is shown in Fig. 7.17 where the experimental spectrum is also included for comparison. The transverse SPR wavelength is slightly red-shifted with respect to the experimental longitudinal SPR wavelength.

Finally, we have considered the interaction between NNs within the discrete dipole approximation. This has been performed by considering 21 NNs (Fig. 7.16) separated by 3 nm (average separation surface to surface observed by TEM) and organized according the scheme shown in Fig. 7.18. We had to restrict the simulation to 21 NNs only, due to computer limitations. Extinction spectra have been calculated using DDSCAT? numerical software averaging among 10 different orientations to take into account that there is no two dimensional organization.* The results obtained are also shown in Fig. 7.17. The longitudinal SPR now appears at 535 nm and the transverse SPR at 390 nm, both in very good agreement with the experimental values. This confirms that the samples must be considered as formed by NNs with a high number density. Both, the NN shape and the interaction between neighbour NNs are responsible for the blue shift of the longitudinal SPR with respect to the case of isolated prolate ellipsoids.

---

*Simulations made by A. Arbouet, CEMES, France

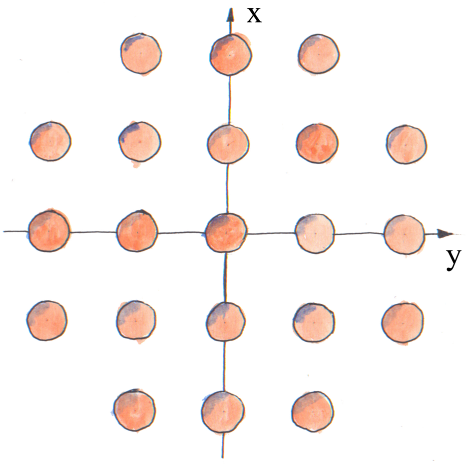

Figure 7.18: Schematic of the NNs distribution (plan-view) used for DDSCAT calculations.

8

Coupling between surface plasmons and confined acoustic vibrations

In this chapter we focus on the coupling between surface plasmons and confined acoustic vibrations in systems containing a single type of NPs such as the Ag NCls, or two types of NPs: Ag and Co NPs.

8.1 Nanocolumns

Chapter 7 has demonstrated that acoustic vibrations and SPRs are related to the size and shape of NPs. Moreover in section 7.1 we have observed that the vibration frequency of a spherical NP is related to the excitation wavelength. This behavior is due to both inhomogenous broadening of the Raman band and to the different size dependence of the resonant and non-resonant Raman scattering efficiencies mediated by SP.[?] In the following we study the coupling between surface plasmons and acoustic vibrations of silver NCls.[?,?]

Figure 8.1 shows the extinction spectrum for a sample containing NCls with aspect ratio 2.5 (Fig. 3.9 a.) together with the frequency of the maximum of the Raman bands as a function of the excitation wavelength. The laser beam, used to excite the Raman scattering, was always p-polarized, and the scattered light was not analyzed. The extinction spectrum shows the expected splitting of the transverse and longitudinal modes of the SPR already discussed in Chapter 7.

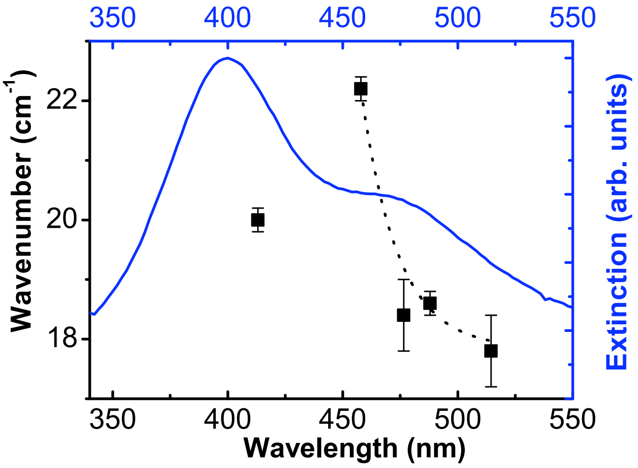

Figure 8.1: (Filled squares) Experimental frequencies of the vibrations of the NCls versus excitation wavelength. The laser beam was p-polarized, and the polarization of the scattered light was not analyzed. The dotted line is a guide to the eye. (blue) Experimental extinction spectrum of the NCls, recorded using p-polarized light and an angle of incidence of 65°.

The frequencies of the maximum of the vibration peaks are ≈18 cm^{-1} for excitation wavelengths that are away from the maximum of the longitudinal SPR, while a shift of the Raman bands to higher frequencies ($\Delta\omega \approx 4$ cm^{-1}) is observed when the excitation approaches the longitudinal SPR. At these wavelengths we excite the longitudinal SP associated to the oscillation of the electrons along the long axis of the NCls, and generate a polarization, P_{SPR}, along it. Meanwhile, the confined acoustic quadrupolar vibration mode ($l = 2$, $m = \pm\, 2$, $n = 0$) of the NCls induces a displacement of the surface charges. The SP and the vibration interact generating a polarization vector with two components along the long and short axis of the NCls. The latter is responsible for the observation of the vibration peak in the Raman spectra. As we approach the resonance with the longitudinal SPR, the coupling between longitudinal SP and vibrations increases. When exciting the NCls with the 413 nm line (i.e. close to the transverse SPR) the Raman peak appears at 20 cm^{-1}, due to the possible coupling of the transverse SP.

In order to further investigate the interactions between SP modes and confined acoustic vibrations, we have recorded the Raman spectra for various incident and scattered light polarizations. We have used the 488 nm line of the Argon laser to excite the NCls close to the resonance with the longitudinal SPR. Figure 8.2 shows the Raman signal as a function of the polarization of the incident and the scattered light. The inset in Fig. 8.2 shows the evolution of the Raman intensity as a function of the incident polarization angle from p- (0 degree) to s- (90 degrees) polarizations. The measured intensity has been normalized to that of the optical phonon of the silicon substrate. In that way, the Raman intensity changes are only due to the coupling with the SP.

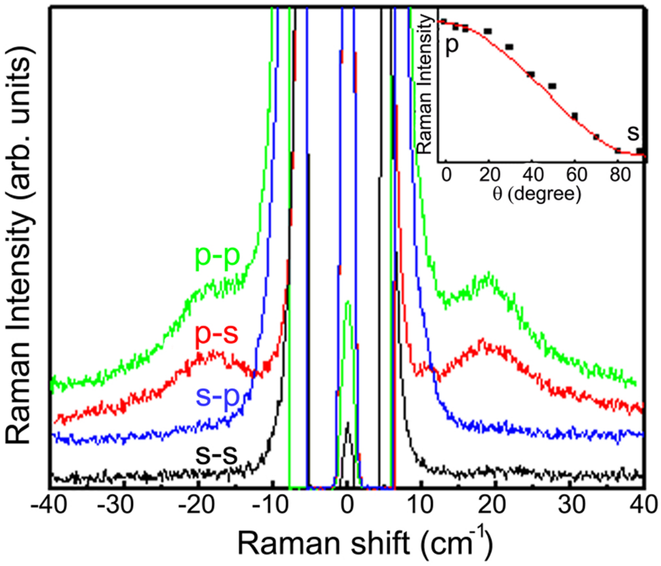

Figure 8.2: Experimental Raman spectra of samples containing NCls excited at 488 nm and using different polarizations. "s-p" stands for (s) and (p) incident and scattered polarizations, respectively. The inset shows the intensity variation of the low-frequency Raman band versus excitation polarization angle (from p to s) normalized with respect to that of the optical phonon of silicon. The continous line is an empirical $cos^2(\theta)$ fit.

The scattered intensity varies as $cos^2(\theta)$ which means that the vibration intensity is maximum when the intensity of the electric field along the long axis of the NCl is maximum. In addition, the vibration is observable only when the incident light is p-polarized irrespective of the polarization of the scattered light. This means that the

Raman band is observable only when the longitudinal SP is excited.

Moreover, in our experimental conditions the detected electric field is always along the plane perpendicular to the major axis of the NCls (Chapter 6), and thus, is perpendicular to the field generated by the longitudinal SP. Therefore, since the NCls have symmetry of revolution around their long-axis, the scattered intensity should be the same in both p-p and p-s configurations as observed experimentally in Fig. 8.2. The longitudinal SP excitation must be transfered to the short axis of the NCls through its interaction with the quadrupolar vibrations. As a consequence, the transverse SP is excited and we can conclude that surface plasmons excitations act as intermediate collective electronic state, which contributes to the recorded Raman response. Instead, when the transverse SP is directly excited, the field perpendicular to the long axis of the NCls, generated by the SP and modulated by the quadrupolar vibration, is directly detected, and a vibration band appears in the Raman spectrum.

8.2 Surface Plasmon-Acoustic Vibration interaction in Co-Ag bilayers

In this section we study the vibrational response of the Co-Ag bilayers described in Chapter 3 and whose cross-section TEM image was shown in Fig. 3.3. The scheme of the samples structure is reminded in Fig. 8.3. The samples are composed of spherical Co NPs ($\boldsymbol{D}_{Co}$ = 2.7 ± 0.4) and Ag NLs ($\boldsymbol{D}_{Ag}$ = 10 ± 2, $\boldsymbol{H}_{Ag}$ = 6.0 ± 0.5). The average in-depth vertical spacing between Co and Ag NPs is $\boldsymbol{X}$=4, 6 or 8 nm within each bilayer, while the separation between consecutive Co-Ag bilayers is fixed to 25 nm. Samples containing only Co NPs or Ag NLs with the same dimensions are also studied for comparison.

In the case of Co NPs, the SPR is located in the near UV, while that of Ag NPs lies in the blue region of the visible spectrum. The inset of Fig. 8.4 shows the SPR of Co NPs and Ag NPs embedded in a-Al_2O_3, calculated using Mie's theory. As shown the SP of Co NPs is not excited by the 488 nm laser line. Thus the vibrations of Co NPs should not be observed in the Raman spectra. Instead, the SP of Ag NLs is excited and therefore the vibrations of Ag NLs are expected in the Raman spectra.

The Raman spectra of samples containing only Co NPs or Ag NPs layers are presented in Fig. 8.4. As expected, the featureless spectrum corresponds to the sample containing

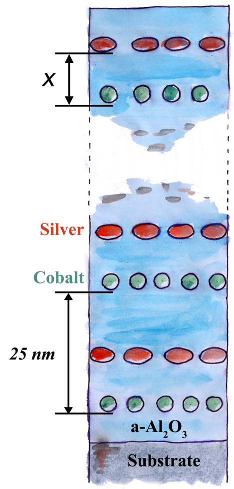

Figure 8.3: Schematic of the Co-Ag bi-layers nanostructures

only Co NPs, whereas a vibration band at ≈ 8 cm^{-1} is observed in the case of the sample containing only Ag NPs. As discussed in the previous sections, this vibration mode corresponds to the quadrupolar vibration of Ag NLs having characteristics sizes of $\boldsymbol{D}_{Ag} = 10 \pm 2$ and $\boldsymbol{H}_{Ag} = 6.0 \pm 0.5$. Thus, Raman scattering from Co NPs should not be expected from Co-Ag bilayer samples.

The Raman spectra of Co-Ag NPs bilayers are also presented in Fig. 8.4 for decreasing in-depth spacings, $\boldsymbol{X}$. Two bands are clearly observed for $\boldsymbol{X} = 4$ and 6 nm. The low frequency band at 8 cm^{-1} is due to the Ag NPs while the broader band at ∼ 28 cm^{-1} is neither observed in samples containing only Ag nor only Co NPs. This band is not resolved for $\boldsymbol{X} = 8$ nm, although it appears as a shoulder on the high energy tail of the Raman signal due to the Ag NPs.

In order to determine the origin of the Raman band at ≈ 28 cm^{-1} we have calculated the acoustic vibration frequencies of each type of NPs. We have used the resonant ultra-sound (RUS) simulation method introduced by Visscher et al.[?,?,?] to calculate the NPs vibration frequencies.[*] The eigenfrequencies (and associated displacements) of the NPs have been calculated in the frame of the continuum elastic approximation using the "xyz algorithm".[†] This method allows determining the acoustic vibrations whatever the shape of the NPs, which is particularly relevant for the case of our Ag NLs. Taking into account the effect of the matrix, the model predicts that the fivefold degenerate

---

[*] simulations made by L. Saviot, Université Carnot de Bourgogne (France), and D. Murray, University of British Columbia (Canada)

[†] A detailled description of this algorithm is out of the scope of this work.

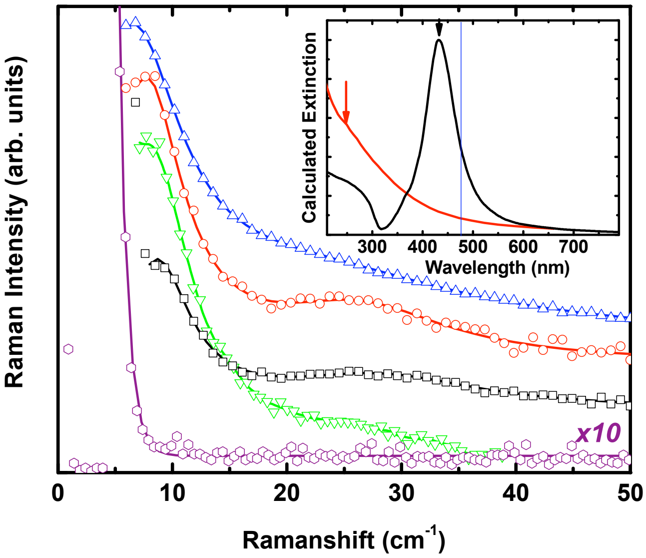

Figure 8.4: Experimental Stokes Raman spectra of samples containing Co-Ag bilayers excited at 488 nm. The incident beam was p-polarized and the polarization of the scattered light was not analyzed. (purple) Samples containing Co NPs or (green) oblate Ag NPs monolayers and samples containing Co-Ag bilayers spaced (black) $\boldsymbol{X}= 4$ nm, (red) $\boldsymbol{X}= 6$ nm, and (blue) $\boldsymbol{X}= 8$ nm are included. Solid lines are guides for the eyes. The inset shows the wavelength of SPRs of Co and Ag NPs embedded in a-Al_2O_3 calculated using Mie theory. The vertical blue line in the inset corresponds to the Raman excitation wavelength (488 nm).

quadrupolar vibration modes ($l = 2$; $m = 0, \pm1, \pm2$; $n = 0$) split into three different frequencies associated to spheroid-like modes when the aspect ratio becomes smaller than 1 as in the present case: 7.1 cm^{-1} (two fold degenerate), 8.3 cm^{-1} (non-degenerate) and 8.4 cm^{-1} (two fold degenerate). These frequencies are in agreement with the frequency of the measured Raman band at 8 cm^{-1}. The other vibration mode of the Ag NLs theoretically observable is the breathing mode ($l = 0$; $m = 0$; $n = 0$) whose frequency is found at 15.0 cm^{-1}. However the coupling of this vibration mode with the SP is much less efficient, and thus the Raman band corresponding to this vibration is not observed in the spectra. This calculation is consistent with the fact that only the quadrupolar vibration is visible in the spectrum of the sample containing Ag NLs layers only. Thus, the vibration responsible for the appearance of the Raman band at $\approx$28.0 cm^{-1} appears to be due to the Co NPs.

In a first step, we have estimated the vibration frequency of Co NPs using Lamb's model. In the case of spherical Co NPs of diameter, $\boldsymbol{D}_{Co}$ = 2.7 ± 0.4 (nm) and using the transverse sound velocity in Co at 295 K (2886 $m.s^{-1}$)[?] (Chapter 4) we found the vibration frequency of the quadrupolar mode at $\approx$ 30 cm^{-1}. This value has been confirmed using the RUS simulation code. We obtain 29.0 cm^{-1} for the vibration frequency of the quadrupolar vibration mode of a free standing spherical Co NP. Thus, calculations indicate that the Raman band observed at $\approx$28.0 cm^{-1} is most likely due to the vibration of Co NPs.[?] However, since the SP of Co NPs is not directly excited by the laser beam,[?] other mechanisms should explain the presence of this band.

A possible explanation for the observation of the Co NPs vibrations could be their coupling with the electric field generated by the SP of the Ag NLs. Indeed, the Ag SP near field expands out of the NL into the matrix. Thus if the Co NP is close enough to the Ag NL, the Co NP quadrupolar vibrations interact with the SP allowing the observation of its vibration band in the Raman spectra. This coupling between the Co NP confined acoustic vibrations and the Ag NL SP is related to the modulation of the surface charges due to NP vibrations, therefore it is important to investigate the distribution of the surrounding electric field generated by the Ag SP. Figure 8.5 shows the electric field pattern, calculated using the Finite Difference Time Domain CST software[*] and considering Ag NL and spherical Co NPs with the real size and shape of the samples studied, $\boldsymbol{X}$ fixed to = 4 nm. The calculation considers that the electric field is generated by a monochromic wave at 488 nm with an angle of incidence of 65° with respect to the normal of the sample surface, which corresponds to the experimental conditions used. The electric fields for $\boldsymbol{X}$= 6 nm, 8 nm and 10 nm have also been calculated but are not shown in the figure.

The electric field at the Co NP surface is very weak (Fig. 8.5(a)) since the SP of the Co NP is not directly excited by the incident laser beam contrary to that of the Ag NL. The presence of the Co NP in the near field of the Ag NL (Fig. 8.5(b)) has a strong impact on the electric field distribution.[?,?] A hot spot characteristic of the electric field enhancement emerges in the region between the Ag and Co NPs for $\boldsymbol{X}$= 4 nm. Moreover, the electric field in the vicinity of the Co NP surface, increases by an order of magnitude when $\boldsymbol{X}$ decreases from 12 to 4 nm. According to the electromagnetic theory of surface enhanced Raman scattering, this enhancement factor should lead to a factor $\approx$ 10000 in the Raman scattering intensity due to the photon absorption and emission events.

---

[*] Calculation made at the DSI in Singapore

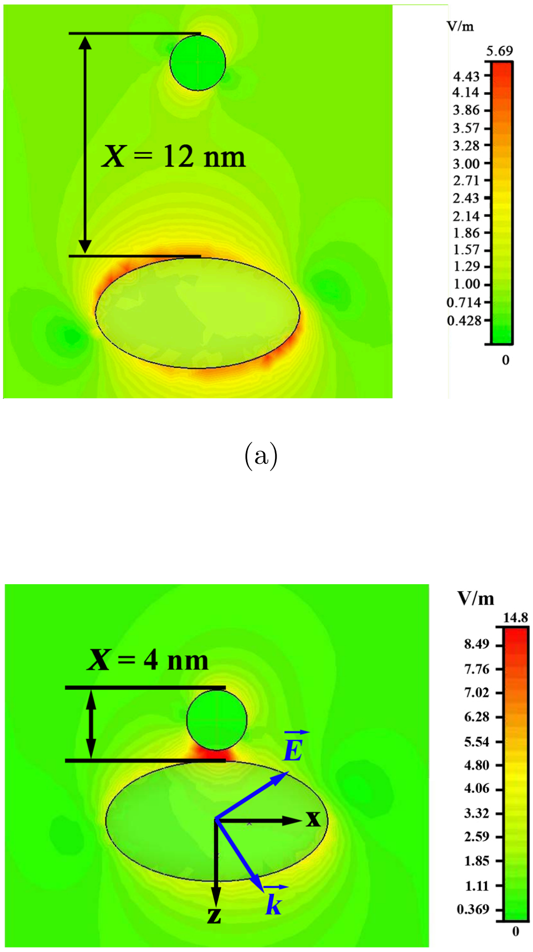

(a)

(b)

Figure 8.5: False color distribution of the electric field generated by Ag SP in the vicinity of an oblate Ag NP with a neighbour Co NP at a distance ***X*** of (a) 12 nm and (b) 4 nm. Note that the scales are different.

Therefore, combination of Raman experiments and modeling allows us to conclude that the coupling between the Co NP quadrupolar vibrations and the Ag NL SP effectively occurs. The Ag NL SP generates polarization charges at the surface of the Co NPs that are modulated by the quadrupolar vibrations, which are detected in the Raman spectra.

Part V

General conclusion

The main conclusion of this thesis is that the production of Ag **nanostructures with well defined morphology** using PLD is feasible. **Nanospheres**, **nanolentils** (oblate ellipsoids) and oriented **nanocolumns** (prolate ellipsoids) embedded in amorphous Al_2O_3 have been produced using alternate pulsed laser deposition. The effect of the deposition parameters on the morphological characteristics of the nanoparticles (size, aspect ratio, concentration) has been determined, and this has made finally possible the study of the relationships between nanoparticles morphology and optical properties of the thin film nanostructures, as well as the analysis of the interaction between surface plasmons and confined acoustic vibrations.

Standard a-PLD allowed us to produce $Ag{:}Al_2O_3$ nanostructures consisting of consecutive layers of Ag nanoparticles separated by layers of amorphous Al_2O_3. Using this approach we have synthesized **nanospheres** and **nanolentils**. We have found that their number density and diameter can be controlled by varying the amount of metal deposited. Below a certain threshold that depends on the metal type ($8{\times}10^{15}$ atoms cm^{-2} in the case of Ag), nanoparticles are spherical, well separated and present a sharp size distribution. Above this threshold, nanoparticles start to coalesce in the plane which leads to the formation of oblate spheroid nanoparticles, i.e. **nanolentils** with typical sizes $D=$ 10 nm and $H=$ 6 nm. However, coalescence is a random process and, as a consequence, the degree of control over the morphological parameters and organization of the nanostructures is dramatically reduced.

In order to achieve a good control over the morphological parameters of the nanostructures we have developed a **new deposition route** that takes advantage of coalescence to produce self-oriented **nanocolumns**. The approach is based on the reduction of the in-depth separation between consecutive layers of Ag **nanospheres** embedded in a-Al_2O_3. We have demonstrated the production of **nanocolumns** when the in-depth separation is close to the diameter of the Ag **nanospheres** (typical size 2.7 nm). The number density, and diameter of the **nanocolumns** can be controlled through the amount of metal deposited in the first metal layer, while the amount of metal deposited in subsequent cycles, the number of cycles and finally, the amount of a-Al_2O_3 deposited after each layer of metal NPs determines the height of the **nanocolumns**. These results open new possibilities for material nano-design since they provide a simple route based on a single step process at room temperature to produce, **nanolentils** and **nanocolumns** with diameters typically <10 nm and with low size and shape dispersion, features that are not easily accessible for other techniques.

The linear **optical response** of the different types of nanostructures has been characterized and we have reported the relationship between surface plasmon resonance and the morphology of Ag nanoparticles. The splitting of the surface plasmon resonance into longitudinal and transverse modes has been observed when the spherical symmetry is broken. As predicted theoretically, the transverse surface plasmon resonance is shifted into the red and the longitudinal surface plasmon resonance into the blue when the aspect ratio is smaller than 1 (**nanolentils**), while the opposite behavior is observed when the aspect ratio is higher than 1 (**nanocolumns**).

Optical analysis has confirmed that the **nanocolumns** are self-oriented perpendicularly to the substrate surface, and it has been shown that the shift of the longitudinal surface plasmon resonance into the red is limited to a maximum value. **Numerical simulation** of the extinction spectra using different models (Gans, Maxwell-Garnett, DDSCAT) has shown that this behaviour is caused by the existence of **electromagnetic interaction** among **nanocolumns**, which demonstrates the importance of the number density of **nanocolumns** on the optical response of the nanostructures. Finally, these simulations also suggest that **nanocolumns** must be considered as an aggregation of contacting **nanospheres** ordered along the direction perpendicular to the substrate surface (nanonuts) rather than a single structure (prolate ellpsoids, or cylinders).

Low frequency Raman scattering has allowed studying the confined acoustic vibrations of the nanostructures embedded in the amorphous host. The vibration bands observed in the spectra are due to the quadrupolar acoustic vibration mode that is mainly dominated by size effects, namely by the average in-plane diameter. The availability of nanostructured thin films having NPs with well defined morphology and orientation has made possible to investigate in detail the effect of the nanoparticle shape on the **vibrational response**. In the case of **nanospheres** the quadrupolar mode is fivefold degenerated. This degeneracy partially disappears when the spherical symmetry is broken. The combination of experimental Raman analysis with numerical simulations performed using molecular dynamics and resonant ultrasound calculations has made possible to identify the folds observed in each case. For aspect ratios smaller than 1 (**nanolentils**) the active modes observed correspond to the threefold degenerate spheroidal modes ($l = 2$; $m = 0, \pm 1$; $n = 0$). On the contrary, the twofold degenerate spheroidal modes ($l = 2$; $m = \pm 2$; $n = 0$) are observed in the case of **nanocolumns**. Finally, we have identified that the Raman scattering acoustic vibrations signal is enhanced by the interaction between the longitudinal surface plasmon mode and the vibrational spheroidal modes: the polarization generated by the surface plasmon is modulated by the quadrupolar vibrational mode.

The work has been completed by expanding the nano-design approach to **complex nanostructures** containing nanoparticles of different metals. In particular, we have produced samples containing alternate layers of **Co nanospheres** and **Ag nanolentils**, in which we have controlled the separation between these layers in the range from 4 nm to 8 nm. We have demonstrated the existence of **interaction between surface plasmons and confined acoustic vibrations** of nanoparticles of different metals. Namely we have excited the acoustic vibrations of Co nanoparticles by embedding them into the near field region of Ag **nanolentils**. In this case numerical modelling shows that the intensity of the electric field near the surfaces of Ag **nanolentils** and Co nanoparticles is strongly enhanced for separations of few nanometers ($\leq$ 6 nm) and for excitation wavelengths close to that of the surface plasmon resonance of Ag **nanolentils**. This interaction promotes the Raman scattering by the confined acoustic vibrations of Co nanoparticles. This prediction has been confirmed experimentally.

Conclusiones

La principal conclusión de esta tesis es que es posible sintetizar nanoestructuras de Ag con una morfología bien definida mediante depósito por láser pulsado. Para ello, se ha desarrollado un procedimiento que permite producir nanoesferas, "nanolentils" (elipsoides oblatos), y nanocolumnas (elipsoides prolatos) auto-ensambladas inmersas en a-Al_2O_3 y orientadas. Se ha determinado cómo afectan las condiciones experimentales de síntesis a las características morfológicas de las nanocolumnas y se ha establecido asimismo en qué condiciones es posible maximizar la relacién de aspecto (altura/dimetro).

Se ha correlacionado la respuesta óptica lineal de las diferentes nanoestructuras con su morfología y se ha simulado la respuesta óptica utilizando diferentes modelos (Gans, Maxwell-Garnett, DDSCAT). Dicho estudio ha confirmado el carácter orientado de las nanocolumnas, demostrándose que su respuesta depende de la polarización del haz incidente. En el caso de la nanopartículas no esféricas se observan las resonancias de los modos transversal y longitudinal del plasmon de superficie. Ambas resonancias se desplazan espectralmente en función de la relación de aspecto de las nanopartículas.

Se ha analizado la respuesta vibracional de las nanoestructuras producidas mediante dispersión Raman de baja frecuencia, determinándose que los modos vibracionales activos son los cuadrupolares. Se ha estudiado en detalle el efecto de la forma de las nanopartículas en la respuesta vibracional. En el caso de nanoesferas el modo cuadrupolar está múltiplemente degenerado. La combinación de los resultados experimentales con simulaciones numéricas basadas en dinámica molecular y cálculos de ultrasonidos resonantes ha hecho posible determinar cómo se rompe la degeneración en cada caso: Para relaciones de aspecto menores a 1 (nanolentils) los modos observados corresponden a los modos esferoidales: $l = 2$; $m = 0, \pm 1$; $n = 0$, mientras que para las nanocolumnas, cuya relación de aspecto es mayor que 1, los modos observados son: $l = 2$; $m = \pm 2$; $n = 0$.

Por último, el trabajo desarrollado ha permitido concluir que la señal Raman es activada por la interacción entre el plasmon de superfice de las nanolentils de Ag y los modos vibracionales de las nanoparticulas de Co. Se ha observado cómo excitando el sistema a una longitud de onda próxima a la de la resonancia del plasmon de superficie de las nanolentils de Ag, es posible activar modos de vibración en las nanopartículas de Co. Este comportamiento se ha relacionado con un aumento intenso del campo eléctrico en las proximidades de la superficie de las nanopartículas de Ag y Co, que es predicho por la modelización efectuada.

Conclusions

La conclusion principale de cette thèse est qu'il est possible de synthétiser des nanostructures d'Ag avec une morphologie bien définie en utilisant la méthode de dépôt par ablation laser pulsé. Pour cela, nous avons développé une procédure qui permet de produire des nanosphères, des nanolentilles (ellipsoïdes oblates), et des nanocolonnes (ellipsoïdes prolates) auto-assemblés, orientées et encapsulées dans une matrice d'a-Al_2O_3. Nous avons démontré comment les conditions expérimentales de synthèse affectent les caractéristiques morphologiques des nanocolonnes, et nous avons pu déterminer ainsi quelles sont les conditions optimum pour maximiser la rapport d'aspect (hauteur/diamètre).

Nous avons corrélé la réponse optique linéaire des différentes nanostructures avec leur morphologies, et nous avons simulé la réponse optique en utilisant différent modèles (Gans, Maxwell-Garnett, DDSCAT). Cette étude a confirmé l'orientation des nanocolonnes, en démontrant que leur réponse dépend de la polarisation du faisceau incident. Dans le cas de nanoparticules non-sphériques on observe les résonances des modes transverse et longitudinal du plasmon de surface.

Nous avons aussi analysé la réponse vibrationnelle des nanostructures produites en utilisant la spectrométrie Raman basse fréquence, grâce à laquelle nous avons pu déterminer que les modes actifs de vibration sont les modes quadrupolaires. Nous avons étudié en détail l'effet de la forme des nanoparticules sur la réponse vibrationnelle. La combinaison des résultats expérimentaux et des simulations numériques basées sur la dynamique moléculaire et les calculs d'"ultrasons résonants" a permis de déterminer comment se lève la dégénérescence dans chacun des cas: Pour des rapports d'aspect inférieure à 1 (nanolentils) les modes observés correspondent aux modes sphéroïdaux: $l = 2$; $m = 0, \pm 1$; $n = 0$, alors que pour les nanocolonnes, cette rapport d'aspect est supérieur à 1, les modes observés sont: $l = 2$; $m = \pm 2$; $n = 0$.

Pour finir, le travail développé a permis de conclure que le signal Raman est activé par l'interaction entre le plasmon de surface des nanolentilles d'Ag, et les modes de vibration des nanoparticules de Co. Lorsque le système est excité à une longueur d'onde proche de la résonance du plasmon de surface des nanolentilles d'Ag, il est possible d'activer les modes de vibration dans les nanoparticules de Co. L'importante augmentation du champ électrique au voisinage de la surface des nanoparticules d'Ag et de Co, qui a également été observé dans les simulations, est responsable de l'observation de la vibration des nanoparticules de Co.

Bibliography

[1] R. P. Feynman. There's plenty of room at the bottom. *Microelectromechanical Systems, Journal of*, 1(1):60–66, 1992.

[2] G. Mie. Beiträge zur optik trüber medien, speziell kolloidaler metallösungen. *Annalen der Physik*, 330:377–445, 1908.

[3] A. Hilger, M. Tenfelde, and U. Kreibig. Silver nanoparticles deposited on dielectric surfaces. *Applied Physics B: Lasers and Optics*, 73(4):361–372, 2001.

[4] N. Taniguchi. On the basic concept of nanotechnology. In *Proc. Intl. Conf. Prod. London, Part II, British Society of Precision Engineering*, 1974.

[5] *Nanotech: The science of small get down to business*, volume 284. Sci. Am., september special issue 2001.

[6] K. E. Drexler. *Nanosystems: Molecular Machinery, Manufacturing, and Computation.* John Wiley & Sons, 1992.

[7] C. L. Haynes and R. P. Van Duyne. Nanosphere lithography: A versatile nanofabrication tool for studies of size-dependent nanoparticle optics. *J. Phys. Chem. B*, 105(24):5599–5611, June 2001.

[8] S. Link, M. B. Mohamed, and M. A. El-Sayed. Simulation of the optical absorption spectra of gold nanorods as a function of their aspect ratio and the effect of the medium dielectric constant. *J. Phys. Chem. B*, 103(16):3073–3077, April 1999.

[9] Y. Xia and N. J. Halas, editors. *Synthesis and Plasmonic Properties of Nanostructures*, volume 30. MRS Bull., 2005.

[10] J. Shi, S. Gider, K. Babcock, and D. D. Awschalom. Magnetic clusters in molecular beams, metals, and semiconductors. *Science*, 271(5251):937–941, February 1996.

[11] S. C. Street, C. Xu, and D. W. Goodman. The physical and chemical properties of ultrathin oxide films. *Annual Review of Physical Chemistry*, 48:43–68, October 1997.

[12] Z. L. Wang, J. M. Petroski, T. C. Green, and M. A. El-Sayed. Shape transformation and surface melting of cubic and tetrahedral platinum nanocrystals. *J. Phys. Chem. B*, 102(32):6145–6151, August 1998.

[13] Ronald P. Andres, Jeffery D. Bielefeld, Jason I. Henderson, David B. Janes, Venkat R. Kolagunta, Clifford P. Kubiak, William J. Mahoney, and Richard G. Osifchin. Self-assembly of a two-dimensional superlattice of molecularly linked metal clusters. *Science*, 273(5282):1690–1693, September 1996.

[14] S. Gorer, J. A. Ganske, J. C. Hemminger, and R. M. Penner. Size-selective and epitaxial electrochemical/chemical synthesis of sulfur-passivated cadmium sulfide nanocrystals on graphite. *J. Am. Chem. Soc.*, 120(37):9584–9593, September 1998.

[15] http://www.britishmuseum.org/.

[16] Walter Caseri. Nanocomposites of polymers and metals or semiconductors: Historical background and optical properties. *Macromolecular Rapid Communications*, 21(11):705–722, 2000.

[17] I. Freestone, N. Meeks, M. Sax, and C. Higgitt. A roman nanotechnology. *Gold bulletin*, 40:270, 2007.

[18] M. Faraday. *Philos. Trans. Royal Soc. London*, 147:145, 1857.

[19] I. O. Sosa, C. Noguez, and R. G. Barrera. Optical properties of metal nanoparticles with arbitrary shapes. *J. Phys. Chem. B*, 107(26):6269–6275, July 2003.

[20] Hsiaoyun V. Chu, Yongjun Liu, Yaowen Huang, and Yiping Zhao. A high sensitive fiber sers probe based on silver nanorod arrays. *Opt. Express*, 15(19):12230–12239, 2007.

[21] Rakesh K. Joshi, Einar F. Kruis, and Olga Dmitrieva. Gas sensing behavior of sno1.8:ag films composed of size-selected nanoparticles. *Journal of Nanoparticle Research*, 8(6):797–808, December 2006.

[22] J. E. Redman. Surface plasmon resonance for probing quadruplex folding and interactions with proteins and small molecules. *Methods*, 43(4):302–312, December 2007.

[23] L. Malic, B. Cui, T. Veres, and M. Tabrizian. Enhanced surface plasmon resonance imaging detection of dna hybridization on periodic gold nanoposts. *Opt. Lett.*, 32(21):3092–3094, November 2007.

[24] Stefan A. Maier, Pieter G. Kik, Harry A. Atwater, Sheffer Meltzer, Elad Harel, Bruce E. Koel, and Ari A. Requicha. Local detection of electromagnetic energy transport below the diffraction limit in metal nanoparticle plasmon waveguides. *Nat Mater*, 2(4):229–232, April 2003.

[25] M. Fleischmann, P. J. Hendra, and A. J. Mcquillan. Raman spectra of pyridine adsorbed at a silver electrode. *Chemical Physics Letters*, 26(2):163–166, May 1974.

[26] M. Moskovits. Surface roughness and the enhanced intensity of raman scattering by molecules adsorbed on metals. *The Journal of Chemical Physics*, 69(9):4159–4161, 1978.

[27] G. Laurent, N. Félidj, J. Aubard, G. Lévi, J. R. Krenn, A. Hohenau, G. Schider, A. Leitner, and F. R. Aussenegg. Surface enhanced raman scattering arising from multipolar plasmon excitation. *The Journal of Chemical Physics*, 122(1):011102, 2005.

[28] Tamitake Itoh, Vasudevanpillai Biju, Mitsuru Ishikawa, Yasuo Kikkawa, Kazuhiro Hashimoto, Akifumi Ikehata, and Yukihiro Ozaki. Surface-enhanced resonance raman scattering and background light emission coupled with plasmon of single ag nanoaggregates. *The Journal of Chemical Physics*, 124(13):134708, 2006.

[29] Luis M. Liz-Marzan. Nanometals: Formation and color. *Materials Today*, 7(2):26–31, February 2004.

[30] G. Frens. Controlled nucleation for regulation of particle-size in monodisperse gold suspensions. *Nature-Physical Science*, 241:20–22, 1973.

[31] B. Nikoobakht and M. A. El-Sayed. Preparation and growth mechanism of gold nanorods (nrs) using seed-mediated growth method. *Chem. Mater.*, 15(10):1957–1962, May 2003.

[32] J. Rodriguez-Fernandez, J. Perez-Juste, F. J. Garciadeabajo, and L. M. Liz-Marzan. Seeded growth of submicron au colloids with quadrupole plasmon resonance modes. *Langmuir*, 22(16):7007–7010, August 2006.

[33] I. Pastoriza-Santos and L. M. Liz-Marzan. Synthesis of silver nanoprisms in dmf. *Nano Lett.*, 2(8):903–905, August 2002.

[34] C. R. Martin. Membrane-based synthesis of nanomaterials. *Chem. Mater.*, 8(8):1739–1746, August 1996.

[35] T. Thurn-Albrecht, J. Schotter, G. A. Kastle, N. Emley, T. Shibauchi, L. Krusin-Elbaum, K. Guarini, C. T. Black, M. T. Tuominen, and T. P. Russell. Ultrahigh-density nanowire arrays grown in self-assembled diblock copolymer templates. *Science*, 290(5499):2126–2129, December 2000.

[36] W. Rechberger, A. Hohenau, A. Leitner, J. R. Krenn, B. Lamprecht, and F. R. Aussenegg. Optical properties of two interacting gold nanoparticles. *Optics Communications*, 220:137–141, May 2003.

[37] P. M. Mendes, S. Jacke, K. Critchley, J. Plaza, Y. Chen, K. Nikitin, R. E. Palmer, J. A. Preece, S. D. Evans, and D. Fitzmaurice. Gold nanoparticle patterning of silicon wafers using chemical e-beam lithography. *Langmuir*, 20(9):3766–3768, April 2004.

[38] C. L. Haynes, A. D. Mcfarland, M. T. Smith, J. C. Hulteen, and R. P. Van Duyne. Angle-resolved nanosphere lithography: Manipulation of nanoparticle size, shape, and interparticle spacing. *J. Phys. Chem. B*, 106(8):1898–1902, February 2002.

[39] Hiroshi Tsuji, Nobutoshi Arai, Takuya Matsumoto, Kazuya Ueno, Yasuhito Gotoh, Kouichiro Adachi, Hiroshi Kotaki, and Junzo Ishikawa. Silver nanoparticle formation in thin oxide layer on silicon by silver-negative-ion implantation for coulomb blockade at room temperature. *Applied Surface Science*, 238(1-4):132–137, November 2004.

[40] A. L. Stepanov and V. N. Popok. Nanostructuring of silicate glass under low-energy ag-ion implantation. *Surface Science*, 566-568(Part 2):1250–1254, September 2004.

[41] F. K. Urban, Hosseini A. Tehrani, P. Griffiths, A. Khabari, Y. W. Kim, and I. Petrov. Nanophase films deposited from a high-rate, nanoparticle beam. *Journal of Vacuum Science & Technology B: Microelectronics and Nanometer Structures*, 20(3):995–999, 2002.

[42] J. Okumu, C. Dahmen, A. N. Sprafke, M. Luysberg, G. von Plessen, and M. Wuttig. Photochromic silver nanoparticles fabricated by sputter deposition. *Journal of Applied Physics*, 97(9):094305, 2005.

[43] D.B. Chrisey and K.G. Hubler. *Pulsed Laser Deposition of Thin Films.* John Wiley & Sons, 1994.

[44] M. Ohring. *Materials science of thin films: deposition and structure.* Academic press, 2002.

[45] Michael Störmer and Hans-Ulrich Krebs. Structure of laser deposited metallic alloys. *Journal of Applied Physics*, 78:7080+, 1995.

[46] J. Gonzalo, A. Perea, D. Babonneau, C. N. Afonso, N. Beer, J. P. Barnes, A. K. Petford-Long, D. E. Hole, and P. D. Townsend. Competing process during the production of metal nanoparticles by pulsed laser deposition. *Phys. Rev. B*, 71:125420, 2005.

[47] N. M. Dempsey, L. Ranno, D. Givord, J. Gonzalo, R. Serna, G. T. Fei, R. C. Doole, and A. K. Petford-Long. Magnetic behaviour of fe nanocrystals embedded in an oxide host produced by pulsed laser deposition. *J. Appl. Phys.*, 90:6268–6274, 2001.

[48] J. P. Barnes, A. K. Petford-Long, A. Suárez-García, and R. Serna. Evidence for shallow implantation during the growth of bismuth nanocrystals by pulsed laser deposition. *J. Appl. Phys.*, 93:6396, 2003.

[49] J. P. Barnes, A. K. Petford-Long, R. C. Doole, R. Serna, J. Gonzalo, A. Suárez-García, C. N. Afonso, and D. Hole. Structural studies of ag nanocrystals embedded in amorphous al2o3 grown by pulsed laser deposition. *Nanotechnology*, 13(4):465–470, 2002.

[50] R. Serna, C. N. Afonso, J. M. Ballesteros, A. Naudon, D. Babonneau, and A. K. Petford-Long. Size, shape anisotropy and distribution of cu nanocrystals embedded in amorphous al2o3 grown by pulsed laser deposition. *Appl. Surf. Sci.*, 138-139:1–5, 1999.

[51] A. N. Dobrynin, D. N. Ievlev, K. Temst, P. Lievens, J. Margueritat, J. Gonzalo, C. N. Afonso, S. Q. Zhou, A. Vantomme, E. Piscopiello, and G. Van Tendeloo. Critical size for exchange bias in ferromagnetic-antiferromagnetic particles. *Applied Physics Letters*, 87(1):012501, 2005.

[52] A. Tiwari, A. Chugh, C. Jin, and J. Narayan. Role of self-assembled gold nanodots in improving the electrical and optical characteristics of zinc oxide films. *Journal of Nanoscience and Nanotechnology*, pages 368–371, October 2003.

[53] Y. Zhu and P. P. Ong. Thin films of silicon nanoparticles embedded in al2o3 matrices. *Surface Review and Letters*, 8(5):559–564, 2001.

[54] V. Dureuil, C. Ricolleau, M. Gandais, C. Grigis, J. P. Lacharme, and A. Naudon. Growth and morphology of cobalt nanoparticles on alumina. *Journal of Crystal growth*, 233(4):737–748, December 2001.

[55] Jong-Won Yoon, Takeshi Sasaki, and Naoto Koshizaki. Photoelectrochemical behavior of pt/tio2 nanocomposite thin films prepared by pulsed laser deposition. *Applied Surface Science*, 197-198:684–687, September 2002.

[56] Y. Zhu and P. P. Ong. Preparation and photoluminescence of thin films of ge nanoparticles embedded in al2o3 matrices. *Journal of Physics: Condensed Matter*, 13(18):4075–4080, 2001.

[57] Shunsuke Ohtsuka, Keiji Tsunetomo, Tadashi Koyama, and Shuhei Tanaka. Ultrafast nonlinear optical effect in cdte-doped glasses fabricated by the laser evaporation method. *Optical Materials*, 2(4):209–215, October 1993.

[58] Serna, R., Suarez-Garcia, A., Afonso, C.N., Babonneau, and D. Optical evidence for reactive processes when embedding cu nanoparticles in al2o3 by pulsed laser deposition. *Nanotechnology*, 17(18):4588–4593, September 2006.

[59] Bruce T. Draine and Piotr J. Flatau. User guide for the discrete dipole approximation code ddscat 6.1, Nov 2006.

[60] J. I. Gersten, D. A. Weitz, T. J. Gramila, and A. Z. Genack. Inelastic mie scattering from rough metal surfaces: Theory and experiment. *Physical Review B*, 22(10):4562+, November 1980.

[61] Euge‘ne Duval. Far-infrared and raman vibrational transitions of a solid sphere: Selection rules. *Physical Review B*, 46(9):5795+, 1992.

[62] Maurizio Montagna and Roberto Dusi. Raman scattering from small spherical particles. *Physical Review B*, 52(14):10080+, October 1995.

[63] B. Palpant, H. Portales, L. Saviot, J. Lermé, B. Prével, M. Pellarin, E. Duval, A. Perez, and M. Broyer. Quadrupolar vibrational mode of silver clusters from plasmon-assisted raman scattering. *Physical Review B*, 60(24):17107+, December 1999.

[64] H. Portales, L. Saviot, E. Duval, M. Fujii, S. Hayashi, N. Del Fatti, and F. Vallée. Resonant raman scattering by breathing modes of metal nanoparticles. *The Journal of Chemical Physics*, 115(8):3444–3447, 2001.

[65] A. Courty, I. Lisiecki, and M. P. Pileni. Vibration of self-organized silver nanocrystals. *The Journal of Chemical Physics*, 116(18):8074–8078, 2002.

[66] A. Nelet, A. Crut, A. Arbouet, N. Del Fatti, F. Vallee, H. Portales, L. Saviot, and E. Duval. Acoustic vibrations of metal nanoparticles: high order radial mode detection. *Applied Surface Science*, 226(1-3):209–215, March 2004.

[67] H. Lamb. *Proc. Lond. Math. Soc.*, 13:189, 1882.

[68] Daniel B. Murray, Avra S. Laarakker, and Lucien Saviot. High precision numerical estimates of acoustic phonon frequencies of nonspherical nanoparticles. *physica status solidi (c)*, 3(11):3935–3938, 2006.

[69] Lucien Saviot, Daniel B. Murray, and Maria del Carmen Marco de Lucas. Vibrations of free and embedded anisotropic elastic spheres: Application to low-frequency raman scattering of silicon nanoparticles in silica. *Physical Review B (Condensed Matter and Materials Physics)*, 69(11):113402, 2004.

[70] G. Bachelier and A. Mlayah. Surface plasmon mediated raman scattering in metal nanoparticles. *Physical Review B (Condensed Matter and Materials Physics)*, 69(20):205408, 2004.

[71] A. N. Dobrynin, K. Temst, P. Lievens, J. Margueritat, J. Gonzalo, C. N. Afonso, E. Piscopiello, and G. Van Tendeloo. Observation of co/coo nanoparticles below the critical size for exchange bias. *Journal of Applied Physics*, 101(11):113913, 2007.

[72] C. Clavero, G. Armelles, J. Margueritat, J. Gonzalo, M. García del Muro, A. Labarta, and X. Batlle. Interface effects in the magneto-optical properties of co nanoparticles in dielectric matrix. *Applied Physics Letters*, 90(18):182506, 2007.

[73] T. H. Maiman. Stimulated optical radiation in ruby. *Nature*, 187(4736):493–494, 1960.

[74] F. Breech and L. Cross. *Applied Spectroscopy*, 16, 1962.

[75] H. M. Smith and A. F. Turner. Vaccum deposited thin films using a ruby laser. *Appl. Opt.*, 4:147, 1965.

[76] D. Dijkkamp, T. Venkatesan, X. D. Wu, S. A. Shaheen, N. Jisrawi, Min Y. H. Lee, W. L. Mclean, and M. Croft. Preparation of y-ba-cu oxide superconductor thin films using pulsed laser evaporation from high t[sub c] bulk material. *Applied Physics Letters*, 51(8):619–621, 1987.

[77] J. Gonzalo, R. Serna, J. Solís, D. Babonneau, and C. N. Afonso. Morphological and interaction effects on the surface plasmon resonance of metal nanoparticles. *Journal of Physics: Condensed Matter*, 15(42):S3001–S3010, 2003.

[78] J. P. Perez, R. Carles, and R. Flekinger. *Électromagnétisme : Fondements et applications*. Masson, 1997.

[79] C. Kittel. *Introduction to solid states physic*. Dunod Univeristé, 1975.

[80] B. Palpant. *Effets de tailles dans la reponse optique d agregats de metaux nobles en matrice: etude experimental et interpretation theorique*. PhD thesis, Universit Claude Bernard, lyon, 1998.

[81] P. B. Johnson and R. W. Christy. Optical constants of the noble metals. *Phys. Rev. B*, 6:4370–4379, December 1972.

[82] W. Hayes and R. Loudon. *Scattering of light by crystals*. John Wiley & Sons, 1978.

[83] W. A. Kamitakahara and B. N. Brockhouse. Crystal dynamics of silver. *Physics Letters A*, 29(10):639–640, August 1969.

[84] H. Portales. *Etude par diffusion Raman de nanoparticles metalliques en matrice dielectrique amorphe*. PhD thesis, Universit Claude Bernard, Lyon, 2001.

[85] M. Cazayous. *Interferences Raman et nanostructures*. PhD thesis, Universite Paul Sabatier, Toulouse, 2002.

[86] U. Kreibig and M. Vollmer. *Optical properties of metal clusters*. Springer-Verlag, 1994.

[87] C.F. Bohren and D.R. Huffman. *Absorption and Scattering of Light by Small Particles*. John Wiley & Sons, 1998.

[88] O. Jepsen, D. Glötzel, and A. R. Mackintosh. Potentials, band structures, and fermi surfaces in the noble metals. *Physical Review B*, 23(6):2684+, March 1981.

[89] G. Bachelier. *Proprietes optiques de nano-structures metalliques et semi-conductrices*. PhD thesis, Univeriste Paul Sabatier, Toulouse, 2005.

[90] Richard Gans. ber die optischen eigenschaften kolloidaler goldlösungen. *Annalen der Physik*, 352(1):270–284, 1915.

[91] Love A. E. H. *A treatise on the mathematical theory of elasticity*. Dover Publication, 1944.

[92] E. Duval, A. Boukenter, and B. Champagnon. Vibration eigenmodes and size of microcrystallites in glass: Observation by very-low-frequency raman scattering. *Physical Review Letters*, 56(19):2052+, May 1986.

[93] M. Fujii, T. Nagareda, S. Hayashi, and K. Yamamoto. Low-frequency raman scattering from small silver particles embedded in sio_2 thin films. *Physical Review B*, 44(12):6243+, 1991.

[94] L. Saviot and D. B. Murray. Longitudinal versus transverse spheroidal vibrational modes of an elastic sphere. *Physical Review B*, 72:205433, 2005.

[95] William M. Visscher, Albert Migliori, Thomas M. Bell, and Robert A. Reinert. On the normal modes of free vibration of inhomogeneous and anisotropic elastic objects. *The Journal of the Acoustical Society of America*, 90(4):2154–2162, 1991.

[96] J. Margueritat, J. Gonzalo, C. N. Afonso, G. Bachelier, A. Mlayah, A. S. Laarakker, D. B. Murray, and L. Saviot. From silver nanolentils to nanocolumns: surface plasmonpolaritons and confined acoustic vibrations. *Applied Physics A: Materials Science & Processing*, 89(2):369–372, November 2007.

[97] J. Margueritat, J. Gonzalo, C. N. Afonso, A. Mlayah, D. B. Murray, and L. Saviot. Surface plasmons and vibrations of self-assembled silver nanocolumns. *Nano Lett.*, 6(9):2037–2042, September 2006.

[98] Jérémie Margueritat, Jose Gonzalo, Carmen N. Afonso, Isabel M. Ortiz, and Carmen Ballesteros. Production of self-aligned metal nanocolumns embedded in an oxide matrix film. *Applied Physics Letters*, 88(9):093107, 2006.

[99] William M. Visscher, Albert Migliori, Thomas M. Bell, and Robert A. Reinert. On the normal modes of free vibration of inhomogeneous and anisotropic elastic objects. *The Journal of the Acoustical Society of America*, 90(4):2154–2162, 1991.

[100] E. D. Palik. *Handbook of Optical Constants of Solids.* Academic press, 1985.

[101] P. Gangopadhyay, T. R. Ravindran, K. G. M. Nair, S. Kalavathi, B. Sundaravel, and B. K. Panigrahi. Raman scattering studies of cobalt nanoclusters formed during high energy implantation of cobalt ions in a silica matrix. *Applied Physics Letters*, 90(6), 2007.

[102] A. Bouhelier, M. Beversluis, A. Hartschuh, and L. Novotny. Near-field second-harmonic generation induced by local field enhancement. *Physical Review Letters*, 90(1):013903+, January 2003.

[103] Neil Anderson, Alexandre Bouhelier, and Lukas Novotny. Near-field photonics: tip-enhanced microscopy and spectroscopy on the nanoscale. *Journal of Optics A: Pure and Applied Optics*, 8(4):S227–S233, 2006.

A

List of Publication and communications

Publications in International Journal

1. *Critical Size for exchange bias in ferromagnetic-antiferromagnetic particles*
   Appl. Phys. Lett. **87** Art. 012501 (2005)
   A.N. Dobrynin, D.N. Ievlev, K. Temst, P. Lievens, **J. Margueritat**, J. Gonzalo, C.N. Afonso, S. Zhou, A.Vantomme, E. Piscopiello, G. Van Tendeloo

2. *Oriented Silver nanocolumns produced by pulsed laser deposition*
   Appl. Phys. Lett. **88**, Art. 093107 (2006)
   J. Margueritat, J. Gonzalo, A. Mlayah, C. N. Afonso

3. *Surface plasmons and Vibrations of self-assembled silver nanocolumns*
   Nano Lett. **6**, 2037-2042 (2006)
   J. Margueritat, J. Gonzalo, C. N. Afonso, A. Mlayah, D.B. Murray, L.Saviot

4. *Observation of Co/CoO nanoparticles below the critical size for exchange bias*
   J. Appl. Phys. **101**, Art. 113913 (2007) A.N. Dobrynin, K. Temst, P. Lievensy, **J. Margueritat**, J. Gonzalo, C.N. Afonso, E. Piscopiello G. Van Tendeloo

5. *From silver Nanolentils to Nanocolumns: Surface plasmon-polaritons and confined acoustic vibrations*
   Appl. Phys. A. **89**, 369-372 (2007)
   J. Margueritat, J. Gonzalo, C.N. Afonso, G. Bachelier, A. Mlayah, A.S. Laarakker, D.B. Murray, L. Saviot.

6. *Interface effects in the magneto-optical properties of Co nanoparticles in dielectric matrix*
   Appl. Phys. Lett. **90**, Art. 182506 (2007)
   C. Clavero, G. Armelles, **J. Margueritat**, J. Gonzalo, M. Garca del Muro, A. Labarta. X. Batlle.

7. *Size dispersion effects on the low-frequency Raman scattering of (quasi-) spherical metal nanoparticles*
   Phys. Rev. B. **76**, 2345419 (2007)
   G. Bachelier, A. Mlayah, **J. Margueritat**, J. Gonzalo, C.N. Afonso,

8. *Acoustic vibration modes and electron-lattice coupling in self-assembled silver nanocolumns*
   Accepted in Nano Letters
   J. Burgin, P. Langot, A. Arbouet , **J. Margueritat**, J. Gonzalo, C.N. Afonso, F. Valle, A. Mlayah, M.D. Rossell, G. Van Tendeloo

9. *Surface Plasmon-Polaritons and Acoustic vibrations in Co-Ag interacting nanoparticles*
   Submitted to Nanotechnology
   J. Margueritat, J. Gonzalo, C.N. Afonso, U. Romn, G. Van Tendeloo, A. Mlayah, D.B. Murray, L. Saviot, Y. Zhou, M.H. Hong, B.S. Lukyanchuk

Communications in school or conferences

Presented by myself :

- TNT04, Trends in NanoTechnology 2004, Segovia, (Spain); Poster presentation **2004**

- Congrs Gnral de la socit Franaise de Physique, Lille, (France); Poster presentation **2005**

- 8th Conference On Laser Ablation (COLA), Banff (Canada); Poster presentation **2005**
- 10emes Journes de la matire condense, Toulouse (France); Poster presentation **2006**
- Quantum Physics of Nanostructures Workshop, Stratford-upon-Avon (UK); Oral presentation **2006**
- International workshop on Plasmonics and Applications in Nanotechnologies, Singapore, (republic of Singapore); Poster presentation; awarded with the first prize **2006**
- Photonics West, Synthesis and Photonics of Nanoscale Materials V., San Jos, California, (USA); Oral presentation **2007**
- 16th International Conference on Dynamical Processes in Excited States of Solids, DPC07, Segovia, Spain; Poster presentation, awarded with the first prize **2007**
- 9th Conference On Laser Ablation, COLA 07, Tenerife, Canaries, Spain; Oral presentation, awarded with honorary mention (second prize) **2007**
- 9th Conference On Laser Ablation, COLA 07, Tenerife, Canaries, Spain; Poster presentation **2007**

Presented by co-authors :

- 2nd Nanospain Workshop, Barcelona, (Spain); Poster presentation **2005**
- 8th Conference on single molecule magnets and hybrid magnetic nanostructures, Trieste, (Italy); Poster presentation **2005**
- Photonics West, Synthesis and Photonics of Nanoscale Materials V., San Jos, California, (USA); Invited Oral presentation **2007**
- Nanospain 2007. 4th International Workshop, Sevilla, (Spain); Poster presentation **2007**
- SPIE Europe, Optics and Optoelectronics, Prague, (Czech Republic); Oral presentation **2007**

- 8th International Symposium on Laser Precision Microfabrication, Vienna, (Austria); Oral and Poster presentation **2007**
- Phonons 2007, Paris, (France); Oral presentation **2007**
- 9th Conference On Laser Ablation, COLA 07, Tenerife, Canaries, Spain; Oral presentation **2007**

Schools :

- Nanophysics School at les houches (France) **2003**
- Nanocluster School 2, Madrid, (Spain); Oral presentation **2004**
- TEM school, Antwerp, (Belgica) **2005**
- NATO Advanced School Institute, (ASI), Magog (Canada); Oral presentation **2005**
- Nanocluster School 3, Helsinki, (Finland); Oral presentation **2006**
- Course on AFM of Biomelucles in Solutions, Birmingham, (UK) **2006**

Particpation in organization of conferences

- 9th Conference On Laser Ablation, COLA07 as member of the local organizing committee **2007**